12-14-2015

Surface Modification of Nanodiamond and Its Incorporation in Nanodiamond/Peek Nanocomposites

Zahidul Wahab
University of South Carolina - Columbia

SURFACE MODIFICATION OF NANODIAMOND AND ITS INCORPORATION IN NANODIAMOND/PEEK NANOCOMPOSITES

by

Zahidul Wahab

Bachelor of Engineering
McMaster University, 1999

Master of Engineering
McMaster University, 2002

Submitted in Partial Fulfillment of the Requirements

For the Degree of Doctor of Philosophy in

Chemical Engineering

College of Engineering and Computing

University of South Carolina

2015

Accepted by:

Harry J. Ploehn, Major Professor

Brian Benicewicz, Committee Member

Xiao-Dong Zhou, Committee Member

James A. Ritter, Committee Member

Lacy Ford, Senior Vice Provost and Dean of Graduate Studies

DEDICATION

I dedicate this dissertation to my parents Abdul Wahab and Dil Afrose Rokeya Wahab.

ACKNOWLEDGEMENTS

I would like to express my sincere gratitude to my Ph.D. advisor Dr. Harry J. Ploehn for his guidance, support and encouragement throughout the course of this project. It was a privilege to pursue this challenging endeavor under his guidance.

I would like to thank my Ph.D. committee members Dr. Brian Benicewicz, Dr. Xiao-Dong Zhou and Dr. James A. Ritter for their constructive suggestions.

I am extremely thankful to my USC colleagues Yating Mao and Dr. Sayful Islam for helping me with multiple experiments, characterizations and overall support throughout the years. I am also grateful to the research staff, and my colleagues at Horizon-1.

I would like to thank my employer Zeus Industrial Products, for their support and encouragement in pursuing this project. Special thanks go to Dr. Bruce Anneaux and Bob Ballard for their support and encouragement over the last several years. Without their support, it would be impossible to pursue this goal. I would like to take this opportunity to also thank the analytical lab personnel and R&D technicians of Zeus for helping me with sample prep, characterization and general support. Special thanks also go to my colleagues whose technical suggestions, support and encouragement helped me continue this project.

I would like to thank my parents for instilling ambition but never expecting too much, my siblings for helping me pursuing this less travelled path and my friends for their continuous encouragement.

Finally, I would like to thank my beautiful wife Clara for being there for me for the last several years. I hope that I will be able to make it up someday the weekends and weeknights that she spent by herself with the kids while I was working at the lab. I look forward to the exciting time that lies ahead of us with our children Zaynah and Rheo.

ABSTRACT

The continued miniaturization of electronic device components requires new lightweight polymers with high thermal stability, high thermal conductivity, low electrical conductivity, and low dielectric constant. Composites of nanodiamond (ND) and poly(ether ether ketone) (PEEK) are candidates for these applications due their unique combination of properties. The objectives of this research are to explore new routes for surface functionalization of nanodiamond (ND), develop methods for maximizing dispersion of ND as a nano-scale filler in PEEK, and characterize the effect of dispersed ND on the mechanical, thermal and dielectric properties of ND/PEEK composites.

Initial attempts to disperse different kinds of commercially available, as-received ND in PEEK were yielded with low quality composites due to ND agglomeration and low thermal stability. Thus we began to explore chemical grafting of phenylphosphonate (PPA) onto oxidized ND (OND) and carboxylated ND (CND), hypothesizing that the phenyl functional group would render the NDs more compatible with aromatic PEEK. Detailed characterization results, including ^{31}P NMR, FTIR, and XPS, indicate successful grafting, resulting in arylation of ND, increased ND thermal stability, and better compatibility with organic solvents. Sonication during the grafting promotes more

complete exposure of the ND surface to PPA grafting, resulting in even better ND dispersion in organic solvents.

PPA-modified OND and CND were then melt-blended with PEEK to produce ND/PEEK composites. Surface tomography results suggest that all PPA-modified NDs were adequately dispersed in PEEK, with OND showing better dispersion due to its higher PPA graft density. The presence of PPA-modified ND has minor impact on PEEK crystallinity based on XRD and DSC data. Tensile testing and DMA results suggest that ND/PEEK composites generally retain the mechanical properties of PEEK with some sacrifice of ductility. TGA data indicate that all ND/PEEK composites have excellent thermal stability at temperatures up to 400°C as needed for PEEK melt processing. ND/PEEK composites had dielectric constants lower than or comparable to that of pure PEEK, with low dielectric losses in most cases. Addition of OND or CND to PEEK generally increases the thermal conductivity relative to pure PEEK; the increase reached 38% for PPA-modified OND (prepared with sonication) blended with PEEK. These results suggest that ND/PEEK nanocomposites are good candidates for use in electronic device applications.

TABLE OF CONTENTS

LIST OF TABLES

LIST OF FIGURES

LIST OF SYMBOLS

ΔH_f	Enthalpy of fusion.
X_c	Degree of crystallinity.
K	Thermal conductivity (W/m.K).
ε_r	Relative permittivity or Dielectric constant.
tan δ	Dielectric loss tangent or DMA (Dynamic mechanical analysis) loss tangent
E’	Storage Modulus
T_g	Glass transition temperature
T_m	Melting temperature

LIST OF ABBREVIATIONS

PEEK ..... Poly(ether ether ketone)

ND ..... Nanodiamond

OND ..... Oxidized Nanodiamond

CND ..... Carboxylated Nanodiamond

ODA-ND ..... Octadecylamine-Functionalized Nanodiamond

PPA ..... Phenyl Phosphonic Acid

PPA@ND ..... PPA-grafted nanodiamond

HPEEK ..... Hydroxylated Poly(ether ether ketone)

PEES ..... Poly(1-4-phenylene ether-ether sulfone)

PEI ..... Polyetherimide

WAXS ..... Wide angle X-Ray diffraction

SAXS ..... Small angle X-ray diffraction

NMR ..... Nuclear magnetic resonance

FTIR ..... Fourier transform infrared spectroscopy

CHAPTER 1

INTRODUCTION

1.1 Motivation

Incorporating organic or inorganic fillers in a polymer matrix to enhance different physical properties of the polymer is a common practice in the polymer processing industry. The properties of the resulting polymer composites depend on the characteristics, dimensions, and shapes of the fillers and also on the interfacial bonding strength. Traditional microscale fillers, while having a positive impact on certain polymer properties, often diminish other useful properties.

Scientists have long known that decreasing filler dimension increases the specific surface area of the filler, which in turn may greatly and effectively improve the transfer of the load between the fillers and polymer matrix. In the last 20 years, there has been strong emphasis on the development of polymer nanocomposites, in which at least one of the dimensions of the filler has nanometer scale. These nanocomposite materials may exhibit significant enhancements in mechanical, electrical and thermal properties that are difficult to achieve using conventional fillers with microscale dimensions, such as carbon, glass, or aramid fibers.

Nanocomposites are currently applied in a variety of marine, automobile, aeronautical, aerospace and other engineering applications that demand an excellent combination of mechanical and thermal properties. Nowadays, engineering polymers are needed to create even lighter, thinner, stronger and cheaper structures with multifunctional properties and performance. In order to close the gap between the performance of today's engineering polymers and the ever increasing demand of engineering applications, new nanocomposites are needed with optimum nanofiller dispersion, improved load transfer ability from polymer to filler particles, and enhanced thermal and dielectric properties.

The continued miniaturization of electronic device components requires new lightweight polymers with high thermal stability. Heat dissipation in polymer based microelectronics is an issue because, compared to metals, polymers have low thermal conductivity. Poor thermal conductivity results in high device operating temperatures, which in turn hurts reliability. In fact, the reliability of an electronic device is exponentially related to its operating temperature. A 10-15^{0}C increase in operating temperature can result in a twofold reduction in the lifespan of a device [1]. Therefore, it is critical that the heat generated in the device be dissipated as quickly and effectively as possible to maintain the operating temperature of the device at a desired level.

One way to increase a polymer's thermal conductivity is to add thermally conductive filler particles. However, the most effective fillers in this regard, usually metals, lead to large increase in polymer composite dielectric permittivity. Above the

percolation threshold, a polymer filled with metal, carbon nanotube, or graphene-based fillers becomes conductive. Considering that polymers in electronic devices are required to serve as insulators, this is obviously undesirable. Low dielectric constant also helps to minimize signal cross talk and signal propagation delay [2].

Conventional cost efficient polymers used in electronic devices often have drawbacks such as halogenation, high sensitivity to moisture, poor dielectric properties at higher temperature and frequencies, low continuous service temperature and thermal stability, and poor solvent resistance. In order to overcome such drawbacks, high performance polymers reinforced with thermally conducting and electrically insulating nanoparticles are desired [2].

1.2 PEEK Nanocomposites

Poly(ether ether ketone) (PEEK) is a high performance thermoplastic used as neat polymer, in blends, and as matrix material in various composite applications. This semicrystalline and highly aromatic thermoplastic belongs to the class of polymer known as poly(aryl ether ketone)s, or PAEK. PAEK plastics are characterized by phenylene rings that are linked via oxygen bridges (ether and ketone). The ratio and sequence of ether to ketones mainly affects the glass transition temperature and melting point of the polymer, and thus its heat resistance and processing temperature. A higher ketone/ether ratio increases the rigidity of the polymer chain, which results in a higher glass transition temperature and melting point.

PEEK (Scheme 1) exhibits some of the highest thermal transitions found in commercially available polymers today, due to its relatively stiff aromatic polymer backbone. As a result, it can be continuously used at temperatures up to 260^0C and for shorter durations up to 300^0C. Typically PEEK has a melting temperature of 343^0C,

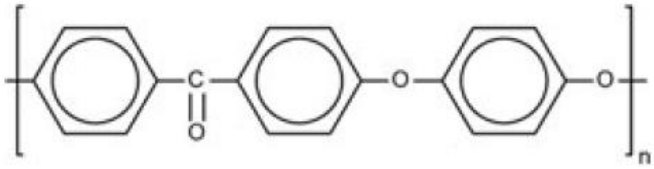

Scheme-1. Structure of Poly(ether ether ketone) (PEEK)

glass transition temperature (T_g) of 143^0C, and is stable in the melt at 400^0C for 1 h. The Young's modulus is 3.6 GPa, and its tensile strength is 90 to 100 MPa. PEEK can be obtained in amorphous and semicrystalline form, depending on the processing conditions employed from the molten state. The standard grade of PEEK is 35% crystalline. However, a maximum crystallinity level of 40% can be achieved by cooling the melt at very low cooling rates (1^0C/minute) [3, 4]. PEEK possesses a range of good properties, including toughness, very low smoke emission in flammability tests, and resistance to all common solvents [3]. It is well known that PEEK has good resistance to most organic solvents except concentrated sulfuric acid (95-98%) and methyl sulfonic acid (CH_3SO_3H). Certain grades of PEEK are FDA approved and being used as medical implants due to its excellent biocompatibility. It is also extensively used in the aerospace, automotive, electronic, and chemical process industries.

Advanced composites based on PEEK have attracted the attention of polymer technologists due to its high temperature stability, adaptability to various processing techniques, and good mechanical and chemical properties. PEEK polymers reinforced with nanoparticles processed via solid, partial melt and melt state blending routes have been reported. Another commonly used method for preparing nanocomposites is solution blending, in which a polymer solution is blended with a nanoparticle dispersion, followed by solvent evaporation. Because PEEK is insoluble in most practical solvents, solution blending routes to PEEK nanocomposites have not been explored.

Vapor-grown carbon nanofibers have been melt blended at up to 10 wt% with PEEK to produce composite fibers with increased stiffness, yield stress, and fracture strength [5]. PEEK nanocomposites containing up to 17 wt% CVD MWCNTs (multiwall carbon nanotubes) have been prepared by melt compounding and injection molding. The composite's mechanical properties exhibit a percolation threshold for (both shear and extensional deformation) at 1 wt%, and electrical percolation at 2 wt% MWNT [6]. Percolation effects were not observed for thermal conductivity and tensile modulus. These properties increased only linearly with increase in nanotube content, rising by 130% and 50% at 17 wt% MWCNT, respectively.

Multiple studies have reported the influence of compatibilizing agents on the dispersion quality of CNTs in PEEK matrix. Compatibilizers such as polyetherimide (PEI), poly(bisphenol-A-ether sulfone) (PES) and poly(1-4-phenylene ether-ether sulfone) (PEES), being miscible with and structurally similar to PEEK, work as polymeric

surfactants to reduce interfacial tension and promote adhesion between the PEEK matrix and the CNTs [7]. MWCNTs wrapped with poly(ether sulphone) (PES) and dispersed in PEEK produced composites with high dielectric constant, low dielectric loss, higher electrical conductivity, and good mechanical and thermal properties [8]. PEI, when used as a compatibilizing agent in PEEK-SWCNT nanocomposites, increased the composite's thermal conductivity, modulus, glass transition temperature and electrical conductivity [9]. Similar improvement in mechanical properties, electrical conductivity, and thermal conductivity was also observed when two types of polysulfones (PEES and PSF) were used as compatibilizing agents in PEEK-SWCNT nanocomposites [10].

One of the most efficient approaches to disperse SWCNTs (Single wall carbon nanotubes) was achieved by covalently grafting PEEK-OH (Hydroxylated PEEK derivative) onto acid-treated SWCNTs [11]. PEEK and HPEEK-grafted SWCNTs were melt blended to produce nanocomposites with significant improvements in the Young's modulus, strength, toughness, thermal stability, storage modulus and glass transition temperature, but with decreased crystallization and melting temperatures [12]. Ethyl-aminated and phenyl-aminated graphene oxide (GO)/MWCNT hybrid fillers have been blended with PEEK to increase the thermal conductivity of the nanocomposites by more than two fold [1].

Nano-barium titanate added to ferrite-filled PEEK was found to increase the degradation temperature, glass transition temperatures, and loss tangent of the PEEK nanocomposite without changing the melting behavior of the PEEK matrix [13]. This

composite system, evaluated as a radar-abosrbing structural material (RASM), yielded increased tensile and flexural moduli, reflection losses, dielectric constant, and loss tangent (measured at 10GHz, room temperature) with increased ferrite content. With increasing nano-barium titanate loading, the ferrite-filled PEEK composites had increased tensile strength, flexural strength, tensile modulus and dielectric constant, but decreased elongation at break, flexural modulus and loss tangent [14]. PEEK nanocomposites prepared with only $BaTiO_3$ up to 67 vol% had dielectric constant increases of approximately 14-fold (measured at 1 MHz) with low dielectric loss.

Unmodified SiO_2 or Al_2O_3 (5-7.5 wt%) have been used to produce PEEK nanocomposites with hardness, elastic modulus, and tensile strength increased by 20-50%, but with a sacrifice of tensile ductility [15]. When nano-sized silica was surface modified by stearic acid, the dispersion quality was much improved, and the nanocomposite's storage modulus was found to be 40% higher from 100 to 250^0C [16]. Nanomaterials such as SiO_2, TiO_2 and ZnS have also been used successfully in PEEK composites for tribological applications [17, 18].

Due to the sp^2 carbon based structure, carbon based nanomaterials such as graphene and carbon nanotubes have very high electrical conductivity. For applications where thermally conducting but electrically insulating composites are required, ceramic particles have been the preferred option to incorporate into different polymers [19]. For PEEK related composites, the ceramic fillers often had relatively high dielectric constants. Unfortunately, thermal conductivity was not measured in most cases. For a

microwave substrate application, strontium titanate ($SrTiO_3$, ε = 270) was used as a filler in PEEK. The permittivity of the composite increased linearly from 3.3 to ~5.9 for up to 35 wt% filler loading. Beyond this filler loading, the permittivity showed a decreasing trend due to the presence of porosity. The loss tangent showed an increasing trend up to 25 wt% but decreased beyond this level [20]. Composites of aluminum nitride (AlN, ε =8.5) in PEEK, developed for an electronics packaging substrate application, had significantly improved mechanical properties, thermal properties, and substantially lower coefficient of thermal expansion (CTE). The dielectric constant increased slightly from 3.37 to 4.11 and dielectric loss from 0.0066 to 0.0115 (at 1MHz) for AlN filler loading of up to 30 wt% [19]. PEEK nanocomposites containing Silicone nitride (Si_3N_4, ε = 8.3) again for an electronic substrate application, yielded lower CTE, higher T_g, and higher microhardness. The dielectric constant increased marginally to 3.84 at 30 wt% filler loading. The loss factor decreased to as low as 0.0058 at 10 wt% [21]. PEEK nanocomposite reinforced with phenyltrimethoxysilane (PTMS) treated silica yielded a lower dielectric constant than pure PEEK at low loading (<10 wt%) but increased to 3.84 at 30 wt% filler level [2]. For another printed circuit board (PCB)/electronic substrate application, talc was used successfully as a microscale filler in PEEK to reduce the CTE. The dielectric constant of the PEEK composite increased with increasing filler fraction (up to 52 wt%) and moisture uptake (measured at 10 MHz) from 3.15 (dry condition) to 3.77 (50% r.h.). A marginal increase in the dielectric loss was noticed, as well [22].

1.3 Nanodiamond and its Surface Modification

Nanodiamond is a carbon allotrope and a unique form of carbon nanomaterial. These nanoscale diamond particles were first produced by detonation synthesis in the 1960's in the former USSR [23]. Owing to their relatively small and narrow size distribution, tunable surface structures, and chemical inertness, nanodiamonds have become well-known since the late 1990s due to their extraordinary mechanical, electronic, thermal, and tribological properties. ND also has significant potential as a component of novel multifunctional materials.

Detonation synthesis is one of the primary techniques to produce bulk-scale nanometric diamond particles. The process consists of placing an explosive charge into a detonation chamber and igniting it either by another accelerator charge or electrically (Figure 1.1). In this process, no additional carbon material is needed for the formation of diamond soot. The explosive itself delivers the carbon. In an oxygen-deficient atmosphere, the incomplete combustion of organic explosives, such as TNT or hexogen, leads to the formation of elemental carbon, in addition to the combustion products CO_2, CO, water and nitrogen [24]. The resultant product of detonation synthesis is

detonation soot, which is a mixture of primary diamond particles 4-5 nm in diameter with other carbon allotropes and impurities. These primary particles have very large specific surface area (>>200 m^2/gm) [25].

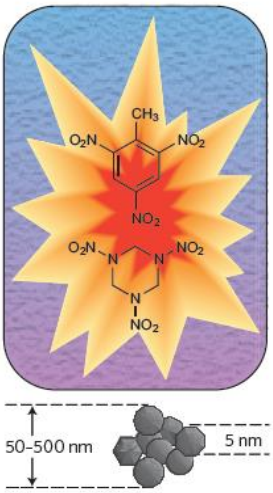

Figure 1.1. Detonation synthesis of nanodiamonds [24].

The process of purifying detonation soot to yield high content of nanodiamond involves several steps (Figure 1.2). The oxidation process used to purify the nanodiamond and remove the non-diamond carbon and non-carbon impurities also removes various functional groups from the nanodiamond surface and produces oxygen-containing surface species such as $–CO_2H$ (carboxylic acids), lactone, C=O (keto carbonyl), anhydrides, and –OH (hydroxyl) (Figure 1.3) [26]. As a result, the ND surfaces are very polar and hydrophilic.

In addition, interparticle hydrogen bonding and formation of ester, ether, and anhydride bonds are believed to play important role in assembling the DND primary particles into much larger aggregates with sizes ranging from a few hundred nanometers (“core agglutinates”) to a few tens of microns (“agglomerates”)[28]. Thus the agglomeration occurs not only due to van der Waals and electrostatic (Coulombic) interactions, but also due to the chemical bonding force. Figure 1.4 presents a possible

structure model of diamond agglomerates. Previous studies [24, 29] found that nanodiamond aggregates can withstand strong ultrasonic treatment. In other words, strong ultrasonic treatment can break down large nanodiamond agglomerates into 100-200 nm aggregates, but it fails to disperse 100-200 nm aggregates into 4-5 nm primary nanodiamonds [30]. While these aggregated NDs can be useful in certain applications such as chromatography or drug delivery [24], for many applications deaggregation into individual primary particles is desired to take full advantage of nanodiamond properties.

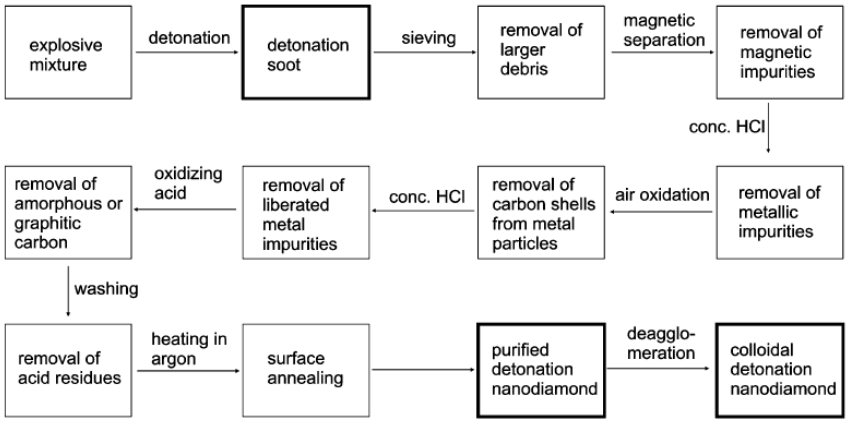

Figure 1.2. Process to purify detonation soot to produce nanodiamond [27].

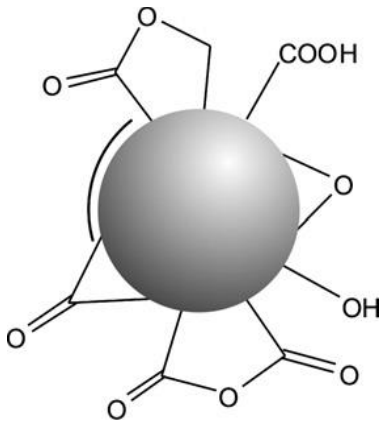

Figure 1.3. Various functional groups covering the surface of nanodiamond [27].

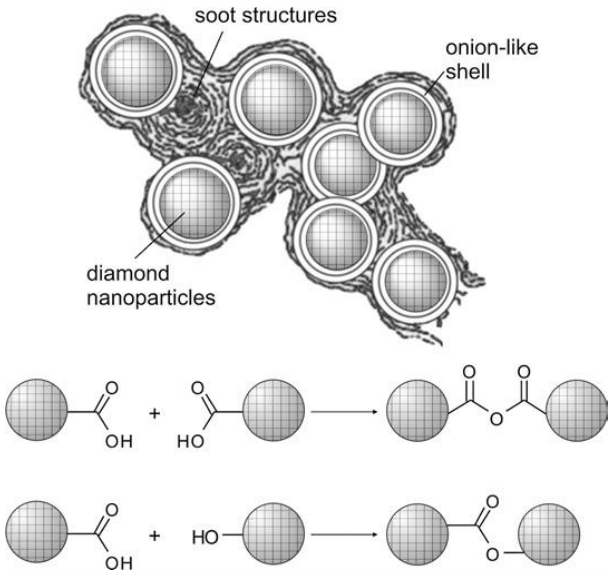

Figure 1.4. A possible structure model for ND agglomerates in detonation ND [27].

A distinct feature of nanodiamonds, in contrast with carbon nanotubes and other graphitic nanoparticles, is that many different functional groups can be attached to the ND surface, allowing quite sophisticated surface functionalization without compromising the useful properties of the diamond core [31]. The understanding of these groups' interactions with their surroundings and the reduction of detrimental effects such as aggregation are also important [27]. Although the various functional groups present on commercial nanodiamond powders can be used for covalent functionalization, it is more convenient to start with carboxylated nanodiamond produced by air or ozone purification (Figure 1.5), and then take advantage of the rich chemistry of COOH groups [24]. Figure 1.6 presents various routes of nanodiamond surface modifications reported to date. Covalent surface modifications of diamond

nanoparticles are generally focused on improving the ND processability and introducing suitable functional groups to impart, enhance, or tailor certain properties and, for polymer composites, ND-polymer compatibility and composite performance.

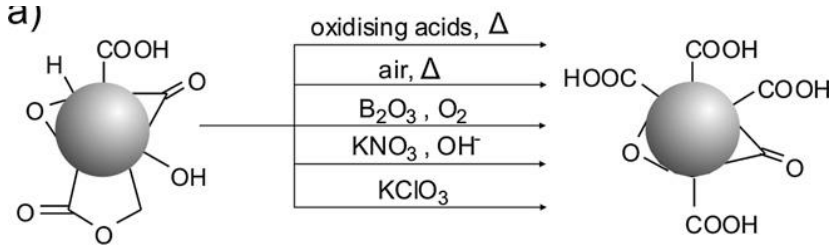

Figure 1.5. The surface of nanodiamond can be homogenized using different oxidative methods. [27].

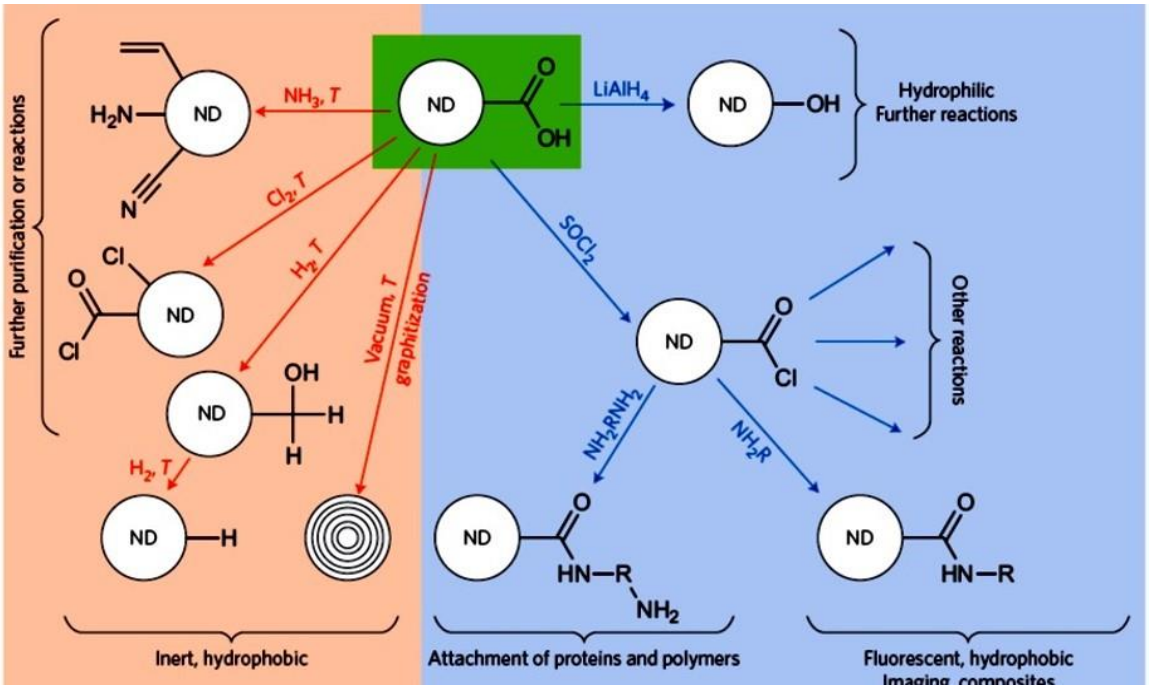

Figure 1.6. Different routes for nanodiamond surface modification; including high temperature gas treatments (red) and ambient-temperature wet chemistry techniques (blue) [24].

Several methods for the deagglomeration and solubilization of nanodiamond have been investigated so far, including mechanical methods such as attrition milling [26] and bead-assisted sonic disintegration (BASD) [32], as well as methods using non-covalent interactions [33] or functionalization [34]. When the mechanical deagglomeration technique is used, the primary particles can be isolated, and stable colloids in water or DMSO can be produced. Unfortunately the milling process contaminates the diamond colloids with abrasion debris from the milling beads (usually zirconia) and titanium (from sonotrode in the case of BASD). These contaminants are difficult to remove without losing the carbonaceous material. The non-covalent methods usually lead to reduced agglomerates in the range of 100-150 nm and do not form stable colloidal solutions unless large amounts of detergents are used. With regard to chemical methods, Khabashesku [34] and Krueger et al. [35] worked with different methods to yield agglomerates with a size of ~150 nm. Their methods (fluorination and reduction followed by silanization, respectively) produced covalently functionalized diamond materials, but stable colloidal solutions of very small nanoscale diamond particles could not be obtained.

Nanodiamond can also be modified through the chemistry of graphitic carbon, which is either present intrinsically or created through surface graphitization. Strong C-C bonds can be created between the graphitic shell and the surface group, whereas techniques that rely on the chemistry of nanodiamond functional groups usually produce C-X bonds (where X is N, O, S etc.) [24]. Nanodiamonds functionalized by phenyl radicals were produced by Kuznetsov et al. [36] by reducing graphenic edges of

annealed nanodiamond and reacting with aryl halides. It was further treated to produce water-soluble nanodiamonds with particle size as low as 164 nm. Yeap and coworkers reported on grafting of aryl moieties by Suzuki reactions [37]. Liang et al. [38] functionalized thermally annealed nanodiamond by C-C coupling of the partially graphitized diamond surface using aryl diazonium salts. The agglomerate size of the originally strongly bound detonation diamond (>0.5μm) was also reduced to ~20-50 nm by this method, without using mechanical techniques such as strong ultrasound or milling.

Purified ND is one of the few carbon based nanomaterials that has very high electrical resistivity due to its sp^3 electronic structure and absence of π electrons. One study found that DNDs were highly resistive until heated above 1100^0K, at which the point the resistivity dropped due to the formation of graphic phases [39]. Another investigation showed that at temperatures below 350^0C the investigated form of detonation nanodiamond was nearly an ideal dielectric [40].

1.4 Nanodiamond/Polymer Nanocomposites

The superior thermal conductivity and stability, excellent mechanical and electrical properties, outstanding tribological properties as well as the rich surface chemistry of nanoscale diamond particles make nanodiamond an excellent candidate filler material for polymer composites. The biocompatibility and chemical stability of the diamond core also make these composites very well suited for biomedical applications.

The following section (1.4.1) reviews prior studies of ND/polymer composites using polymers other than PEEK; section 1.4.2 reviews studies of ND/PEEK composites.

1.4.1 ND/Polymer Nanocomposites

Many studies have explored the addition of ND to polymers in order to improve mechanical properties. Only 0.6 wt% ND in poly(vinyl alcohol) (PVA) composite was found to increase hardness by 80% and elastic modulus by 100% [41]. Another ND/PVA study shows that after solution blending of only 1 wt% ND with PVA in water, nanocomposite films produced by casting had 250% increase in Young's modulus [42]. Alkyl functionalized ND has been blended with a low density polyethylene (LDPE) matrix [43]. Increasing the chain length of the alkyl group increased the interaction of ND with the LDPE. At a maximum ND content of 11 wt%, Young's modulus increased three-fold, and thermal properties improved significantly. A study of the effect of different ND surface functionalizations (hydroxyl, carboxyl, amino, and amide groups) on the mechanical properties of nanocomposites prepared in polycarbonate and poly(methyl methacrylate) (PMMA) matrices showed that while almost all functionalizations increased the Young's modulus to some degree, the amine or amide functionalization gave the best improvement in mechanical properties for both polymers [44].

Epoxy has been used as a polymer matrix for composites with a wide range of ND loadings (0-25 vol%). While small to moderate improvements in mechanical properties were observed at low ND loadings, an unprecedented 470% increase in Young's modulus and up to 300% increase in hardness were observed for the

nanocomposite with 25 vol% ND[45]. Another study with epoxy matrix shows that when only 0.3 wt% carboxylated/oxidized ND was efficiently dispersed in epoxy through a high powerful ultrasonincation and hear shear mixing, Vicker's hardness, tensile strength and tensile modulus of the nanocomposite increased by 24.7%, 52.7% and 54.2% respectively [46]. A multifunctional fluorescent composite bone scaffold material was prepared by solution mixing biodegradable poly (L-lactide acid) (PLLA) material with up to 10 wt% hydrophobic octadecylamine-functionalized nanodiamond (ODA-ND). Almost an order of magnitude increase in hardness, together with reduced creep and three times higher Young's modulus were found for composites containing 10 wt% ODA-ND [47]. ND/poly(lactic acid) (PLA) (0.1-5%) nanocomposites prepared by melt-blending showed a 75% increase in storage modulus (E') at 3 wt% ND. An increase in tensile strength was noticed as well [48].

Due to its extremely high thermal conductivity (~2000 W/mK) [42], ND has been used as a filler to increase the thermal conductivity of nanocomposites. Addition of only 1 wt% ND in a PVA matrix in aqueous media resulted a 25% increase in thermal conductivity of a nanocomposite film produced by solution casting [42]. In a microelectronic application, the addition of only 2 wt% ND increased the thermal conductivity of PDMS (polydimethylsiloxane) up to 15% [49]. Addition of 25 vol% ND in an epoxy matrix increased the thermal conductivity of the nanocomposite by almost 25% [45].

ND has also been used to increase the thermal stability of polymer nanocomposites. In microelectronic applications, addition of 1-2 wt% ND to a polyimide matrix increased the composites' thermal degradation temperature by up to 30^0C [49]. A study of melt compounded ND/PLA nanocomposites also showed an increased decomposition temperature [48].

Nanodiamond has also been used for tribological applications. Only 2 wt% ND in PTFE (polytetrafluoroethylene) reduced the coefficient of friction from 0.12 to 0.08 [50]. Addition of 25 vol% ND in an epoxy matrix reduced the coefficient of friction of the nanocomposite by almost 40% [45].

Symmetric supercapacitors containing ND/PANI (polyaniline) nanocomposite electrodes with 3-28% low cost detonation ND showed dramatically improved cycle stability and higher capacitance retention at fast sweep rate than pure PANI electrodes [51].

1.4.2. ND/PEEK Composites

There have been just a few studies of composites prepared with ND and polymers from the PEK family. Nanodiamond has been used to improve the poor mechanical properties of SPEEK (Sulfonated polyetherether ketone) in proton exchange membrane fuel cell (PEMFC) applications [52]. In this study, researchers used ND as a reinforcing agent and took advantage of thermal crosslinking of $-SO_3H$ groups to improve the mechanical properties of SPEEK membranes. This strategy helped resolve the key issue of SPEEK membranes, namely that high degree of sulfonation needed for

high conductivity usually results in poor mechanical properties. ND also moderately improved the thermal stability of the nanocomposite without reducing the proton conductivity of SPEEK.

A recent study [25] demonstrated arylcarbonylation and grafting of DND (detonation nanodiamond) nanoparticles with PEK (polyether ketone) polymer via *in situ* Friedel-Crafts polycondensation reaction in a polyphosphoric acid medium. The success of the grafting reaction was demonstrated by SEM and TEM analysis, showing that the nanoparticles were well dispersed within the polymer. The nanocomposites were found to be soluble in solvents such as NMP and THF and displayed remarkably higher viscosity and T_g values than the neat polymer. Moreover, the composites exhibited considerably higher thermal stability than PEK in both nitrogen and air.

1.5 Overview of Dissertation

The objectives of this project are to explore new routes for surface functionalization of nanodiamond (ND), develop methods for maximizing dispersion of ND as a nano-scale filler in poly(ether ether ketone) (PEEK), and characterize the effect of dispersed ND on the mechanical, thermal and dielectric properties of ND/PEEK composites.

Our preliminary efforts to disperse unmodified and various surface-modified NDs (as received from suppliers) in PEEK were unsuccessful due to ND agglomeration and low thermal stability. Thus we began to explore chemical grafting of phenylphosphonate (PPA) onto ND, hypothesizing that the phenyl functional group

would render the ND more compatible with aromatic PEEK. This research, including detailed characterization of the PPA-modified ND, are presented in chapter 2.

Chapter 3 describes the preliminary study of melt-blending as-received ND with PEEK, as well as the more comprehensive study of melt-blending of PPA-modified ND with PEEK. This chapter includes detailed characterization of the ND/PEEK nanocomposites and comparison with pure PEEK properties.

Chapter 4 describes two other routes we explored to produce ND/PEEK composites with an objective to maximize dispersion quality. In the first approach, PEEK was converted to hydroxylated PEEK (HPEEK) by carbonyl reduction. Then an attempt was made to covalently graft HPEEK onto carboxylated nanodiamond (CND). In the second method, some initial experiments were performed to use poly(1-4-phenylene ether-ether sulfone) (PEES) and polyetherimide (PEI) as surfactants to better disperse ND in PEEK.

CHAPTER 2

SURFACE FUNCTIONALIZATION OF NANODIAMOND WITH PHENYLPHOSPHONATE[1]

This work explores arylation of oxidized nanodiamond (OND) and carboxylated nanodiamond (CND) using phenylphosphonate (PPA) to produce PPA-grafted nanodiamond (PPA@ND). The specific hypothesis is that PPA can be readily grafted onto the surfaces of OND and CND particles via the nanodiamonds' reactive oxygen-rich surface functional groups.

The research explores the effect of varying reaction conditions (reactant ratio, heat, sonication) on PPA graft density and grafting mode. The products were characterized by a variety of techniques including: ^{31}P MAS NMR and FTIR to confirm PPA grafting, XPS to estimate PPA grafted amounts, and TGA to assess thermal stability. The utility of PPA functionalization for improving ND dispersion in organic solvents was evaluated using dynamic light scattering.

[1] This work was previously published in the *Journal of Colloid and Interface Science* **450**, 301-309 (2015) and is reproduced here with publisher permission.

The results confirm PPA grafting on both OND and CND, quantify the extent of PPA grafting, and suggest primarily bidentate grafting. For PPA grafting on OND, the grafted amount does not depend on PPA:ND ratio, application of heat, or use of sonication. The grafted amount of PPA on CND was significantly lower than that on OND. TGA data indicates that grafted PPA improves the thermal stability of both OND and CND. The starting OND disperses in water as aggregates with approximately 100 nm particle size. However, PPA-grafted OND does not disperse at all in water: thus grafted PPA changes the ND surface from hydrophilic to hydrophobic. PPA@OND prepared without sonication does not completely disperse in either DMF or toluene. Only PPA@OND prepared with sonication disperses well in these solvents, suggesting that sonication promotes more complete exposure of the ND surface to PPA grafting.

2.1. Introduction

Nano-scale diamond particles were first produced by detonation synthesis in the 1960's in the former USSR [23]. More recently, interest in nanodiamonds (NDs) has grown dramatically due to their relatively small particle size, narrow size distribution, tunable surface chemistry, and chemical inertness. Moreover, NDs exhibit remarkable mechanical, electronic, thermal, and tribological properties giving this novel form of carbon significant potential as a component of high performance multifunctional materials.

A variety of methods have been used to synthesize ND including detonation synthesis, laser ablation, high-energy ball milling, plasma-assisted chemical vapor

deposition (CVD), autoclave synthesis from supercritical fluids, chlorination of carbides, iron irradiation of graphite, electron irradiation of carbon onions, and ultrasound cavitation. Among these methods, commercial production employs only detonation synthesis, laser ablation, and high-energy ball milling. The majority of ND is produced via detonation synthesis using a mixture of trinitrotoluene (TNT) and hexogen [24, 38]. Detonation nanodiamond (DND) is also known by two other common names, ultra-dispersed diamond (UDD) and ultra-nanocrystalline diamond (UNCD) particulate.

Detonation synthesis produces detonation soot, a mixture of primary diamond particles (4-5 nm diameter) with other carbon allotropes and impurities. Primary DND particles have very large specific surface area (>>200 m^2/gm) [25]. The oxidation process used to purify the nanodiamond and remove the non-diamond carbon and non-carbon impurities also removes various functional groups from the nanodiamond surface and produces oxygenated surface species such as $–CO_2H$ (carboxylic acids), lactones, C=O (keto carbonyls), anhydrides, and –OH (hydroxyls) [26]. As a result, DND surfaces are polar and hydrophilic.

Despite this, primary DND particles tend to agglomerate into much larger aggregates with sizes ranging from a few hundred nanometers (“core agglutinates”) to a few tens of microns (“agglomerates”) [28]. This agglomeration occurs not only due to van der Waals and electrostatic (Coulombic) interactions, but also chemical bonding. Interparticle hydrogen bonding and formation of ester, ether, and anhydride bonds are believed to play important role in DND primary particle agglomeration. Nanodiamond

agglomeration can be partially reversed via ultrasonic treatment [24, 29]: large agglomerates can be broken down into 100-200 nm aggregates, but further dis-aggregation into 4-5 nm primary particles has not been achieved [30]. Although aggregated NDs can be useful in applications such as chromatography or drug delivery [24], dis-aggregation into individual primary particles might enable formulators to take full advantage of ND surface properties.

To this end, several methods for ND dis-aggregation and solubilization have been investigated, including mechanical methods such as attrition milling [26] and bead-assisted sonic disintegration (BASD) [32], as well as methods using non-covalent interactions [33] or chemical functionalization [34]. When mechanical methods are used, some primary particles can be isolated, and stable colloidal suspensions in water or DMSO can be produced [26, 32]. Unfortunately, the milling process contaminates ND colloids with abrasion debris, typically zirconia (from milling beads) or titanium (from the sonotrode in the case of BASD). Such contaminants are difficult to remove without sacrificing the carbonaceous material. The methods based on non-covalent interactions usually lead to reduced agglomerates in the range of 100-150 nm but do not form stable colloidal solutions without the use of large amounts of detergents. Chemical methods, including fluorination [34] and reduction followed by silanization [35], produced covalently functionalized ND materials with aggregate size on the order of ~150 nm, but these studies did not yield stable colloidal suspensions of primary ND particles.

A distinct feature of nanodiamonds, in contrast with carbon nanotubes and other graphitic nanoparticles, is that NDs can be readily functionalized in many ways, enabling sophisticated surface functionalization without compromising the useful properties of the ND core [31]. Covalent surface modification of NDs aims to introduce suitable functional groups to improve ND processability and impart, enhance, or tailor certain properties. At the same time, it is critical to understand how ND surface functional groups influence interparticle interactions, especially with regard to detrimental outcomes such as aggregation [27].

Various functional groups on the surfaces of as-prepared, commercial ND powder can be used for covalent functionalization. Nanodiamond can be modified through the chemistry of graphitic carbon, present intrinsically or created through surface graphitization. Strong C-C bonds can be created between the graphitic shell and the surface group, but these approaches require harsh conditions [24]. Phenyl-functionalized ND has been produced by reducing graphenic edges of annealed nanodiamond and reacting it with aryl halides [36]. Further treatment using oleum produced water-soluble ND with particle sizes as low as 164 nm. Suzuki reactions have also been used to graft aryl moieties [37]. Thermally annealed ND was functionalized by C-C coupling of the partially graphitized diamond surface using aryl diazonium salts. The agglomerate size was reduced to ~20-50 nm by this method, without using mechanical techniques such as strong ultrasound or milling [38].

In many cases, carboxylated ND (produced by air, ozone or acid purification) provides a convenient starting point, taking advantage of the rich chemistry of COOH groups. These routes usually produce C-X bonds (where X is N, O, S etc.) [24]. For example, COOH and other surface functional groups on ND were successfully reduced with lithium aluminum hydride to produce ND-OH [53]. Carboxylated ND was covalently linked with octadecylamine (ODA) to produce hydrophobic blue fluorescent ND material (ND-ODA) [54]. Heating carboxylated ND in ammonia can result in the formation of variety of surface groups including NH_2, C-O-H, C≡N, and groups containing C=N. Heating carboxylated ND in chlorine gas produces acylchlorides; treatment in hydrogen completely reduces C=O to C-O-H and forms additional C-H groups [24].

To date, phosphonate coupling agents have not been explored for the surface functionalization of ND. Phosphonic acids have been widely used to modify titania, zirconia, and indium tin oxide surfaces [55-57]. Organophosphonates have also been used to tailor the surface chemistry of barium titanate and related perovskite-type metal oxide nanoparticles to facilitate their dispersion in various host matrices [58]. Recently, we demonstrated phenylphosphonate functionalization of exfoliated calcium niobate platelets [59]. Covalent coupling between organophosphonates and metal oxide surfaces occurs either by heterocondensation with surface hydroxyl groups or coordination to metal ions on the surface. Various binding modes (mono-, bi-, and tri-dentate) can be identified through ^{31}P MAS NMR and other spectroscopic methods [56, 59].

In this work, we explore arylation of ND using phenylphosphonate (PPA). Functionalization studies utilized both oxidized and carboxylated DND agglomerates as the starting materials. The primary goal of this work is to demonstrate surface functionalization of ND with an organophosphonate. A secondary goal is to assess the utility of this functionalization method for improving ND dispersion as primary particles in solvents and (ultimately) polymer hosts.

2.2 Experimental Section

2.2.1. Materials

Phenylphosphonic acid (98%) was purchased from Sigma-Aldrich and used as received. Oxidized nanodiamond (O-ND) and carboxylic acid modified nanodiamond (C-ND) were purchased from NanoBlox, Inc. and used as received. BET measurements indicate specific surface areas of 283 and 327 m^2/g for OND and CND, respectively.

2.2.2. Chemical Functionalization

Functionalization of O-ND with PPA begins with dissolution of PPA in deionized (DI) water with mild heating, followed by addition of O-ND powder to the solution. Two formulations were studied, employing 3:5 and 1:9 ratios of PPA:ND by weight (Table 2.1). The PPA+ND mixture was refluxed at ~100°C for 48 h, followed by heating on a hot plate to drive off the water. A control sample, "$PPA_{1:9}$@OND(unh)", was prepared with PPA:ND = 1:9 but without reflux or heat. This product suspension was freeze-dried using a lyophilizer. In all cases, the dried product was washed with DI water several

times to remove unreacted PPA. For each washing stage, after adding water and stirring, the product was centrifuged, and the supernatant solution was decanted and saved for UV-vis analysis. UV-vis spectra for the supernatant solutions from each wash stage were compared against spectra for solutions with known PPA concentrations. In this way, it can be demonstrated that the washing procedure removed virtually all unreacted PPA from the product. The same procedure was used to functionalize CND with PPA.

Preparation of one sample followed a different procedure. PPA was dissolved in DI water with mild heating followed by addition of O-ND (3:5 PPA:ND by weight). Instead of refluxing, the suspension was heated on a hot plate for 22 h with replenishment of DI water to make up for evaporation. In addition, energy was supplied to the suspension over the 22 h using a sonic horn (Sonics Vibracell VCX 500). The "$PPA_{3:5}$@OND(son)" product was not dried; instead, it was centrifuged and then washed repeatedly with DI water to remove unreacted PPA. Table 2.1 lists all samples considered in this work. The generic label "PPA@ND" denotes PPA-functionalized ND. TEM images of OND, CND and $PPA_{3:5}$@OND(son) can be found in Appendix A.

2.2.3. Characterization Methods

Solid-state ^{31}P MAS NMR spectra were collected on either a Varian Inova 500 MHz or a Bruker Avance III-HD 500 MHz spectrometer (202.49 MHz). The Varian spectrometer used a Doty Scientific 4mm XC MAS probe. These spectra were collected

at ambient temperature with a sample rotation rate of 10 kHz and TPPM decoupling at a ^{1}H field strength of 64 kHz. The Bruker system was fitted with a 1.9 mm MAS probe.

Table 2.1. List of samples with preparation conditions for PPA functionalization of OND and CND.

Sample Name	**PPA:ND**	**ND Type** (a)	**Conditions**
$PPA_{3:5}OND$	3:5	OND	reflux 48 h
$PPA_{1:9}OND$	1:9	OND	reflux 48 h
$PPA_{1:9}OND$(unh)	1:9	OND	unheated: stirred 48 h, freeze-dried
$PPA_{3:5}OND$(son)	3:5	OND	heated on hot plate with sonication (22 h)
$PPA_{3:5}CND$	3:5	CND	reflux 48 h
$PPA_{1:9}CND$	1:9	CND	reflux 48 h

(a) OND = oxidized nanodiamond; CND = carboxylated nanodiamond

These spectra were collected at ambient temperature with a sample rotation rate of 20 kHz. ^{1}H dipolar decoupling was performed with SPINAL64 modulation and 145 kHz field strength. Bloch decays were collected with 50 ms acquisition time over 300 or 400 ppm spectrum width with a relaxation delay of 10 s. Chemical shifts are reported with respect to H_3PO_4 and referenced externally with $NH_4 \cdot H_2PO_4$, which was assigned a value of 0.72 ppm.

XPS measurements employed a Kratos AXIS Ultra DLD XPS system equipped with a monochromatic Al Kα source. The energy scale of the system is calibrated using a Au foil with Au_4f scanned for the Al radiation and a Cu foil with Cu_2p scanned for Mg radiation resulting in a difference of 1081.70 ± 0.025 eV between these two peaks. The

binding energy is calibrated using an Ag foil with $Ag_3d_{5/2}$ set at 368.21 $\pm$ 0.025 eV for the monochromatic Al X-ray source. The monochromatic Al Kα source was operated at 15 keV and 120 W. The pass energy was fixed at 40 eV for the detailed scans. A charge neutralizer (CN) was used to compensate for the surface charge.

FT-IR spectra were recorded on a Thermo Nicolet Nexus 470 using an ATR diamond cell attachment. Thermogravimetric analyses (TGA) were performed using a Mettler Toledo TGA/SDTA851. TGA samples were heated either in air or N_2 from room temperature to 900°C using a heating rate of 10°C/min. UV-vis data were collected using a Cary 100 UV-visible spectrophotometer.

Dynamic light scattering (DLS) data were collected using a ALV/CGS-3 precision compact goniometer system. Most DLS tests were performed on samples consisting of 5 mg of PPA@ND sample suspended in 50 mL of solvent. Each suspension was bath sonicated for 8 h and then allowed to settle for 12 h. Each suspension was characterized by DLS "as-made" (after 12 h settling) as well as immediately after filtration using 0.2 μm ePTFE filters.

2.3. Results and Discussions

2.3.1. Purification of PPA@ND Products

Repeated centrifugation and washing steps were used to remove unreacted PPA from PPA@ND grafting products. Figure 2.1 shows UV-vis spectra for supernatant solutions (solid lines) collected during a sequence of multiple washes of $PPA_{3:5}$@OND

product. The supernatant from the first wash shows very strong absorbance in the 230-280 nm range, indicating high PPA concentration. This is unsurprising, considering that the synthesis of $PPA_{3:5}$@OND employed excess PPA, most of which should wash out from the product. The absorbance values decrease dramatically in the UV-vis spectra for supernatant solutions from subsequent washes. The UV-vis spectrum for the fifth supernatant solution lies well below that for 0.01% PPA solution. Thus the supernatant from the fifth wash has a PPA concentration significantly below 0.01%. More generally, the results in Figure 2.1 demonstrate that the washing procedure effectively removes non-grafted PPA from PPA@ND products.

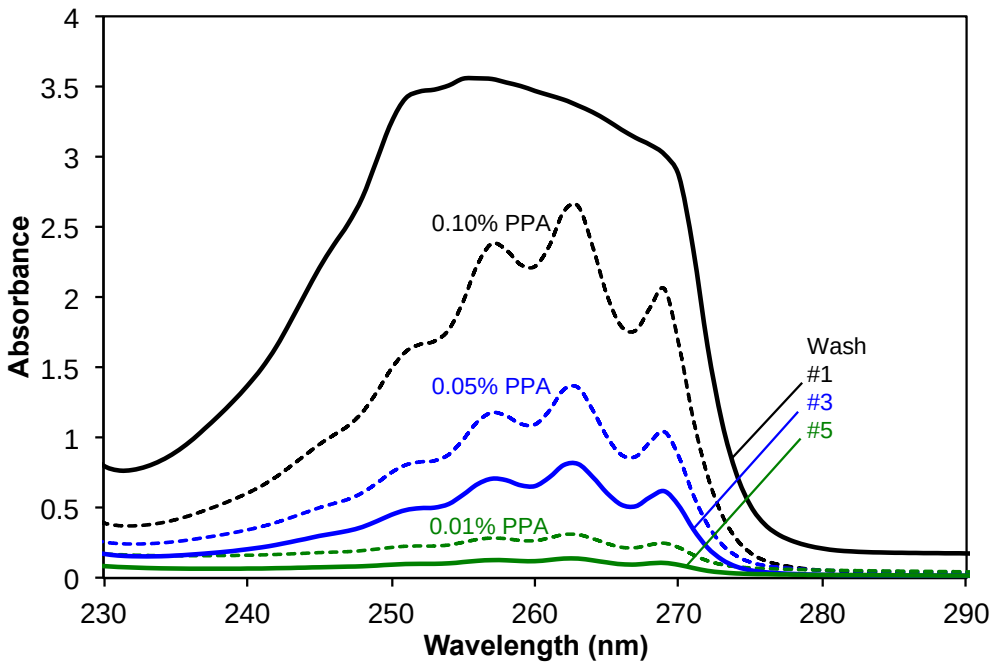

Figure 2.1. UV-vis spectra for supernatant solutions (solid curves) collected during a sequence of five washes of $PPA_{3:5}$@OND. Also shown are three spectra for three PPA solutions with known concentrations as indicated (dashed curves).

2.3.2. PPA Grafting on OND and CND

2.3.2.1. PPA Grafting on OND

Figure 2.2 shows the ^{31}P NMR spectra of pure PPA, $PPA_{3:5}$@OND before washing, and $PPA_{3:5}$@OND after washing. The NMR spectrum for pure PPA (Figure 2.2a) has a signature peak at 21.4 ppm. This peak also appears in the spectrum of "pre-washed" $PPA_{3:5}$@OND (Figure 2.2b), indicating the presence of considerable non-grafted PPA in the sample. However, the spectrum for "post-washed" $PPA_{3:5}$@OND (Figure 2.2c) shows no evidence of the signature peak associated with pure PPA. This observation is consistent with the UV-vis results (Figure 2.1) demonstrating that the washing procedure removed non-grafted PPA. Each of the NMR spectra for $PPA_{3:5}$@OND (Figure 2.2b, c) also displays a dominant peak shifted 10-11 ppm upfield from the peak for pure PPA, consistent with covalent grafting of PPA onto the OND surface. This conclusion is consistent the findings of recent study of PPA grafting onto layered calcium niobate and many earlier studies cited therein [59].

Figure 2.3 shows ^{31}P NMR spectra of various washed PPA@OND samples. None of the spectra have a peak near 21 ppm, demonstrating the absence of non-grafted PPA. Each of the spectra has a peak in the range of 10-15 ppm, indicating PPA grafting onto OND. The spectra for some samples (Figure 2.3a, 2.3c) may have a weaker secondary peak further upfield in the 0-5 ppm range, suggesting an additional binding mode. Samples showing this secondary peak include PPA@OND prepared with the higher ratio (3:5, Figure 2.3a) as well as $PPA_{1:9}$@OND prepared without any heating during the

reaction or purification stages (Figure 2.3c). The spectrum for the latter sample shows that PPA grafts onto OND at room temperature without the need for reflux or heating of any kind. Likewise, Figure 2.3d shows that addition of energy during the reaction via sonication does not have an impact on the mode of PPA grafting at least based on the peak shift in the ^{31}P NMR spectrum.

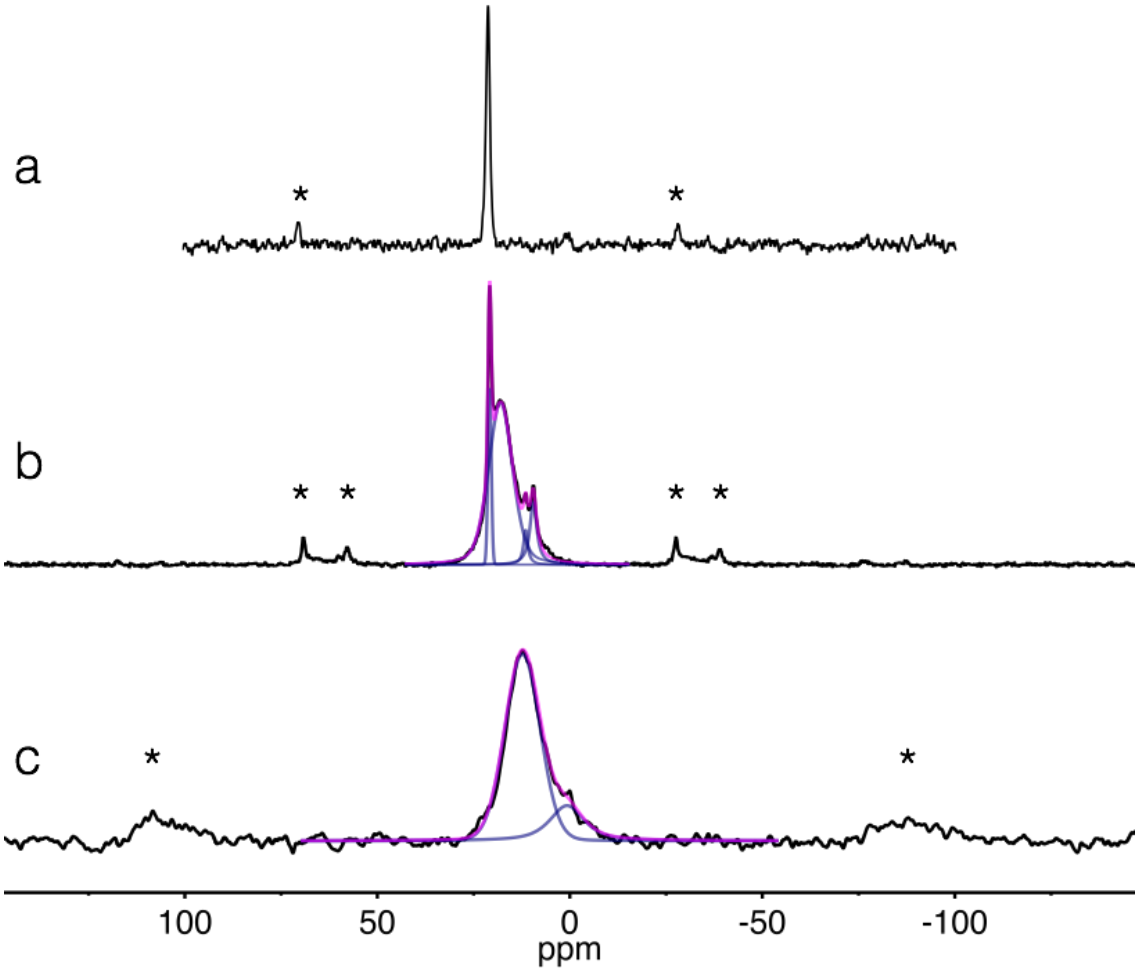

Figure 2.2. ^{31}P MAS NMR spectra with peak fitting for: (a) pure PPA, (b) $PPA_{3:5}$@OND before washing, and (c) $PPA_{3:5}$@OND after washing. Asterisks (*) denote spinning side bands.

XPS characterization provides elemental compositions that can be used to estimate the amounts of grafted PPA (Table 2.2). Both OND and CND are primarily carbon, as expected, but also have significant oxygen content arising from polar surface groups. The "pre-washed" $PPA_{3:5}$@OND has a high phosphorus content, but the post washed sample has a much lower phosphorous content consistent with the removal of non-grafted PPA. All of the PPA@OND samples have similar phosphorus contents,

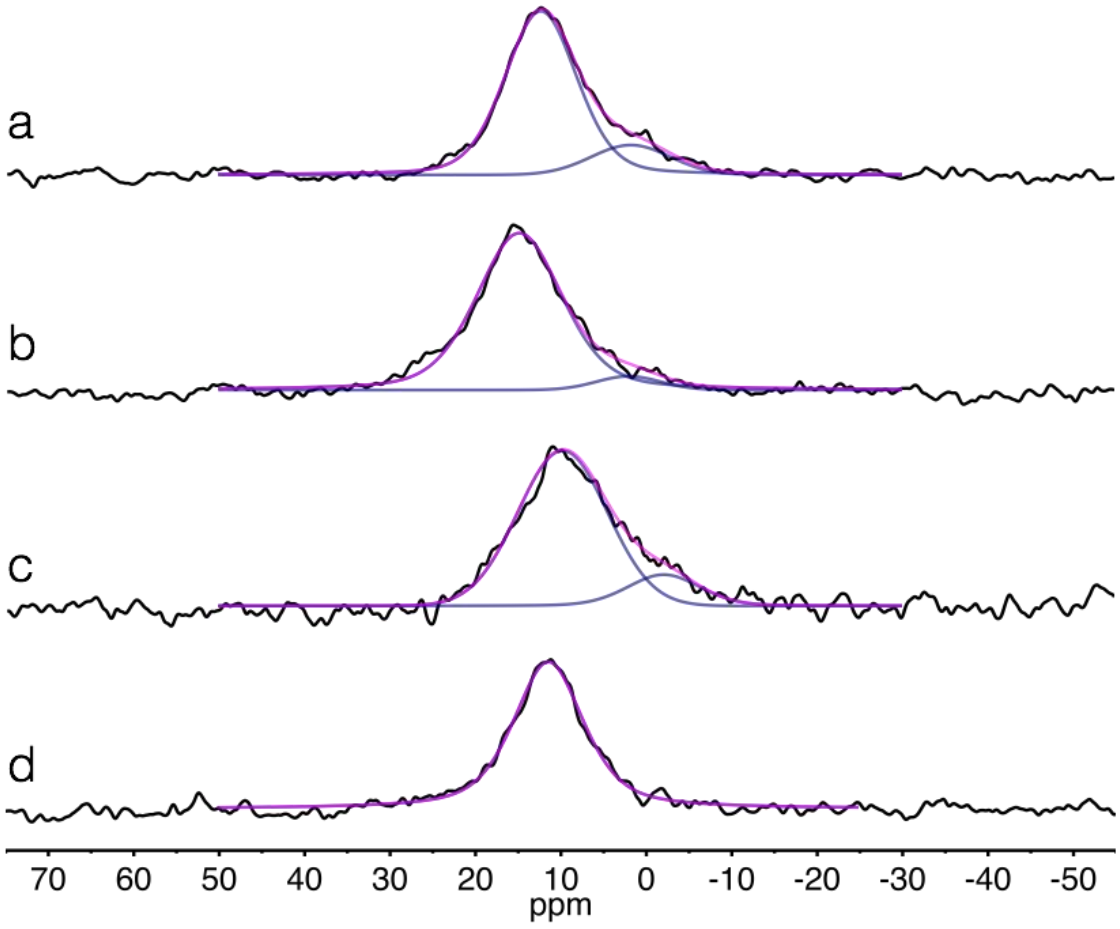

Figure 2.3. ^{31}P MAS NMR spectra with peak fitting for: (a) $PPA_{3:5}$@OND, (b) $PPA_{1:9}$@OND, (c) $PPA_{1:9}$@OND(unh), and (d) $PPA_{3:5}$@OND(son).

apparently independent of the PPA:ND ratio, application of heating, or use of sonication during the reaction. Using OND's measured BET surface area of 283 m^2/g, the PPA@OND products have PPA graft densities of approximately 0.57/nm^2. The reciprocal value, known as the parking area, is about 1.75 nm^2 per grafted PPA molecule. This value is larger than the 0.24 nm^2 value reported previously for PPA grafting onto calcium niobate [59] and other kinds of metal oxide surfaces. In previous work, the packing density of grafted PPA molecules on the surfaces was thought to limit the amount of PPA grafting. In the case of OND, it is possible that PPA cannot reach all of the surface area identified through BET measurement. Alternately, the surface density of grafting sites on the OND may limit PPA grafting.

2.3.2.2. PPA Grafting on CND

The ^{31}P NMR spectra of washed PPA@CND samples (Figure 2.4) have primary peaks located at 11.1 and 11.5 ppm consistent with PPA grafting and the absence of non-grafted PPA. Deconvolution of the spectrum for $PPA_{3:5}$@CND suggests the possibility of a second upfield peak at 1.2 ppm, but noise in the data makes it uncertain if this represents a second binding mode. XPS analysis (Table 2.2) indicates that PPA grafted amounts on CND are 25-50% lower than for PPA@OND; the corresponding parking areas are 2-4 times higher. Either the CND's surface –COOH groups are poor reaction sites for PPA, or the –COOH groups create an unfavorable, mutually repulsive interaction with acidic PPA. The PPA grafted amount for $PPA_{1:9}$@CND appears to be twice as high as than for $PPA_{3:5}$@CND, despite the lower PPA:ND ratio used in the

former. The reasons for this observation are not obvious; however, this trend (higher PPA grafting for 1:9 PPA:ND) may also be observed for PPA grafting on OND.

Table 2.2. Composition of PPA@ND samples determined from XPS characterization.

Sample ID	**Mass %**			**Graft Density**		**Parking Area**
	P (2p)	C (1s)	O (1s)	mmol PPA/g ND	1/nm^2 (a)	nm^2 (b)
OND	0.00	87.96	12.04	n.a.	n.a.	n.a.
CND	0.00	88.36	11.64	n.a.	n.a.	n.a.
$PPA_{3:5}OND$ (pre-wash)	6.75	73.97	19.28	n.a. (c)	n.a. (c)	n.a. (c)
$PPA_{3:5}OND$	0.79	86.41	12.80	0.27	0.575	1.74
$PPA_{1:9}OND$	0.86	86.73	12.41	0.29	0.617	1.62
$PPA_{1:9}OND$(unh)	0.77	86.34	12.89	0.26	0.553	1.81
$PPA_{3:5}OND$(son)	0.72	86.58	12.70	0.24	0.511	1.96
$PPA_{3:5}CND$	0.18	87.98	11.83	0.059	0.109	9.20
$PPA_{1:9}CND$	0.37	87.07	12.57	0.12	0.221	4.52

(a) PPA molecules per nm^2 based on measured BET surface areas of 283 m^2/g (OND) and 327 m^2/g (CND).

(b) Reciprocal of graft density: ND surface area occupied by each grafted PPA molecule.

(c) Not applicable because most of the PPA is not grafted, as shown in Figures 2.1 and 2.2.

2.3.3. Analysis of PPA@ND Grafting

FTIR spectroscopy permits characterizing the changes in surface functional groups associated with PPA grafting on ND particles. The OND material was acid treated by manufacturer to increase the number of carboxylic acid groups and produce CND. Unsurprisingly, the FTIR spectra of the two as-received materials (Figure A1, Appendix) are similar. The spectrum for CND has a broader absorbance peak centered at ~3450 cm^{-1} due to additional O-H-stretch vibrations in part from –COOH but especially from

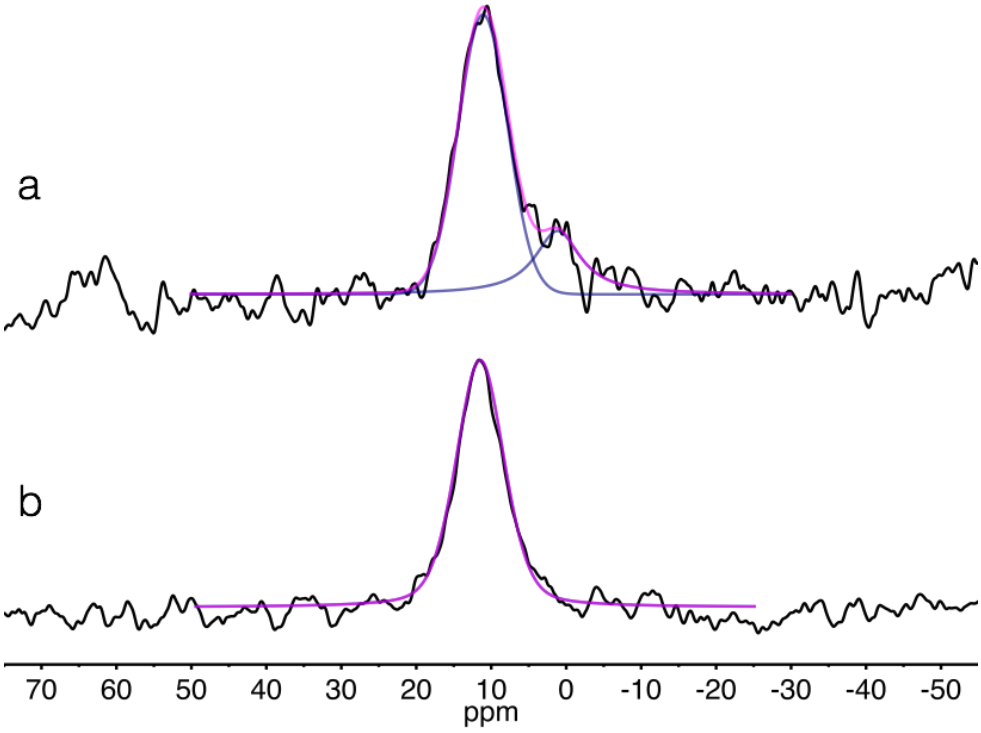

Figure 2.4. ^{31}P MAS NMR spectra with peak fitting for (a) $PPA_{3:5}$@CND and (b) $PPA_{1:9}$@CND.

additional water adsorbed to the surface. The FTIR absorption spectra of OND and CND (Figure A1, Appendix) both show characteristic bands between 1680 and 1780 cm^{-1} with maxima usually around 1730 cm^{-1}. These bands can be attributed to carbonyl functions like ketones, aldehydes, and carboxylic groups (esters, lactone, acids) generated by the oxidation of the surface [60, p. 355].

Figure 2.5 shows FTIR spectra of the starting materials and products of PPA grafting onto OND. Pure PPA has several strong, distinctive bands with assignments listed in Table 2.3. The spectra for the washed PPA@OND products manifest some of the same bands as PPA specifically the aromatic C-H and C-C vibrations associated with the PPA phenyl ring (bands 1, 5, and 7 in Table 2.3). The presence of these bands in the spectra for the washed PPA@OND products is consistent with bound PPA in PPA@OND, although it does not prove covalent grafting. On the other hand, certain FTIR bands for PPA are missing or significantly reduced in the spectra for the PPA@OND products. In particular, the PPA bands at 941 and 1014 cm^{-1} due to P-OH stretching, and the band at 1220 cm^{-1} due to P=O stretching, are not apparent in the spectra for the PPA@OND products. This observation implies that PPA's P-OH and P=O groups are involved in covalent grafting of PPA on OND, consistent with the shifts observed in the ^{31}P NMR spectra (Figure 2.3).

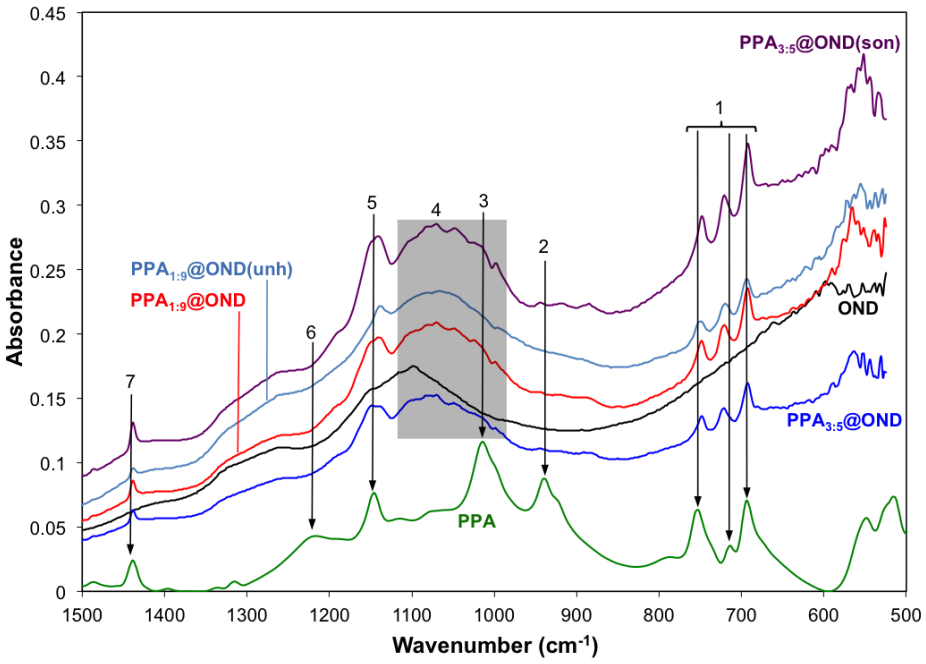

Figure 2.5. FTIR spectra for PPA, OND, and PPA@OND products. The PPA spectrum has been rescaled for visual clarity. Table 2.3 lists band (peak) assignments.

Comparing the spectra for PPA@OND and OND in the 850-1100 cm^{-1} range (Figure 2.5) suggests the appearance of new absorbance bands in the products. This can be more carefully quantified by taking the difference in absorbance between the product and starting OND spectra. Figure 2.6 shows one example, comparing the "$PPA_{1:9}$@OND – OND" difference spectrum with the full FTIR spectrum for PPA. Two features may be noted. First, peaks "2" and "3" associated with P-OH in PPA, as well as peak "6" due to P=O, may not be completely absent in the $PPA_{1:9}$@OND spectrum. The latter, although diminished, may be present in the $PPA_{1:9}$@OND spectrum but shifted to ~1190 cm^{-1}. This observation suggests that some P-OH and P=O groups may still be present in the $PPA_{1:9}$@OND product. Second, the difference spectrum shows a broad

band (labeled "4" in Figures 2.5 and 2.6) spanning 950-1100 cm^{-1}, consistent with P-O-C vibrational modes (see Table 2.3 for references). This provides direct evidence of the conversion of P-OH and P=O groups to P-O-C linkages.

Table 2.3. Band assignments for numbered peaks in the FT-IR spectra shown in Figures 2.5, 2.6, and A2 (Appendix).

No.	**σ (cm^{-1})**	**Source**	**Mode** (a)	**References**
1	694, 714, 752	PPA	arom. C-H	[61-65]
2	941	PPA	P-OH	[62, 63, 66, 67]
3	1014	PPA	P-OH	[62-64, 66-72]
4	950-1100	PPA@OND	P-O(-C)	[61, 63, 67-69, 72]
5	1145	PPA	P-C	[62, 67-69, 72]
6	1220	PPA	P=O	[62,63, 66-71, 73]
7	1438	PPA	arom. C-C	[63-65, 67]

(a) Abbreviations: oop = out-of-plane bending; arom. = aromatic.

FTIR spectra for CND and PPA@CND products may be found in Supporting Information (Figure A2, Appendix). In brief, the spectra for PPA@CND products are very similar to those for PPA@OND products. Thus FTIR results also verify PPA grafting on CND with involvement of the same functional groups.

Finally, with regard to the mode of PPA binding on ND, the NMR and FTIR data do not permit definitive conclusions to be made. The FTIR spectra (Figures 2.5 an A2) suggest that low amounts of residual P-OH and P=O groups may be present in the PPA@ND products. The ^{31}P NMR spectra (Figures 2.3 and 2.4) suggest one dominant mode in most cases. The previous analysis of chemical shifts in ^{31}P NMR spectra

suggests upfield shifts of 4 ppm or more for dialkyl esters of PPA [74, p. 29], and an absolute shift of 11.2 ppm for the cyclic propyl ester of PPA [74, p. 42]. Based on the NMR and FTIR data presented in this work as well as these citations, we believe that PPA grafts onto the ND surface primarily in the bidentate mode, involving both P-OH and P=O groups (Figure 2.7). In some cases, a small amount of PPA may graft in the tridentate mode, as evidenced by the smaller upfield peak observed near 0 ppm in some of the spectra. Considering the complexity of ND surface chemistry [24, 27], the reactions illustrated in Figure 2.7 are speculative and representative of many possible grafting reactions involving oxygen-containing groups and graphitic carbon at the ND surface.

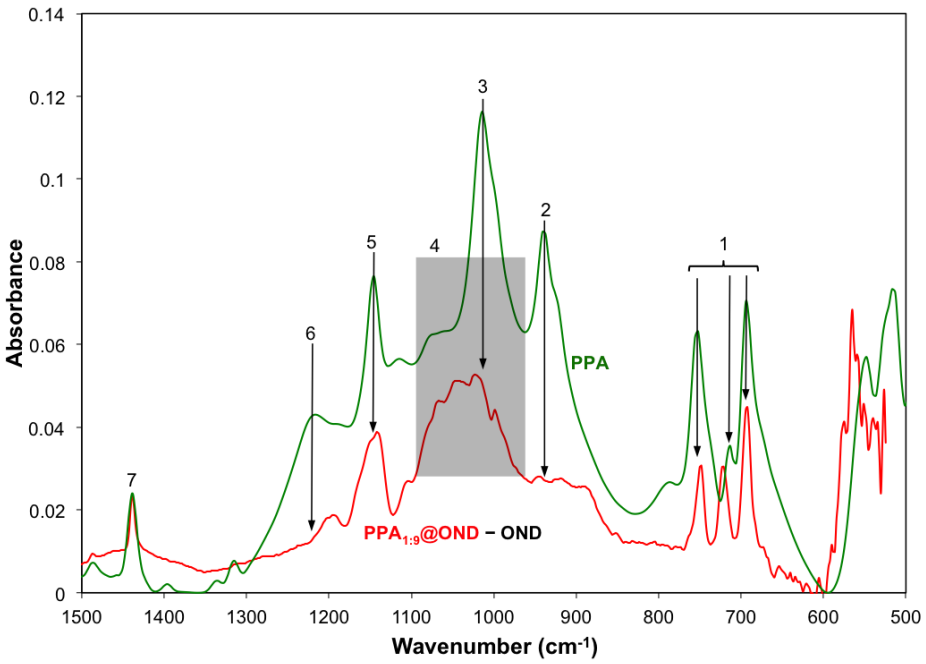

Figure 2.6. FTIR spectrum for $PPA_{1:9}$@OND after subtraction of the OND spectrum ("$PPA_{1:9}$@OND – OND"), compared with the full spectrum for PPA. The PPA spectrum has been rescaled for visual clarity. Table 2.3 lists band (peak) assignments.

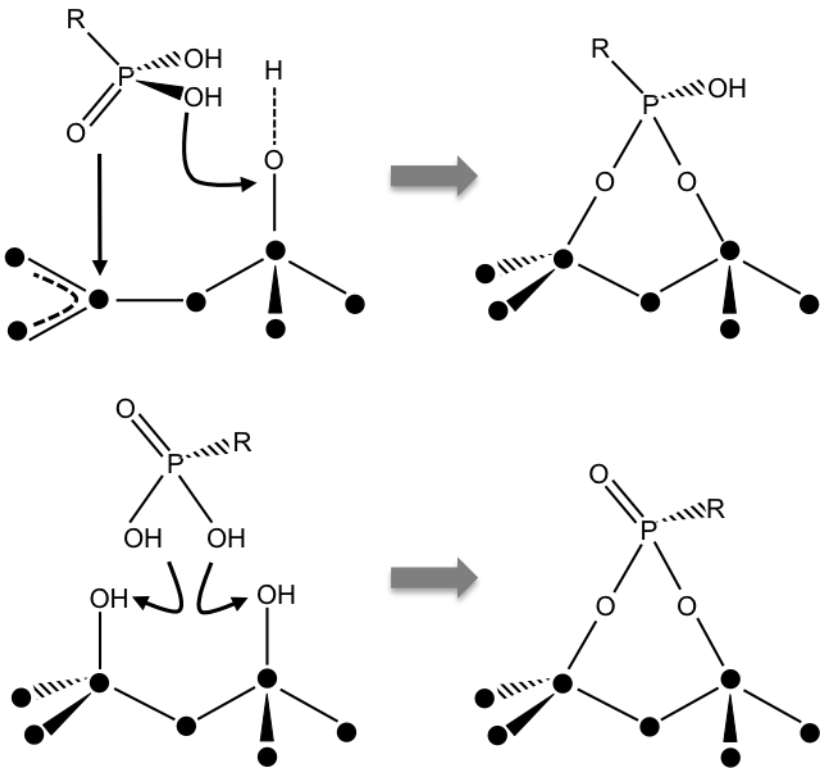

Figure 2.7. Schematic illustration of two possible reactions between organophosphonate and the ND surface, resulting in bidentate grafting. Filled circles denote ND carbon atoms. In the first reaction (top), the P=O group reacts with graphitic carbon, and one of the phosphonate hydroxyls undergoes condensation with a surface hydroxyl. In the second reaction (bottom), both phosphonate hydroxyls undergo condensation with surface hydroxyls.

2.3.4. Thermal Stability of PPA@ND

The thermal stability of PPA@ND materials was evaluated using TGA (Figure 2.8). All of the samples show a weight loss of 3 to 6% upon heating from room temperature to 150°C in air presumably due to evaporation of residual water. OND manifests the highest water loss of about 6% (Figure 2.8a). The water mass losses for all PPA@OND products are lower, about 3-4%. This implies that PPA grafting renders the OND surface

less hydrophilic, and so the PPA@OND powders are less hygroscopic than OND. The trends are similar for CND and PPA@CND samples, although the starting CND has lower water mass loss (about 4.5%). This indicates that CND is somewhat less hydrophilic than OND.

Upon further heating, OND maintains nearly steady weight up to 480°C followed by a relatively steep rate of mass loss due to oxidative decomposition (Figure 2.8a). In contrast, the mass loss data for all PPA@OND samples [$PPA_{3:5}$@OND, $PPA_{1:9}$@OND, $PPA_{1:9}$@OND(unh), and $PPA_{3:5}$@OND(son)] have nearly steady weights up to about 500°C, then accelerating weight loss in the 500-550°C range, and then steady but rapid weight loss at higher temperatures. Depending on how one defines the degradation temperature, the PPA@OND materials have thermal stability extending approximately 50°C higher than that of OND.

CND (Figure 2.8b) does not exhibit rapid mass loss due to oxidation until approximately 495°C, indicating better thermal stability than OND. The acid treatment of OND used to produce CND may have reduced the amount of exposed sp^2 hybridized carbon that would oxidize at lower temperature. PPA@CND shows enhanced thermal stability relative to CND, as indicated by the ~30°C higher temperature at which the mass loss rate significantly accelerates. For both PPA@OND and PPA@CND, the grafted PPA seems to protect the surface carbons and delays the onset of oxidative decomposition to higher temperatures.

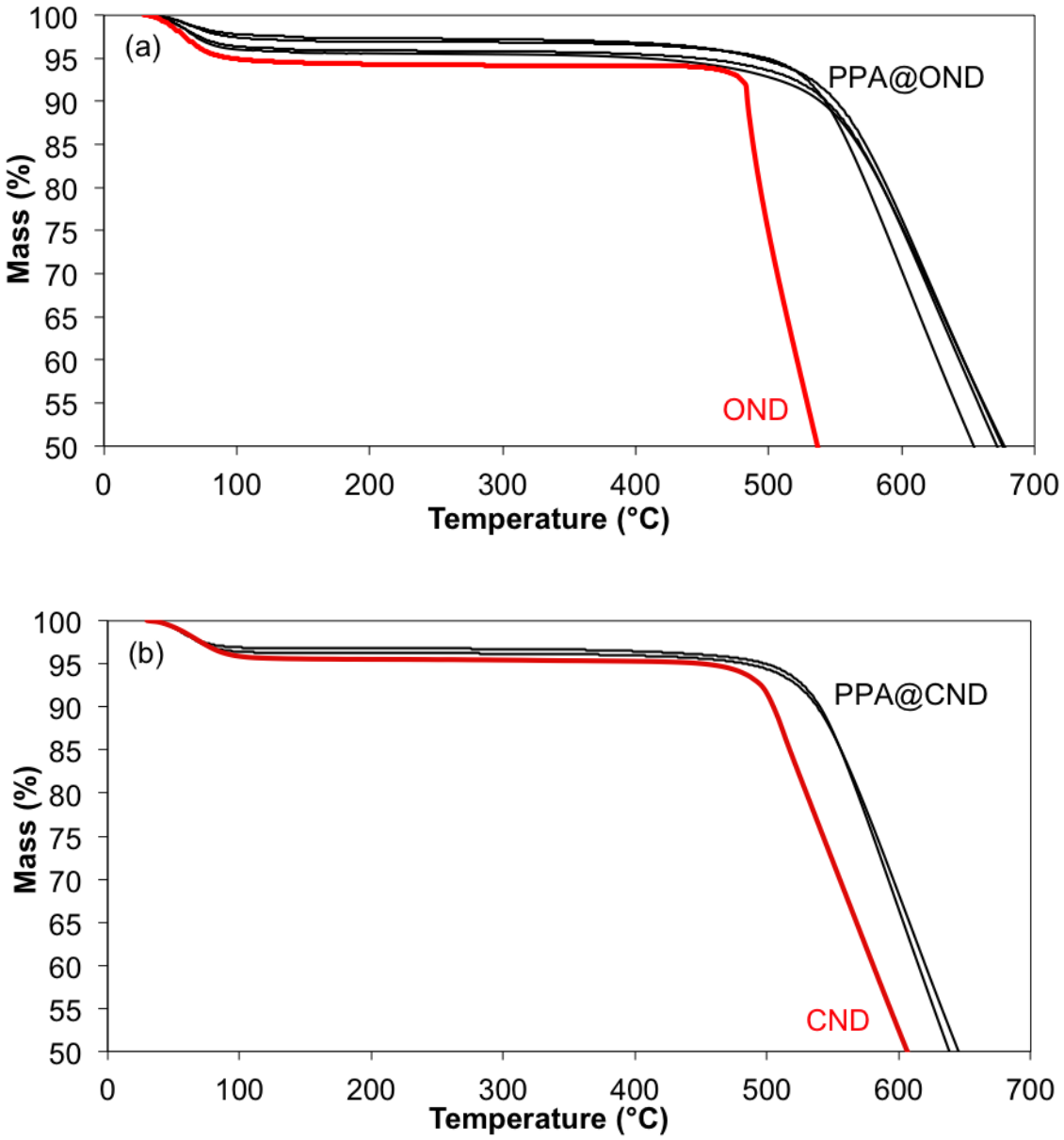

Figure 2.8. TGA characterization of mass percentage as a function of temperature for (a) OND and PPA@OND products [3:5, 1:9, 1:9(unh), 3:5(son)], and (b) CND and PPA@CND products [3:5, 1:9]. All samples were heated in air with a temperature ramp rate of 10°C/min.

2.3.5. PPA@ND Dispersion

Dynamic light scattering (DLS) was used to characterize the effect of PPA grafting on the ability to disperse ND particles in various solvents. Table 2.4 summarizes the key results for dispersion of OND and two PPA@OND products in water, N,N-dimethylformamide (DMF, a polar aprotic organic solvent), and toluene (a nonpolar organic solvent).

Table 2.4. DLS results for OND and PPA@OND particle size (nm) after dispersion in various solvents.

Sample	**Solvent**					
	Water		**DMF**		**toluene**	
	as-dispersed	filtered	as-dispersed	filtered	as-dispersed	filtered
OND	121±3	59±1	~60,100	41±1	~157,000	fail (a)
$PPA_{1:9}$@OND	- -	- -	~210,000	38±1	~43,000	fail (a)
$PPA_{3:5}$@OND(son)	unstable (b)	fail (a)	102±2	57±1	97±1	64±1

(a) Light scattering failed to detect any particles.

(b) Unstable; see Figure 2.8.

Dispersion of OND in water results in colloidal suspensions with an average particle size (121±3 nm) consistent with previous studies [32, 35, 75, 76]. The particle size remained constant over time (Figure 2.9a), indicating the stability of the aqueous OND suspension. DLS characterization after filtration indicates a smaller particle size (59±1 nm), showing that filtration removes larger aggregates while leaving smaller

aggregates in suspension. These results can be rationalized in terms of the hydrophilic character of the OND particle surface. Dispersion of OND in DMF resulted in a suspension dominated by very large agglomerates. After filtration, DLS detected small OND aggregates in the DMF suspension with size (41±1 nm) independent of time (Figure 2.9b). The fraction of OND present in DMF as smaller aggregates was not measured. Nonetheless, the relatively high polarity of DMF permits the dispersion of at least some OND particles as small aggregates. The polar, hydrophilic character of OND particles results in poor dispersability in toluene, a nonpolar organic solvent. The as-prepared toluene suspension of OND contained very large agglomerates that were completely removed by filtration.

PPA grafting presumably renders the OND surface less polar and less hydrophilic due to the presence of the phenyl moiety in PPA. To test this hypothesis, $PPA_{1:9}$@OND was dispersed in DMF and toluene, followed by DLS characterization. For both as-prepared suspensions, DLS indicated the presence of very large $PPA_{1:9}$@OND agglomerates (Table 2.4). After filtration, DLS detected small aggregates in the filtered DMF suspension with stable, time-independent particle size (38±1 nm, Table 2.4 and Figure 2.9b) consistent with that measured for OND in filtered DMF suspension. However, no particles were detected in the filtered toluene suspension of $PPA_{1:9}$@OND. This observation implies that the $PPA_{1:9}$@OND surface has sufficient polarity for dispersion of at least some of the particles as small aggregates in polar aprotic DMF. However, the poor dispersion of $PPA_{1:9}$@OND in toluene was disappointing, considering

that the intent of PPA grafting was to render OND more hydrophobic and thus more compatible with organic solvents and, ultimately, organic polymers.

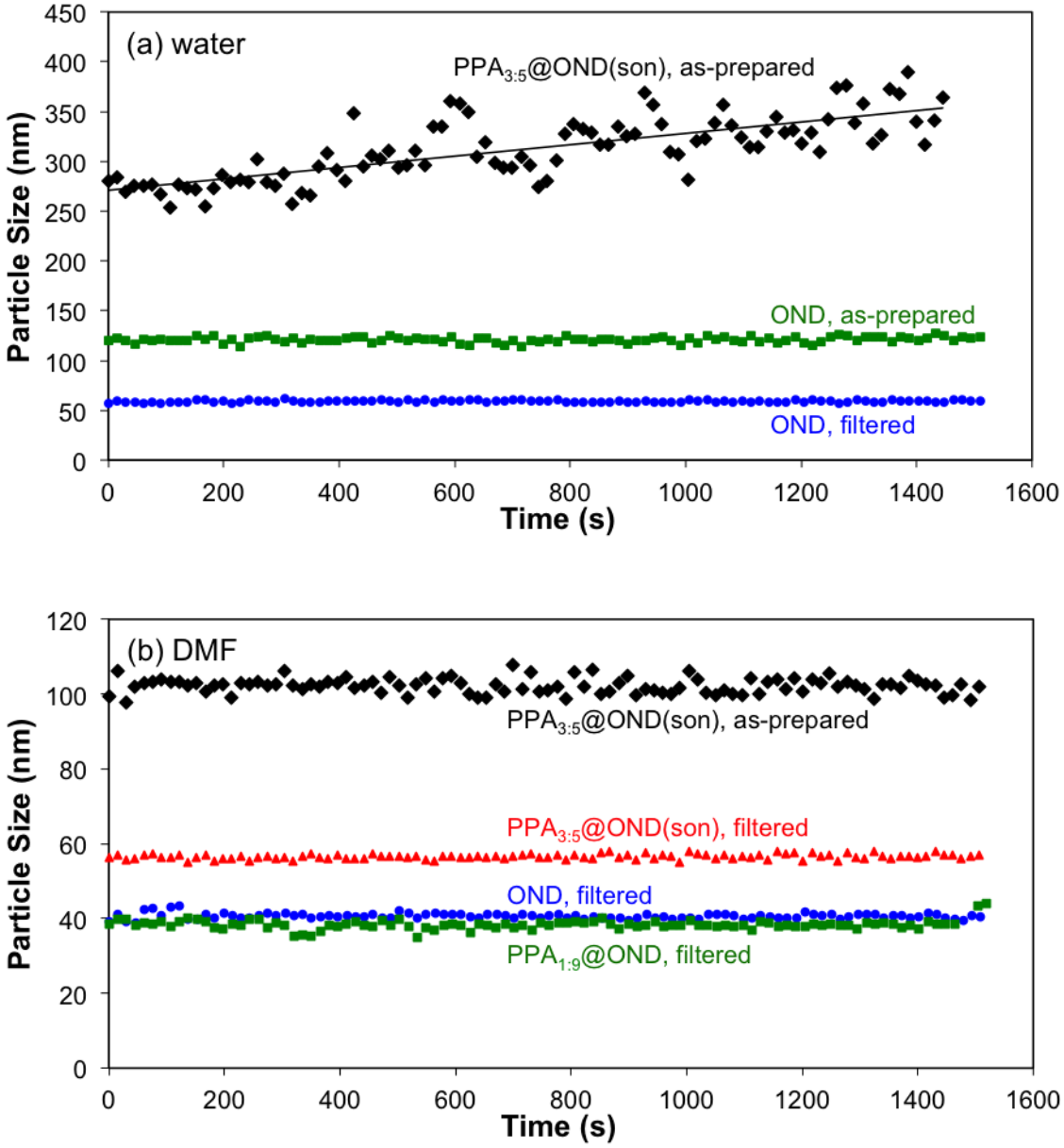

Figure 2.9. DLS measurements of particle size as a function of time for OND and PPA@OND materials dispersed in (a) water and (b) DMF. Sample identity and filtration state (as-prepared or filtered) are indicated on the plots.

In view of this result, it was further hypothesized that the poor dispersability of PPA@OND in organic solvents might be due to incomplete coverage of the OND particle surfaces by grafted PPA. To test this hypothesis, PPA@OND was prepared using a combination of heating and sonication of the PPA+OND suspension during the grafting reaction. The expectation was that sonication would break up OND agglomerates and expose more surface area to PPA grafting.

DLS results indicate that the resulting $PPA_{3:5}$@OND(son) product has quite different dispersion properties than $PPA_{1:9}$@OND prepared with reflux but no sonication. After dispersion in water, $PPA_{3:5}$@OND(son) has an initial particle size of ~275 nm, which subsequently increased to more than 350 nm in 25 min (Figure 2.9a). This shows that PPA@OND can be dispersed in water as aggregates with poor colloidal stability. No $PPA_{3:5}$@OND(son) particles were detected in filtered aqueous suspension. In contrast, the unmodified OND could be dispersed as a stable aqueous suspension. Thus PPA grafting definitely renders the OND surface more hydrophobic and incompatible with water.

DLS measurements (Table 2.4) show that $PPA_{3:5}$@OND(son) forms stable suspensions of small aggregates in both DMF (102±2 nm, Figure 2.9b) and toluene (97±1 nm, Figure A3 of Appendix). Filtration removes some of the larger aggregates, producing filtrates that are stable suspensions of smaller aggregates. The measured sizes of $PPA_{3:5}$@OND(son) aggregates in DMF and toluene suspensions, for both as-prepared and filtered samples, are comparable to those of as-prepared and filtered OND

in water (Table 2.4, Figure 2.9b, Figure A3). Direct comparison of the DLS results for DMF and toluene suspensions of $PPA_{1:9}$@OND and $PPA_{3:5}$@OND(son) demonstrate the value of sonication for ensuring more uniform surface coverage of OND by PPA during the grafting process. Overall, these results demonstrate that PPA grafting with the use of sonication can produce PPA@OND materials that are not only hydrophobic, but also dispersible in both polar aprotic and nonpolar organic solvents.

2.4. Conclusions

This work demonstrates that both oxidized and carboxylated nanodiamond particles can be functionalized through covalent grafting of phenylphosphonate. Data from UV-visible spectrophotometry shows that unreacted PPA was removed from the reaction products through repeated cycles of water washing and centrifugation. ^{31}P MAS NMR and FTIR spectra demonstrate PPA grafts on both OND and CND. Based on XPS data, the grafted amount of PPA on OND appears to be independent of the PPA:ND ratio, application of heat, and use of sonication. However, significantly more PPA grafting occurred on OND compared to CND. NMR and FTIR spectra suggest that PPA grafts onto the ND surface primarily in the bidentate mode through both P-OH and P-O groups. PPA functionalization of the ND surface increases the thermal stability of both OND and CND. Results from DLS indicate that PPA@OND materials prepared without the use of sonication do not disperse well in DMF (a polar aprotic solvent) or toluene (a nonpolar organic solvent). In contrast, use of sonication during the grafting process results in PPA@OND products that can be readily dispersed in these solvents, at least as

relatively small aggregates. This result suggests that sonication during the reaction renders more of the OND surface accessible to PPA grafting.

The DLS results for PPA@OND(son) show that PPA grafting changes the ND surface from hydrophilic to hydrophobic. The PPA@OND products also have enhanced thermal stability. These findings point towards a route for better dispersion of ND particles in organic polymers, via melt or solution blending, to produce ND-based polymer nanocomposites with improved properties.

Acknowledgements

We thank Nirupam Aich and Dr. Navid Saleh for assistance with the dynamic light scattering measurements and Dr. Shuguo Ma for his assistance with the XPS measurements.

CHAPTER 3

NANODIAMOND/PEEK COMPOSITES

3.1. Introduction

In our previous work (Chapter 2, [77]), we demonstrated that both oxidized (OND) and carboxylated nanodiamond (CND) particles can be functionalized through covalent grafting of phenylphosphonate, which increased the thermal stability of both OND and CND significantly. It was also found that the use of sonication during graft reaction made a significant difference in terms of hydrophobicity and produced PPA@OND materials that are not only hydrophobic, but also dispersible in both polar aprotic and nonpolar organic solvents. These findings point towards a route for better dispersion of ND particles in organic polymers, via melt or solution blending, to produce ND-based polymer nanocomposites with improved properties.

The basic objective of the present work is to develop ND/PEEK composites having low dielectric permittivity and low dielectric loss combined with increased thermal conductivity and high thermal stability. To our knowledge, this objective has not been explored in previous work.

3.2. Experimental Section

3.2.1 Materials

The PEEK polymer used in this work was fine powder grade (PEEK 450PF) sourced from Victrex® plc. PEEK 450PF has the following physical characteristics: T_g = 143°C (onset), T_m = 343°C, density = 1.3 g/cm^3, melt viscosity = 350 Pa.s at 400°C, and average particle size (D50) = 50 µm [78]. Oxidized nanodiamond (OND), carboxylic acid modified nanodiamond (CND) and octadecylamine-modified nanodiamond (ODA-ND) were purchased from NanoBlox, Inc. and used as received. BET measurements indicate specific surface areas of 283 and 327 m^2/g for OND and CND, respectively. Surface modification of OND and CND with phenylphosphonate (PPA) followed the procedure described previously (Chapter 2, [77]).

3.2.2 Preparation of ND/PEEK Composites

In this study, varying wt% of ND fillers and PEEK 450PF were melt-blended (compounded) using a DSM Xplore™ 5 cc twin-screw microcompounder with conical, fully intermeshing, and co-rotating screws. The microcompounder features a valve that, when closed, causes recirculation of the polymer and additives, resulting in melt-mixing. Opening the valve results in extrusion of the additive/polymer blend through a die. Both films and cylindrical strands with varying dimensions may be extruded. The extrudate is cooled by forced air convection, and the product may be wound on a take-up roll rotated with controlled speed or torque.

Before compounding, both the PEEK and ND powders were dried in a convection oven at 165°C for 24 h. Appropriate amounts of ND and PEEK were manually mixed in a jar to achieve a rough mix with the desired wt% ND. The temperature profile of the barrel was set at 380/370/400°C from the hopper to the die. About 4 g of the mix was added through the hopper of the microcompounder with the screw speed set at 100 rpm. The residence time of the materials inside the microcompounder was held constant at 3 min to minimize PEEK degradation. Filaments were extruded with about 0.5 mm diameter without forced convection air cooling. The product fibers were used directly in some tests or pelletized to make compression-molded specimens. This procedure was also followed to prepare specimens of pure PEEK with the same process history. A thin film sample of amorphous/semi-crystalline PEEK (denoted below as APEEK) was also prepared using the same compounding conditions. Instead of extruding it through the strand die, it was extruded through a 38 mm wide slit die followed by rapid quenching with forced air convection.

In preliminary research, we performed a melt blending study using various nanodiamond products (OND, CND and ODA-ND) without PPA modification, blended with PEEK in as-received form from the supplier (Nanoblox, Inc.). Table 3.1 shows the formulations of the various composites produced in this preliminary study. The “NB” subscript indicates that the ND materials were used as received from Nanoblox, without any additional surface modification. None of the nanocomposite strands made in this preliminary study were annealed before tensile testing.

Table 3.2 shows the formulations of various ND/PEEK composites prepared using PPA-modified OND or CND. In this primary study, all of the OND and CND materials were functionalized with PPA as described in Chapter 2. The subscript "son" for some samples indicates that the OND suspension was sonicated during the PPA grafting process. ND/PEEK melt blending followed the same procedure described previously.

Table 3.1. Composition of ND_{NB}/PEEK nanocomposites Investigated in the preliminary compounding study.

Material (a)	ND Type (a)	ND (wt%)
PEEK	--	0%
1% OND_{NB}/PEEK	OND_{NB}	1%
2% OND_{NB}/PEEK	OND_{NB}	2%
4% OND_{NB}/PEEK	OND_{NB}	4%
6% OND_{NB}/PEEK	OND_{NB}	6%
2% CND_{NB}/PEEK	CND_{NB}	2%
4% CND_{NB}/PEEK	CND_{NB}	4%
0.5% ODA-ND_{NB}/PEEK	ODA-ND_{NB}	0.5%
2% ODA-ND_{NB}/PEEK	ODA-ND_{NB}	2%
4% ODA-ND_{NB}/PEEK	ODA-ND_{NB}	4%

(a) The subscript "NB" indicates that the ND materials were used as received from Nanoblox, without any additional surface modification.

Table 3.2. Composition of PPA@ND/PEEK nanocomposites Investigated in the primary study. All of the OND and CND materials listed were surface-modified with PPA as described in Chapter 2.

Material (a)	ND Type (b)	ND (wt%)
PEEK	--	0%
APEEK	--	0%
3% OND/PEEK	$PPA_{1:9}$OND	3%
3% CND/PEEK	$PPA_{1:9}$CND	3%
1% son-OND/PEEK	$PPA_{3:5}$OND(son)	1%
3% son-OND/PEEK	$PPA_{3:5}$OND(son)	3%
5% son-OND/PEEK	$PPA_{3:5}$OND(son)	5%

(a) The term "son" indicates that the OND suspensions were sonicated during surface modification with PPA.
(b) ND type: notation as defined in Chapter 2.

3.2.3 Test Specimen Preparation

To prepare compression molded plaques, compounded, pelletized strands were placed in a 15.2 cm x 10.2 cm (6”x4”) stainless steel mold/bracket covered by two brass plates at the bottom and at the top. The assembly was then placed inside the compression molding (hot press) machine heated to 370°C. Compressive force (10 MPa) was applied and held for 15 minutes, followed by cooling to 50°C. The resulting plaques had thicknesses of 0.5 to 0.8 mm. Both plaques and extruded fibers were annealed at 200°C for 3 hours. Annealed plaques were used for thermal conductivity tests, and annealed fibers were used for tensile, DMA and TGA tests.

Some of the plaques were further compressed to produce thin film samples (25-75µm) by applying 10MPa pressure for 30 minutes at 370°C, followed by cooling to 50°C. The main use of thin film samples was for dielectric testing. For this purpose, film samples were gold sputter-coated with gold under argon atmosphere through a shadow mask to deposit circular gold electrodes (area 0.283 cm^2) on both surfaces of the film. Some thin film samples were also used for DSC characterization.

3.2.4 Characterization Techniques

3.2.4.1 Surface Topography

nSpec® 3D (Nanotronics Imaging, Inc.) is an automated, rapid optical microscope that provides three-dimensional surface topographies and quantitative surface roughness measurements. In this work, three dimensional topography images were

generated using an nSpec® 3D system using a 20x objective. Bright-field optical images and 3-D topographic scans were measured on the surfaces of sample cross-sections prepared using a manual cutter with a fresh razor blade for each cut. Instrument software provides quantitative analysis of the 3-D topographic scans, including surface roughness, number of asperities in the image, and average asperity volume. All optical images, 3-D tomographic scans, and image analysis were performed by collaborators at Nanotronics Imaging.

3.2.4.2 X-Ray Scattering Measurements

X-ray scattering experiments were conducted using a SAXSLab Ganesha at the South Carolina SAXS Collaborative. A Xenocs GeniX3D microfocus source was used with a Cu target to generate a monochromic beam with a 0.154 nm wavelength. The instrument was calibrated using a silver behenate reference with the first order scattering vector $q^* = 1.076\ nm^{-1}$, where $q = (4\pi/\lambda)\sin\theta$ with a total scattering angle of 2θ. A Pilatus 300 K detector (Dectris) was used to collect the two-dimensional (2D) scattering patterns. Radial integration of 2D WAXS patterns reduced the data to 1D profiles using SAXS GUI software.

Samples were mounted on an ambient sample stage using kapton tape to secure them. Once mounted, the ambient stage was loaded and fixed in position with screws before the chamber was evacuated. Extra small angle measurements (ESAXS) were acquired using 30 minute scans. Small angle measurements (SAXS) were acquired with 20 minute scans. Medium angle measurements (MAXS) were acquired with 15 minute

scans and wide angle measurements (WAXS) were acquired over 5 minutes. All X-ray scattering measurements were performed by Zachary Marsh in the USC Department of Chemistry & Biochemistry.

3.2.4.3 Tensile Testing

Stress-strain curves were measured using a SYNERGIE 200 tensile tester (MTS Systems, Inc.) without strain gauge-type extensometer at room temperature. A 100 N load cell was used with a gauge length of 10.16 cm (4 in) and strain rate of 5.08 cm/min (2 in/min). At least five replicate tensile tests were performed for each sample to establish mean and standard deviation of measured quantities.

3.2.4.4 Dynamic Mechanical Analysis (DMA)

The dynamic mechanical properties of all samples were characterized using a RSA-III dynamic mechanical analyzer (TA Instruments). Experiments were performed in tensile mode at fixed frequency of 1.0 Hz and 0.2% strain amplitude. The complex modulus spectra were recorded as temperature sweeps from room temperature to 260^{o}C.

3.2.4.5 Thermogravimetric Analysis (TGA)

Thermogravimetric analyses (TGA) were performed using a Mettler Toledo TGA/SDTA851. TGA samples were heated either in air or N_2 from room temperature to 900°C using a heating rate of 10°C/min. Isothermal TGA tests were also performed, either in air or N_2, by heating the sample from room temperature to 365^{o}C and then

holding at this temperature for 60 min. The TGA tests were performed with the help of Zeus analytical lab.

3.2.4.6 Differential Scanning Calorimetry (DSC)

A differential scanning calorimeter (model Q2000 V24.11 build 124, TA Instruments) was used to perform dynamic DSC experiments. Samples of about 10 mg were sealed under N_2 atmosphere in aluminum pans and then heated from 100°C to 400°C at 3°C/min for the first heating cycle. The sample was then cooled to 100°C at 3°C/min (first cooling cycle), and then heated again to 400°C at 3°C/min (second heating cycle). The DSC instrument software automatically provides melting and crystallization temperatures and enthalpy values from the peaks in the heating and cooling curves. Degree of crystallinity (X_c) values are obtained by integrating the area under the melting peak during heating cycle and normalized to the actual weight fraction of polymer, and then the area was divided by the ΔH_f (Enthalpy of fusion) of 100% crystalline PEEK (130 J/g) [1, 5]. The crystallinity of the PEEK constituent in the composite was determined by Eq. (1) [1].

$$X_c = \frac{\Delta H_f}{\Delta H^0{}_f \, W_{polymer}} \times 100$$

where ΔH_f^0 is theoretical value of ΔH_f for 100% crystalline PEEK, and $W_{polymer}$ is the weight fraction of the polymer matrix. The DSC tests were performed with the help of Zeus analytical lab.

3.2.4.7 Thermal Conductivity Measurements

A linear unidirectional heat transfer apparatus (Armfield HT11) was built to conform to ASTM 1225-04 standard and used to characterize the thermal conductivity of compression-molded samples. Figure 3.1 shows a schematic diagram of the apparatus. An electrical heat source (heater) delivers heat to a 25.4 mm diameter polycarbonate (PC) rod, which then transfers the heat to the specimen supported by a second 25.4 mm diameter PC rod. The lower PC rod contacts a copper rod immersed in constantly-running water at the other end, which serves as the heat sink. The apparatus incorporates multiple thermocouples to monitor the temperature profile from the heat source, through the specimen, and into the heat sink. The effective thermal conductivity (K_e) of the sample is calculated from a simple one-dimensional conduction model assuming all materials obey Fourier's law [79]:

$$K_e = K_{PC}\left[\frac{(\Delta X_{PC})*((T_3 - T_4)+(T_5 - T_6))}{2*(\Delta X_{Sample})*(T_H - T_C)}\right]$$

In this equation, ΔX_{sample} is the sample thickness, and the various temperatures are measured at locations indicated in Figure 3.1. Further details of the equipment and the procedure can be found elsewhere [79]. All thermal conductivity measurements were performed by Addis Tessema in the USC Department of Mechanical Engineering.

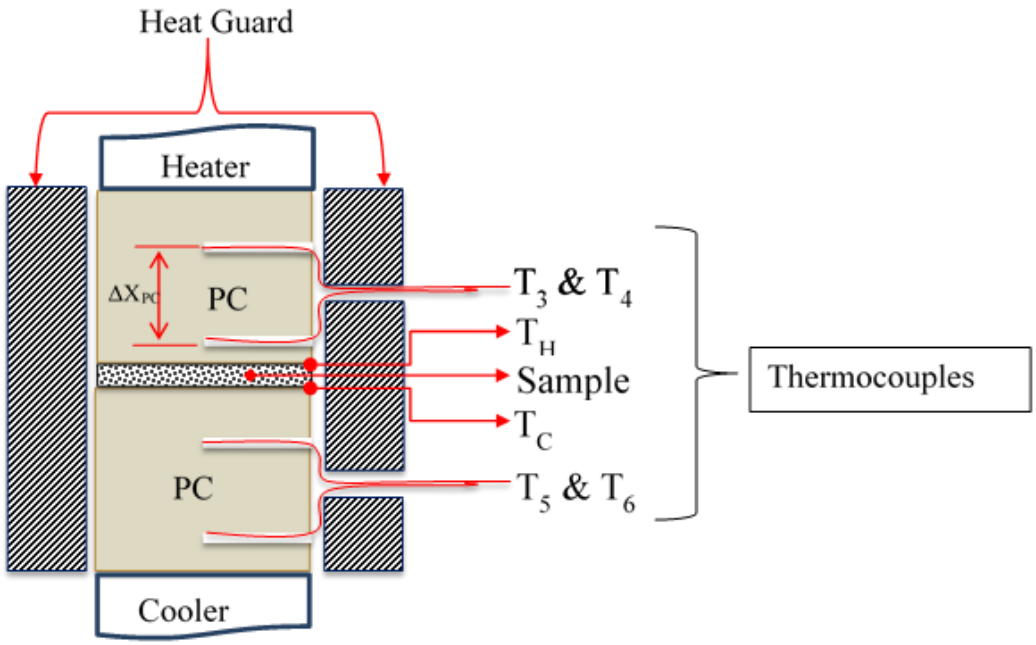

Figure 3.1. Schematic diagram of the apparatus used to measure the thermal conductivity of PEEK and ND/PEEK composite samples.

3.2.4.8 Dielectric Measurements

Dielectric measurements characterize the dielectric polarization of a material in response to an applied time-varying electric field [80]. In dielectric impedance spectroscopy, the applied electric field has low amplitude, and so the magnitude of dielectric complex impedance varies linearly with the applied field strength. The complex impedance has real and imaginary parts [80]. The real part ε‘, known as the dielectric permittivity, quantifies reversible electrical energy storage due to charge polarization. Dividing ε‘ by the vacuum permittivity defines the relative permittivity, also known as the dielectric constant (ε_r). Polarization usually involves the formation of a non-uniform electron cloud distribution or the distortion of ionic charge layers. The resulting dipolar electric fields store electrical energy that is released when the applied

field is removed. An ideal dielectric insulator releases 100% of the stored energy. However, some of the dipolar charge may migrate as "leakage" current, resulting in dissipation of some electrical energy as heat. The dielectric loss (ε") quantifies the electric energy lost during cyclic electrical excitation. The ratio ε"/ε' is known as the loss tangent (tan δ).

The complex impedance of PEEK and PEEK/ND nanocomposite film samples were measured using a LCR meter (Agilent model E4980A). Measurements were carried out at a fixed applied voltage (20 mV) and varying frequency (typically from 10^2 to 2×10^6 Hz). Impedance spectra were collected for 3−5 specimens of each sample to ensure reproducibility; average values are reported. The real and complex parts of the impedance, expressed as impedance magnitude and phase angle, were analyzed using a parallel RC circuit model describing a "leaky" capacitor, yielding values of relative permittivity (ε_r) and loss tangent (tan δ) as functions of frequency.

Polarization measurements at higher applied electric fields employed a polarization tester (Precision Multiferroic, Radiant, Inc.). These measurements characterize the non-linear dielectric response that results from stronger applied fields. Polarization data (dielectric displacement D versus applied electric field E) were obtained for applied voltages up to 2000 V with a cycle frequency of 10 Hz. The maximum applied field strength depended on the sample film thickness and breakdown strength.

3.3 Results and Discussions: Preliminary Study of ND_{NB}/PEEK Composites

Preliminary research investigated the hypothesis that high-performance ND/PEEK composites could be prepared by direct melt blending of as-received ND powders with PEEK 450PF. Table 3.1 shows the formulations of ND_{NB}/PEEK composites prepared for this study; the "NB" subscript denotes that the ND materials were used as received from Nanoblox, without any additional surface modification.

The appearance and texture of the ND_{NB}/PEEK composites suggest that melt blending did not completely disperse ND_{NB} in PEEK. For the OND_{NB}/PEEK composites, with increasing OND_{NB} content in the PEEK matrix, the surface of the extruded composite strands became progressively rougher (by touch), presumably due to the presence of large OND_{NB} agglomerates. At the highest OND_{NB} content, it became more difficult to obtain uniform diameter strands from the melt extrusion die, another indication of poor filler dispersion. Similar observations were apparent for CND_{NB}/PEEK composites: at 2% and 4% CND_{NB} loading, the strands' surface roughness seemed similar to that of OND_{NB}/PEEK. This suggests that neither as-received CND_{NB} or OND_{NB} disperses very well in PEEK.

ODA-ND_{NB} was also melt-blended with PEEK 450PF under similar conditions to produce composite fibers. During blending and extrusion of 0.5 wt% ODA-ND_{NB} with PEEK, a strong odor was apparent; the odor was even more intense at higher loadings of ODA-ND_{NB}. This indicated that the ODA surface modifier is not thermally stable at the temperature required for melt-blending with PEEK (up to 400°C). At a loading of 4 wt%

ODA-ND_{NB}, the off-gassing due to ODA decomposition was so severe that a specimen satisfactory quality could not be produced for tensile testing. Strands of ODA-ND_{NB}/PEEK manifested surface roughness similar to that of OND_{NB}/PEEK and CND_{NB}/PEEK, which we attribute to ODA-ND_{NB} agglomerates. These observations suggest that ODA-ND_{NB} has no better dispersion in PEEK than of OND_{NB} or CND_{NB}.

Figures 3.2-3.4 and Table 3.3 present tensile test results for ND_{NB}/PEEK composites. Replicate stress-strain curves for each sample may be found in Appendix B. For all of the ND_{NB}/PEEK composites, the Young's modulus values (Figure 3.2) do not differ significantly from that of PEEK, nor do they show a significant change with increasing ND_{NB} loading. One exception may be the OND_{NB}/PEEK composites, for which the Young's modulus shows a small but significant decrease at OND_{NB} loadings of 4 wt% and above. With respect to tensile strength (Figure 3.3) and elongation at break (Figure 3.4), these properties decrease monotonically and significantly with increasing ND_{NB} loading for all types of ND_{NB}. These results demonstrate that the melt blending of as-received ND_{NB} with PEEK results in composites with mechanical properties poorer than those of pure PEEK. Adding less than 4 wt% ND_{NB} to PEEK has minimal effect on Young's moduli values, but higher loadings may have a negative impact. For all kinds of as-received ND_{NB}, melt blending with PEEK has a negative impact on tensile strength and elongation at break.

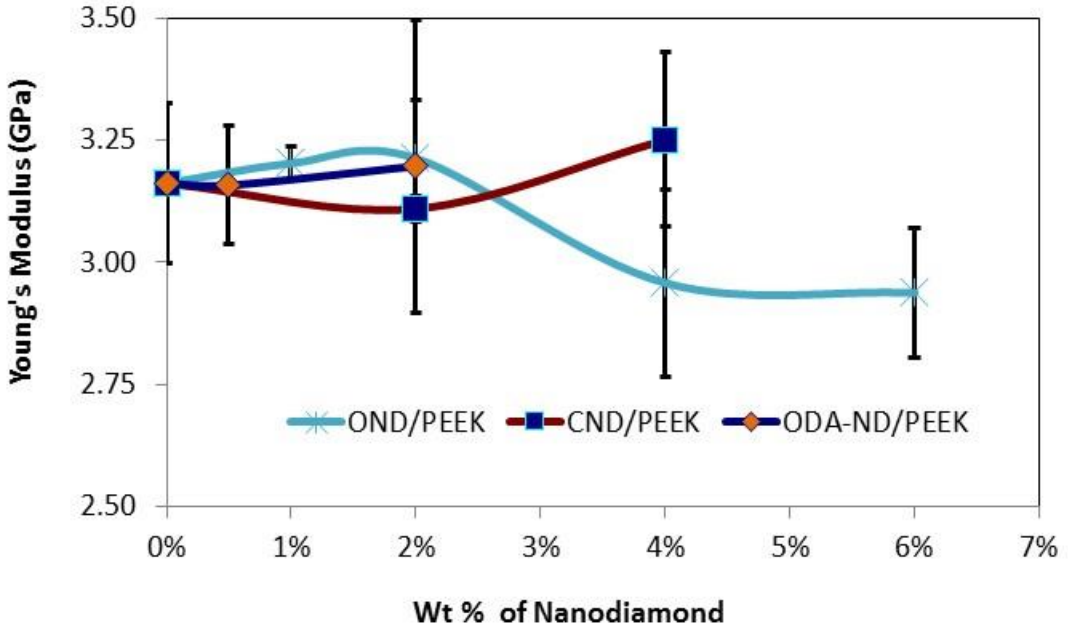

Figure 3.2. Young's modulus as a function of ND loading for various ND_{NB}/PEEK composites.

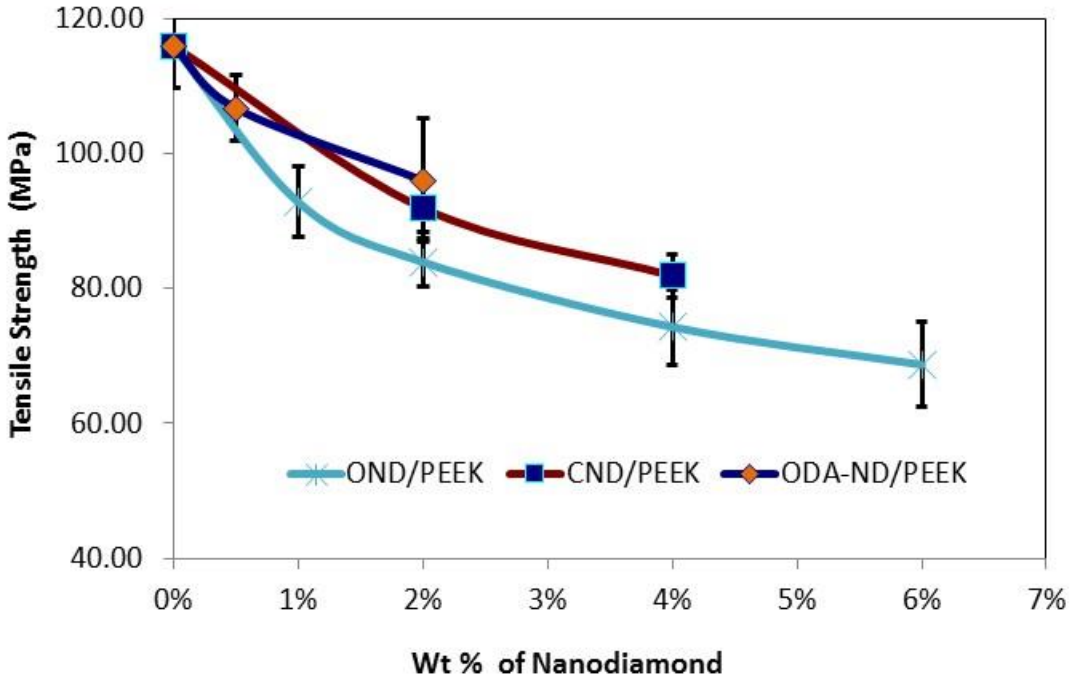

Figure 3.3. Tensile strength as a function of ND loading for various ND_{NB}/PEEK composites.

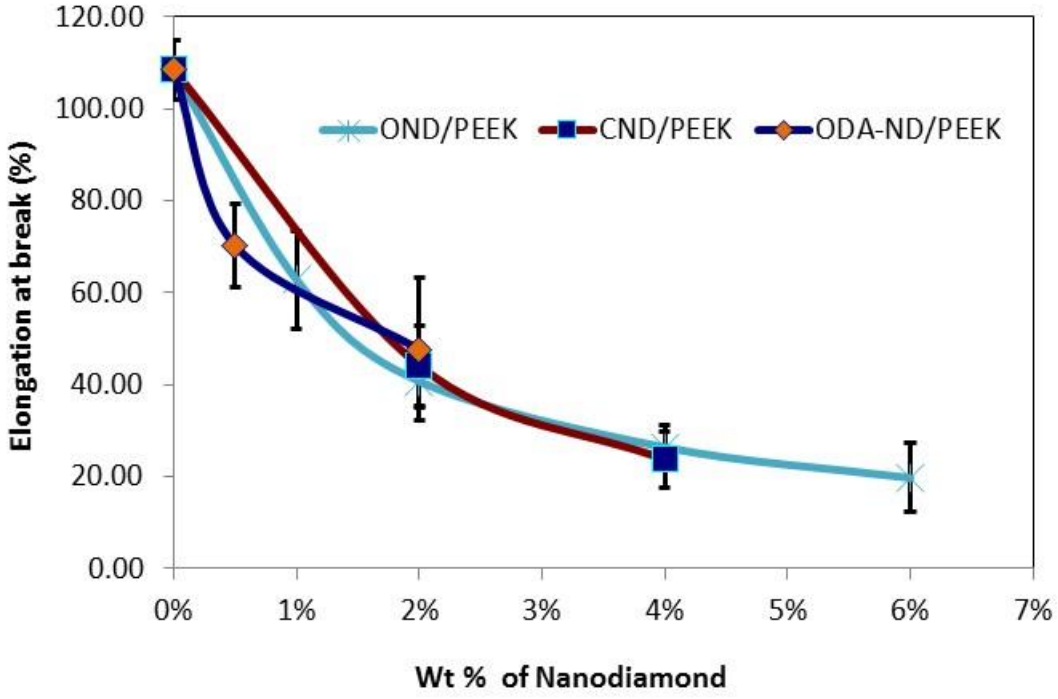

Figure 3.4. Elongation at break (%) as a function of ND loading for various ND_{NB}/PEEK composites.

Table 3.3. Tensile test results for various ND_{NB}/PEEK composites.

Composites	Young's Modulus (GPa)	Tensile Strength (Mpa)	Elongation at break (%)
PEEK	3.16 ± 0.165	115.9 ± 6.3	108.44 ± 6.34
OND_{NB}/PEEK (1%)	3.203 ± 0.034	92.8 ± 5.2	62.81 ± 10.54
OND_{NB}/PEEK (2%)	3.213 ± 0.12	83.9 ± 3.6	40.74 ± 5.6
OND_{NB}/PEEK (4%)	2.958 ± 0.191	74.3 ± 5.6	26.41 ± 4.65
OND_{NB}/PEEK (6%)	2.938 ± 0.132	68.7 ± 6.3	19.76 ± 7.56
CND_{NB}/PEEK(2%)	3.11± 0.027	91.9 ± 3.5	44.13 ± 8.62
CND_{NB}/PEEK (4%)	3.251 ± 0.179	81.9 ± 3.2	23.72 ± 6.13
ODA-ND_{NB}/PEEK (0.5%)	3.158 ± 0.122	106.7 ± 4.9	70.24 ± 9.15
ODA-ND_{NB}/PEEK (2%)	3.197 ± 0.3	96 ± 9.1	47.72 ± 15.54

Note: five tensile tests were performed for each sample.

In summary, as-received ND_{NB}, provides no enhancement of mechanical strength of ND_{NB}/PEEK composites while making them more brittle. Based on our visual and tactile assessment of these composites, we believe that poor ND_{NB} dispersion may explain the unchanged (tensile modulus) or degraded mechanical properties of ND_{NB}/PEEK composites relative to PEEK. The incomplete dispersion of ND_{NB} in PEEK may be due to the incompatibility between the relatively hydrophilic ND_{NB} surfaces and the more hydrophobic PEEK. Use of as-received ND_{NB} as an additive to PEEK may lead to other kinds of improved properties, but as-received ND_{NB} should not be expected to yield enhanced mechanical properties in ND_{NB}/PEEK composites.

3.4 Results and Discussions: PPA-Modified ND/PEEK Composites

The disappointing physical and mechanical properties of ND_{NB}/PEEK composites (section 3.3), attributed to poor dispersion of ND_{NB} in PEEK, motivated our subsequent investigation of PPA-modified ND. The hypothesis is that grafting the aromatic PPA onto ND will render the particles more hydrophobic and thus more compatible with hydrophobic, aromatic PEEK. The first step was to accomplish grafting of PPA onto ND and demonstrate that this rendered the ND particles hydrophobic. These goals were achieved, as described in Chapter 2.

This section describes the physical, mechanical, thermal, and dielectric properties of ND/PEEK composites prepared by melt blending PPA-modified ND with PEEK. Table 3.2 shows the formulations of various ND/PEEK composites prepared using PPA-modified OND or CND. In this section, all of the OND and CND materials were

functionalized with PPA as described in Chapter 2. The term "son" for some OND samples indicates that the OND suspension was sonicated during the PPA grafting process.

3.4.1 Physical and Structural Characterization

3.4.1.1 Physical Appearance

The appearance and texture of PPA-modified ND/PEEK composites suggest that melt blending achieved better ND dispersion than found previously for ND_{NB} in PEEK (section 3.3). For son-OND/PEEK composites containing up to 3 wt% son-OND, extruded strands manifested significantly less surface roughness, as determined by touch as well as visual inspection. Considering other PEEK composites (3% OND, 3% CND, 5% son-OND), good quality strands were extruded with marginally better texture and appearance than ND_{NB}/PEEK composites. None of the PPA-modified ND/PEEK composites showed any indication of outgassing or thermal instability at processing temperatures up to 400°C.

3.4.1.2. Surface Tomography

Figure 3.5 shows optical images of the cross-sectional surfaces of PEEK and various ND/PEEK composites. The textures in the images for the ND/PEEK samples clearly differ from that of pure PEEK. Among the ND/PEEK composites, the 3 wt% CND/PEEK sample (Figure 3.5c) appears to have a coarser surface texture than the other samples. Three-dimensional topographic reconstructions (Figure 3.6) derived from nSPEC surface tomography provide better visual indications of surface texture. Qualitatively, pure PEEK (Figure 3.6a) appears to have a smooth surface texture, as one might expect for a polymer not containing particulate filler. The 3% CND/PEEK sample (Figure 3.6c) has more surface

texture than 3% OND/PEEK (Figure 3.6b), suggesting better dispersion of OND in PEEK compared to CND. Among the composites containing son-OND, the coarseness of the composite surface texture appears to increase with son-OND loading (Figure 3.6d-f). This is consistent with the expectation that the size and number of particle aggregates would increase with son-OND loading.

Quantitative analysis of the topographic reconstruction images provides additional insight. Figure 3.7 shows the surface roughness of each sample cross-sectional surface, representing the average deviation of points on the surface from the average elevation. The surface roughness values for most of the ND/PEEK composites are greater than that of pure PEEK. However, among the composite samples, no definitive trends are apparent. Closer examination of the topographic reconstruction images (Figure 3.6) suggests that surface non-planarity (μm to mm scale) makes a dominant contribution to the average surface roughness measurements. The 1.39 μm surface roughness value for pure PEEK indicates the magnitude of this contribution. both local surface texture and. Since the surface texture originating from the ND filler aggregates appears to have a smaller scale (μm to sub-μm), we do not believe surface roughness provides an accurate measure of ND particle dispersion in ND/PEEK composites.

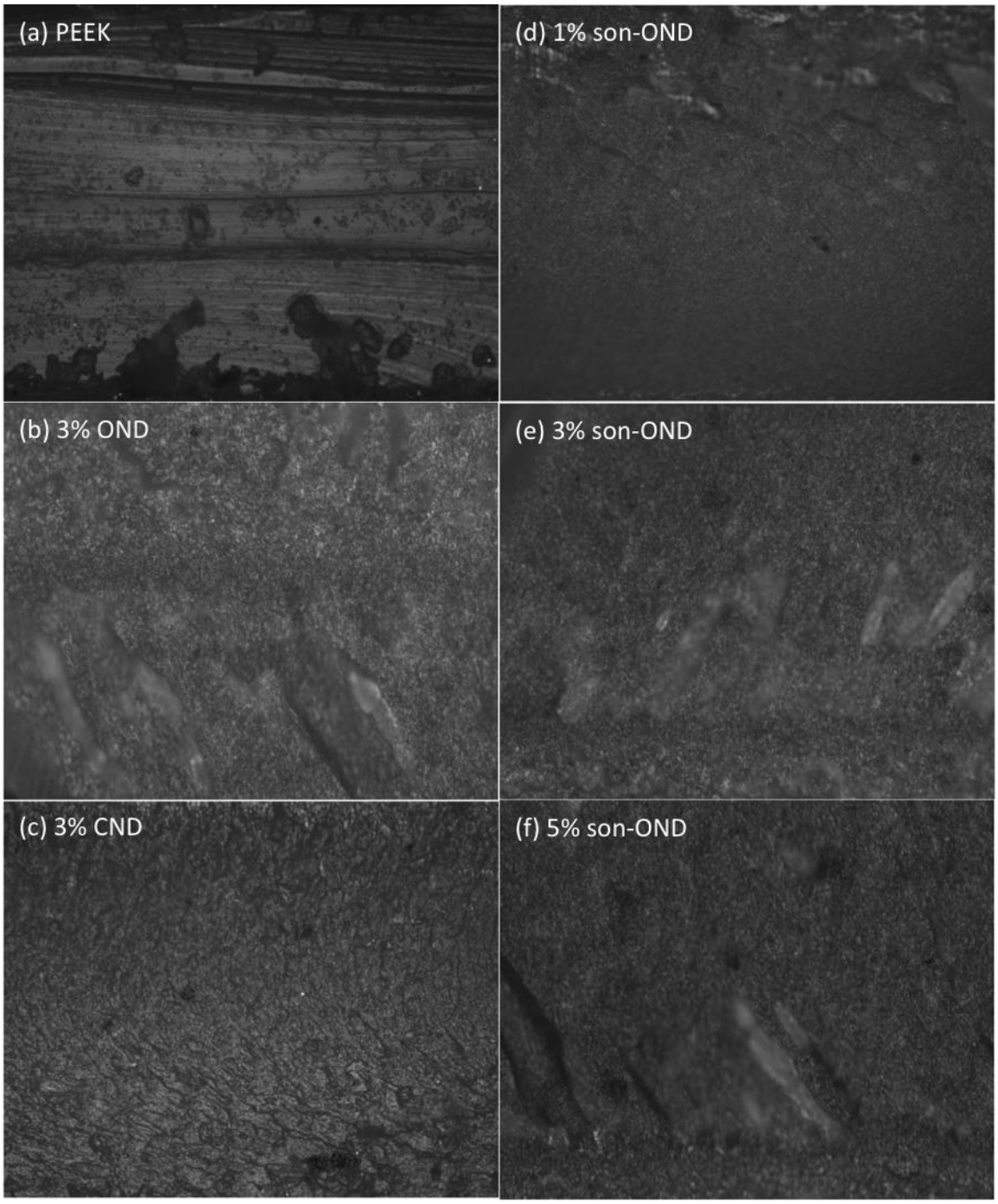

Figure 3.5. Bright field optical images of cross-sectional surfaces of (a) PEEK and (b-f) various ND/PEEK composites as indicated in the image labels. The dimensions of each image are approximately 0.625 mm by 0.500 mm.

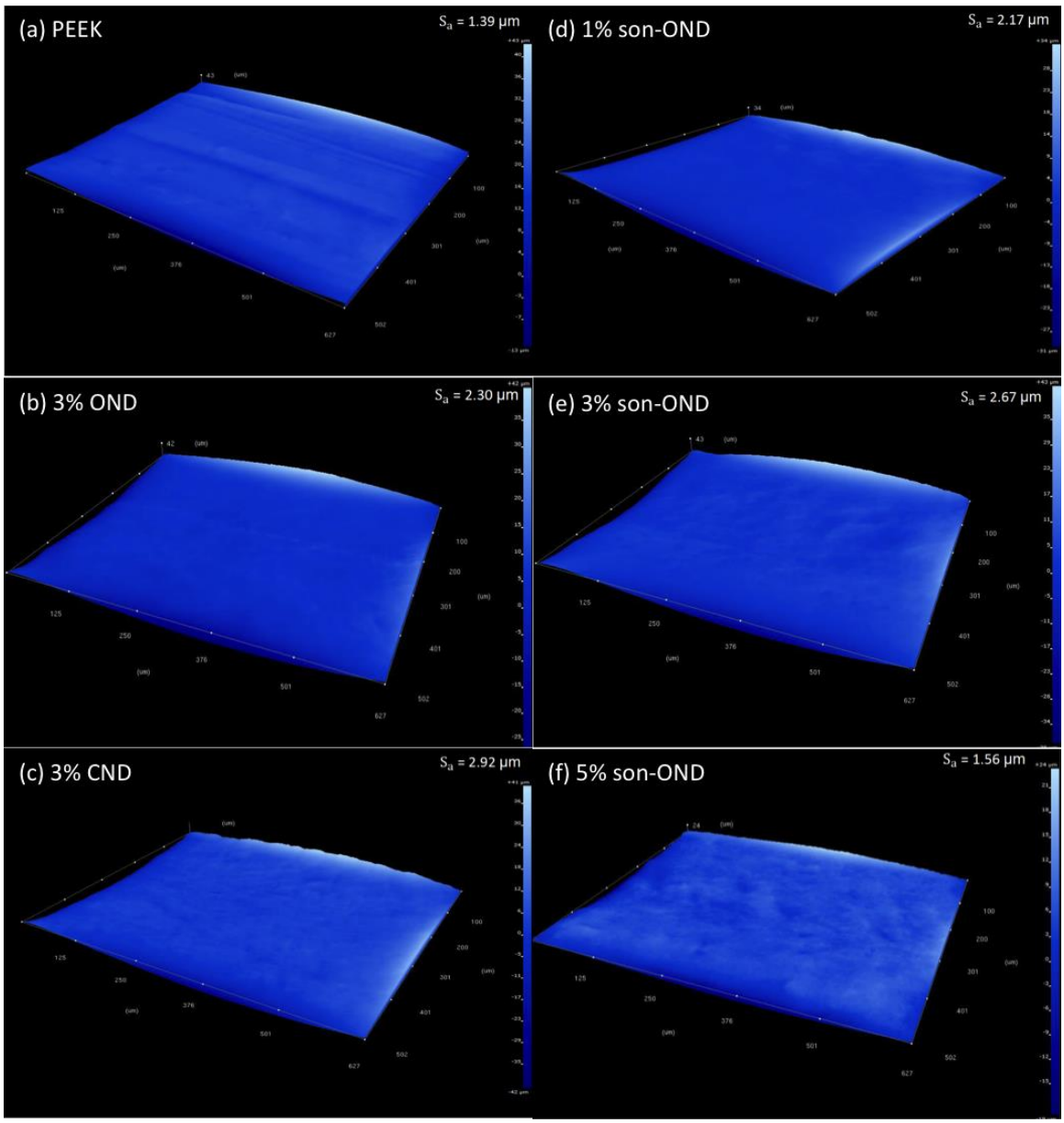

Figure 3.6. Three-dimensional topographic reconstructions of cross-sectional surfaces of (a) PEEK and (b-f) various ND/PEEK composites as indicated in the image labels. The dimensions of each image are approximately 0.625 mm by 0.500 mm. The vertical scales (not legible in this view) vary among the images.

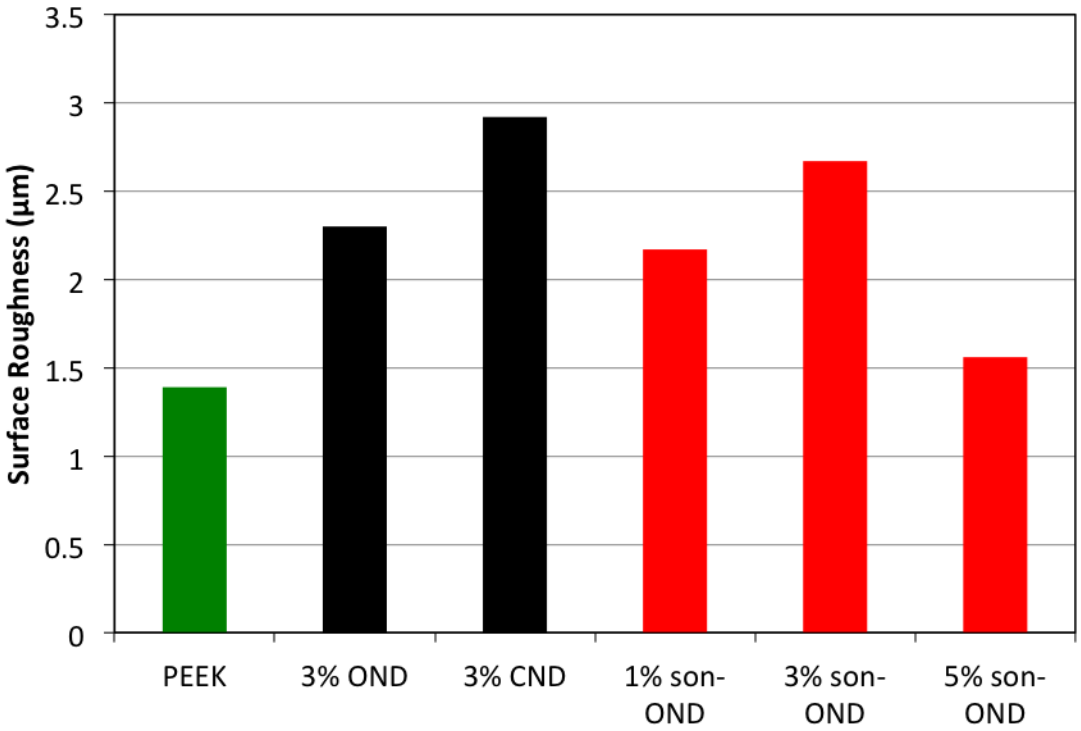

Figure 3.7. Surface roughness values for cross-sectional surfaces of PEEK and various ND/PEEK composites.

Quantitative analysis of the topographic reconstruction images also provides measures of the asperity density (number per unit surface area) and their average volume (Figure 3.8). Each asperity represents a "feature" that may protrude above or below the average plane of the surface. The average asperity volume provides a size scale for the asperities. The surface of pure PEEK has about 900 asperities per mm^2 (Figure 3.8a) with an average asperity volume of about 48 μm^3 (Figure 3.8b). The product of asperity area density and average volume gives a characteristic length that we call "average asperity height". For PEEK, this value is about 43 nm (Figure 3.8c).

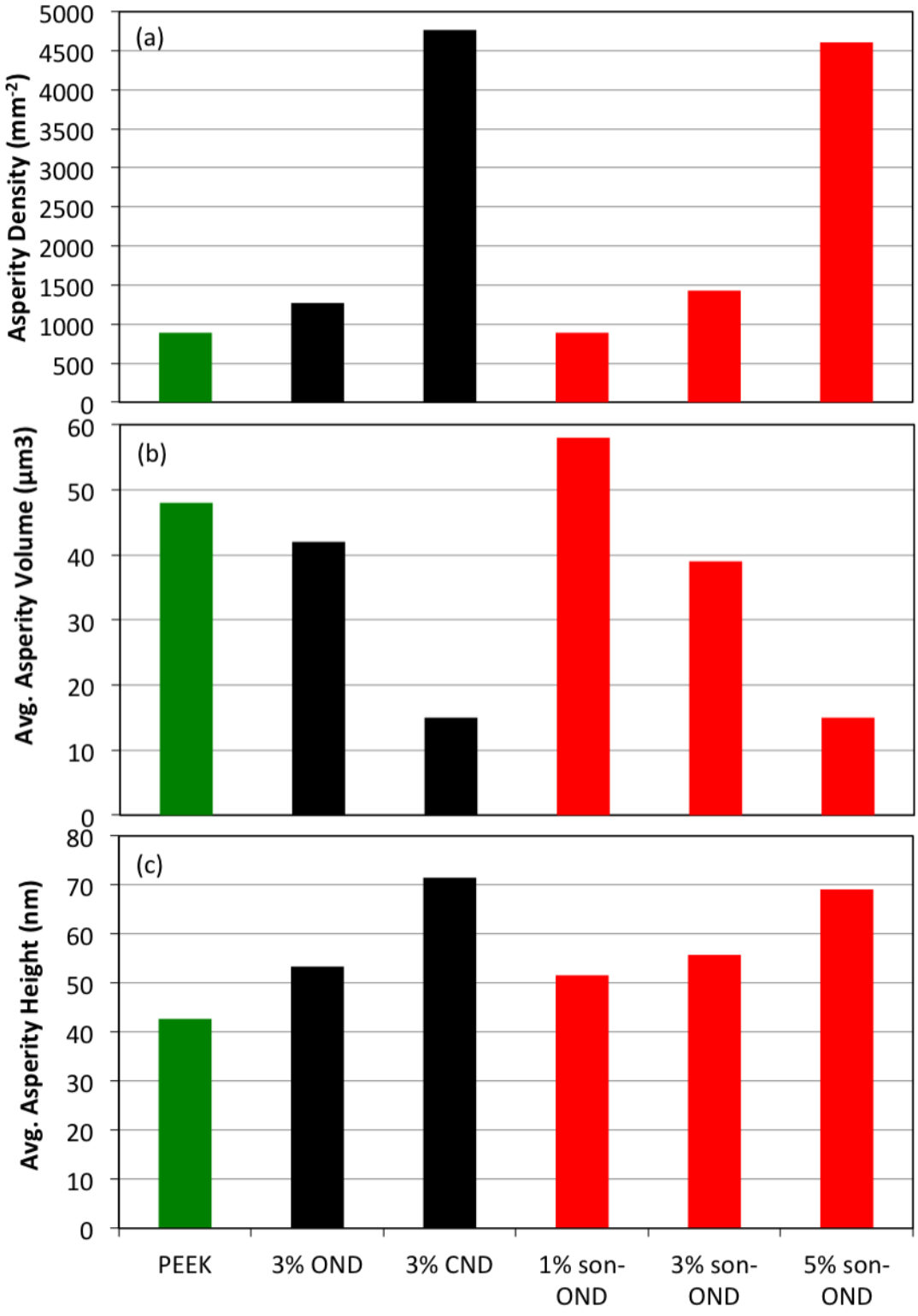

Figure 3.8. Values of asperity density (a), average asperity volume (b), and average asperity height (c) for cross-sectional surfaces of PEEK and various ND/PEEK composites.

The 3% OND/PEEK composite surface has an asperity density of about 1,270 mm^2 (Figure 3.8a) and average asperity volume of 42 μm^3 (Figure 3.8b). The similarity of these values to those of pure PEEK implies that the asperities in pure PEEK and 3% OND/PEEK have a similar nature, and that the OND particles are relatively well-dispersed in the PEEK. In contrast, 3% CND/PEEK has almost 4,800 asperities per mm^2 (Figure 3.8a) with an average asperity volume of 15 μm^3 (Figure 3.8b). The average asperity height for 3% CND/PEEK (71 nm) is much greater than that for PEEK or 3% OND/PEEK. The greater asperity density, smaller average volume, and larger average height can be explained by the presence of large CND aggregates. In other words, we believe that CND is not dispersed well in PEEK compared to OND/PEEK. The optical images in Figure 3.5b-c provide qualitative visual support for this conclusion.

Figure 3.8 shows that the asperities on the surfaces of 3% OND/PEEK and 3% son-OND/PEEK have similar area density, average volume, and average height. Compared to the values for PEEK, these results suggest some aggregates of OND may contribute to surface texture in these composites. The dispersion of OND in PEEK appears to be relatively good in both of these composites. However, we conclude that sonication of OND during the PPA grafting process does not improve the dispersion of OND in PEEK during melt blending.

Finally, the asperity surface density increases sharply with increasing son-OND loading (Figure 3.8a), and the average asperity volume decreases sharply (Figure 3.8b). Their product, the average asperity height, also manifests a significant increase with son-

OND loading (Figure 3.8c). These observations are consistent with an increase in son-OND particle aggregation with increasing loading, which results in significant coarsening of the surface texture of son-OND/PEEK composites at the highest filler loading.

3.4.1.3 PEEK Crystallinity Via X-Ray Scattering

In this section, we consider the effect of added ND on the crystallinity of the PEEK matrix. Figure 3.9 compares the WAXS profiles of pure PEEK and ND/PEEK composites, and Table 3.3 gives the unit cell parameters extracted from the WAXS patterns. The WAXS pattern for pure PEEK and the corresponding unit cell dimensions are consistent with previous studies [81]. The WAXS patterns for all of the ND/PEEK composites (Figure 3.9) show all of the same peaks seen in the pure PEEK polymer. This demonstrates that the PEEK matrix in each of the ND/PEEK composites has essentially the same crystalline form as pure PEEK.

However, the peaks in the ND/PEEK patterns are shifted to somewhat larger values of 2θ, suggesting slight contraction of the unit cell dimensions. The values in Table 3.4 show some mostly small variations in unit cell dimensions among the samples, although there are definitive changes. The sample with the largest deviations is 1% son-OND/PEEK with an 11% increase in the b lattice parameter and a 25% decrease in the c parameter compared to pure PEEK. For the other samples, the changes in unit cell dimensions are less than 5%. Such variations could be related to varying cooling rates [81].

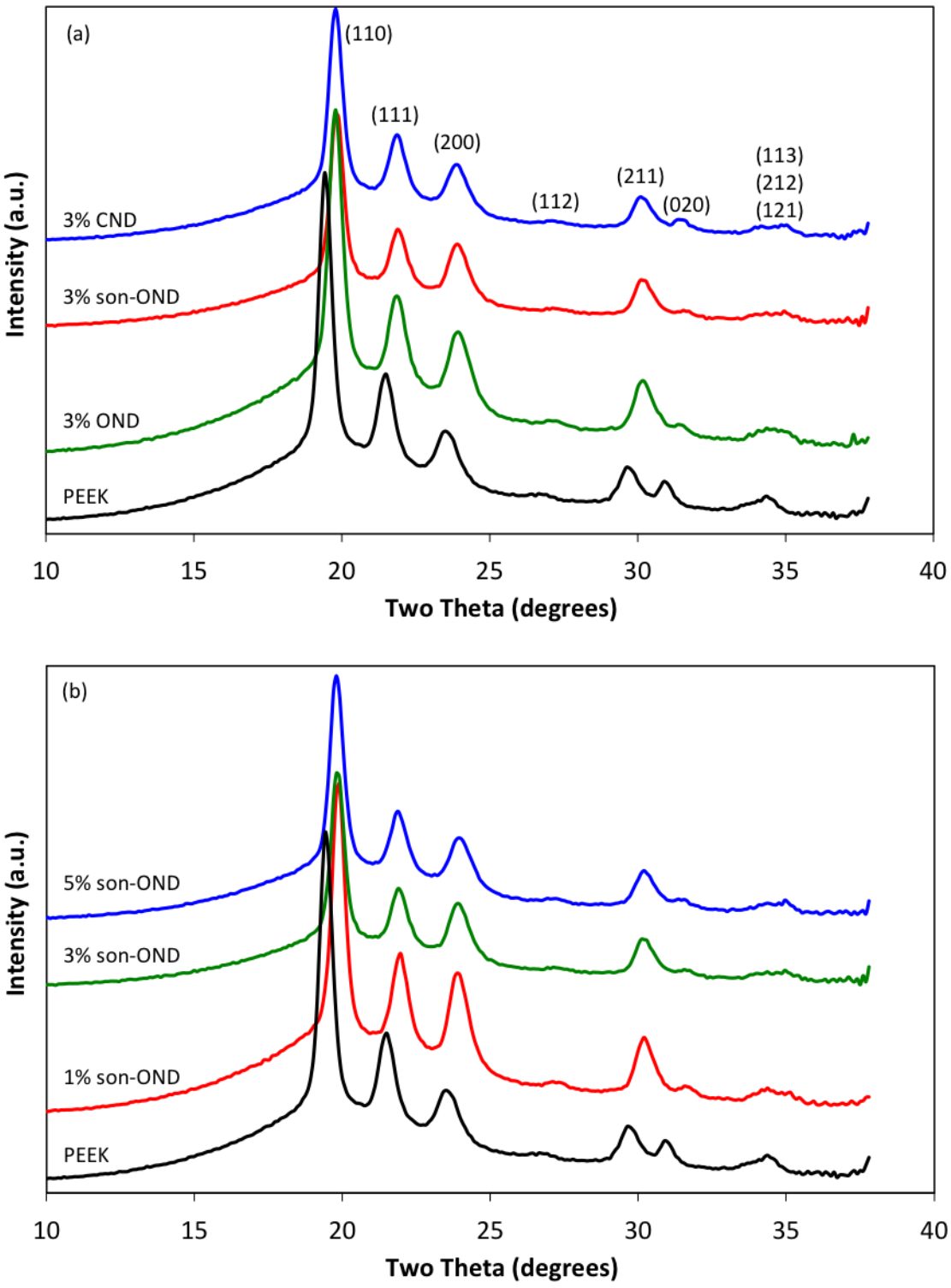

Figure 3.9. WAXS patterns for (a) pure PEEK and various 3% ND/PEEK composites, and (b) pure PEEK and son-OND/PEEK composites containing 1%, 3% and 5% son-OND. Miller indices are indicated in panel (a).

Table 3.4. Unit cell parameters for pure PEEK and ND/PEEK composites.

Sample	a (nm)	b (nm)	c (nm)
PEEK	0.754	0.573	0.974
1% son-OND	0.743	0.64	0.736
3% son-OND	0.743	0.560	0.968
5% son-OND	0.741	0.564	0.944
3% OND	0.744	0.561	0.959
3% CND	0.744	0.557	0.978

Figure 3.10 shows the MAXS scattered intensity profile for pure PEEK and ND/PEEK composites. The I(q) profile for pure PEEK is consistent with that observed previously [82, 83]. The most noticeable feature is the peak centered at about q=0.039 $Å^{-1}$, corresponding to the "long period" lamellar spacing of about 16 nm expected for PEEK [82]. The I(q) profiles for the ND/PEEK composites differ from that of pure PEEK in several ways. First, the scattered intensities for the ND/PEEK composites are significantly greater than that for pure PEEK at all q values below q~0.25 $Å^{-1}$. This indicates that the presence of the ND enhances or intensifies the X-ray scattering at low angles. Second, the peak in I(q) for PEEK becomes considerably broadened in the ND/PEEK profiles. Evidently the I(q) profiles for the ND/PEEK composites represent a convolution of the scattering from the ND filler and the PEEK lamellar structure.

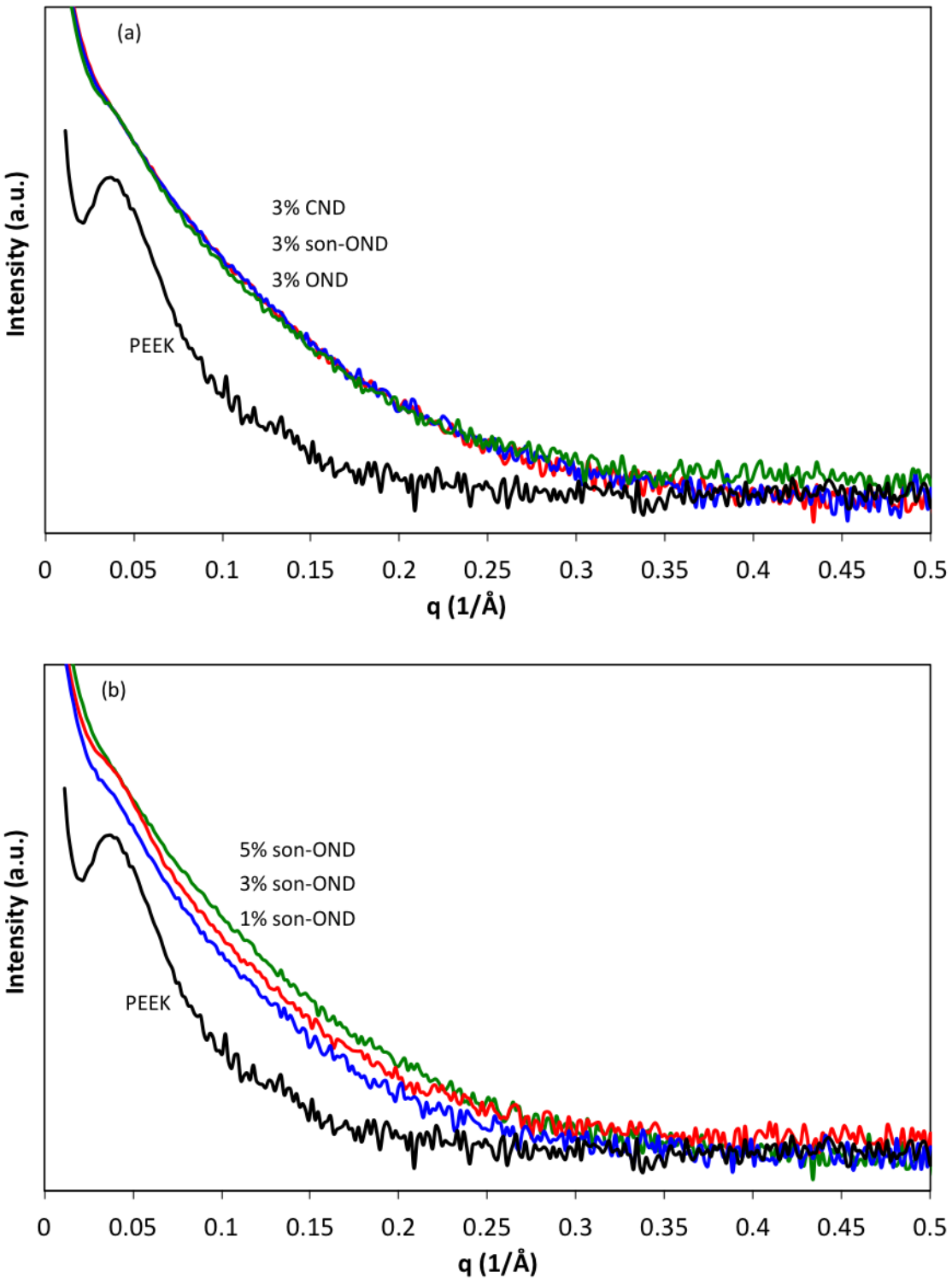

Figure 3.10. MAXS patterns for (a) pure PEEK and various 3% ND/PEEK composites, and (b) pure PEEK and son-OND/PEEK composites containing 1%, 3% and 5% son-OND.

The Lorentz correction [84] provides an approximate means of suppressing the contribution of single particle scattering in order to isolate and quantify scattering due to the internal structure of lamellar domains in semicrystalline polymers. Figure 3.11 shows Lorentz-corrected MAXS patterns for pure PEEK and ND/PEEK composites. All of these profiles show a peak in $q^2I(q)$ at approximately q=0.04 $Å^{-1}$. corresponding to a long-period lamellar spacing of about 16 nm. This result shows that the addition of PPA-modified OND to PEEK does not change the lamellar structure of the PEEK.

3.4.2 Mechanical Properties

3.4.2.1 Tensile Testing

The mechanical properties of pure PEEK and ND/PEEK composites were characterized via tensile testing and DMA. Figures 3.12 and 3.13 show typical stress-strain curves for PEEK and ND/PEEK composites. Additional figures in Appendix B provide stress-strain curves for multiple replicate specimens of each sample. All measured stress-strain curves exhibited linear behavior at low strains, allowing good estimates of Young's modulus.

The average tensile (Young's) modulus, tensile strength, elongation at break, and toughness (strain energy density) were determined from the replicate stress-strain curves and tabulated in Table 3.5. Figures 3.14-3.16 show the effect of varying loadings of son-OND on the tensile properties son-OND/PEEK composite fibers. The tensile

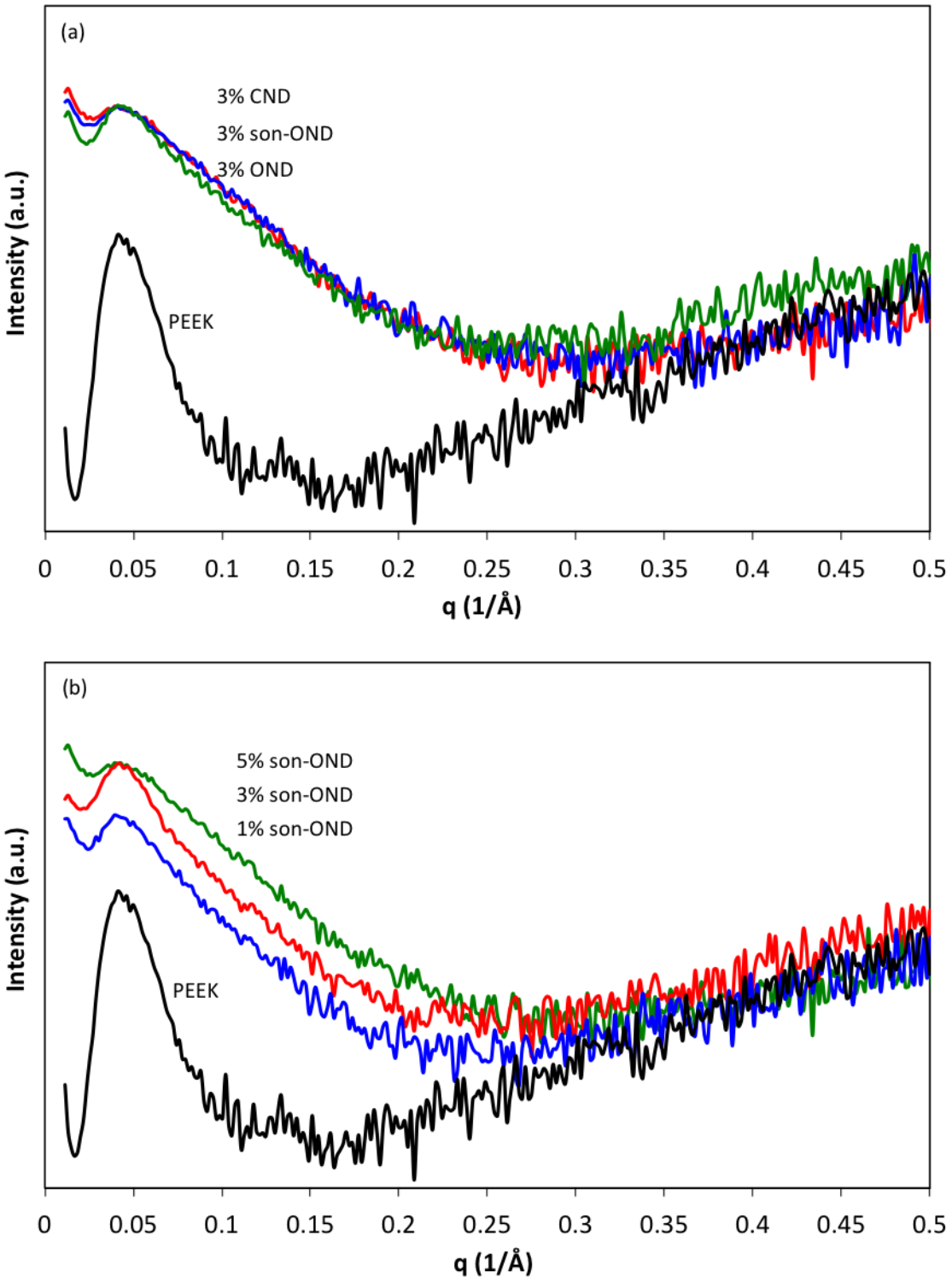

Figure 3.11. Lorentz-corrected SAXS patterns for (a) pure PEEK and various 3% ND/PEEK composites, and (b) pure PEEK and son-OND/PEEK composites containing 1%, 3% and 5% son-OND.

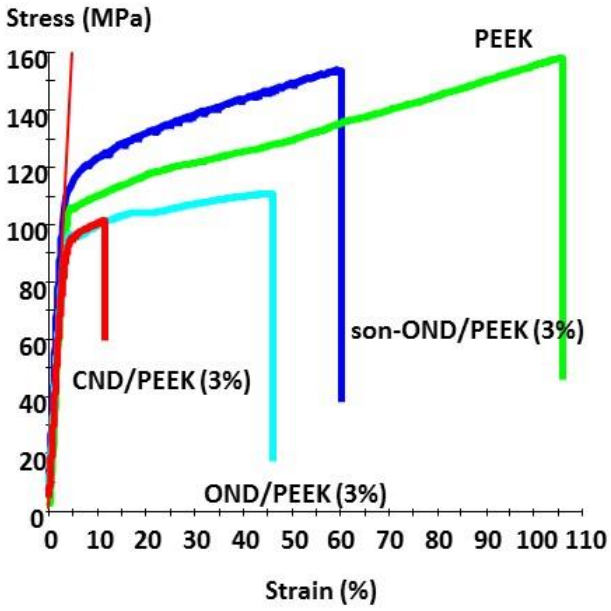

Figure 3.12. Typical stress-strain curves for pure PEEK, 3% OND/PEEK, 3% son-OND/PEEK, and 3% CND/PEEK.

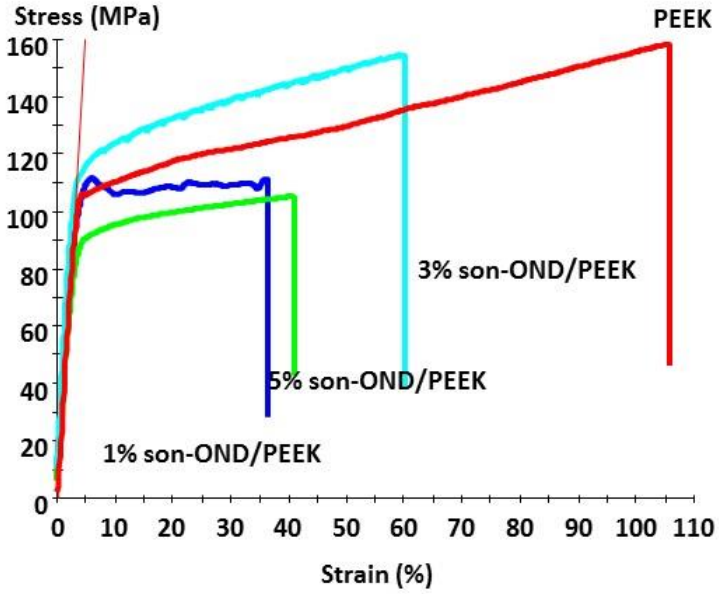

Figure 3.13. Typical stress-strain curves for PEEK and son-OND/PEEK composites.

Table 3.5: Mechanical properties of PEEK and PEEK based nanocomposite

Composites	Young's Modulus (GPa)	Tensile Strength (MPa)	Elongation at break (%)	Toughness (MPa.m)
PEEK	3.409±0.139	147.87±14.88	101.18±24.97	12.53±4.49
3% OND	3.297±0.194	112.75±9.74	56.65±15.98	6.12±2.36
3% CND	3.314±0.113	100.12±3.78	13.07±4.31	1.07±0.49
1% son-OND	3.403±0.184	107.66±10.94	38.37±15.85	3.75±2.03
3% son-OND	3.944±0.118	150.74±5.55	57.04±10.77	7.53±1.6
5% son-OND	3.207±0.219	110.62±10.84	38.86±15.36	3.85±1.56

Note: five replicate tests were performed for each sample.

(Young's) modulus of pure PEEK is 3.41 GPa (Table 3.4, Figure 3.14). The tensile modulus remains unchanged with the addition of 1 wt% son-OND. It seems that only 1 wt% of son-OND was not sufficient to affect the modulus of the matrix. With the addition of 3 wt% of son-OND, the tensile modulus increases by 16% to about 3.94 GPa, possibly as a result of increased interfacial area between the matrix and the nanoparticles. This increase is comparable to that observed in other PEEK nanocomposites incorporating larger amounts of other spherical inorganic nanoparticles (~15% for 7.5 wt% of 30 nm Al_2O_3 [16]. Such an increase in tensile modulus can be attributed to the improved dispersion of the nanoparticles, with smaller domain sizes and larger surface area contributing to the development of a larger interfacial region where the movements of the polymer chains are restricted due to interactions with the surface of the nanofillers [4].

With the addition of 5 wt% of son-OND, the composite's tensile modulus declined to 3.21 GPa (Table 3.4, Figure 3.14). It is possible that the higher content of son-OND resulted in the formation of agglomerates to such an extent that it had a

negative impact on the composite's tensile modulus. Statistical comparisons (t-test, 95% confidence Interval) indicate no significant difference among the tensile moduli of pure PEEK, 1% son-OND/PEEK, and 5% son-OND/PEEK composites.

Figure 3.15 shows that the ultimate tensile strength (tensile stress at break) of pure PEEK annealed fiber is 148 MPa. Addition of son-OND to the PEEK matrix either reduced or maintained the tensile strength of pure PEEK.

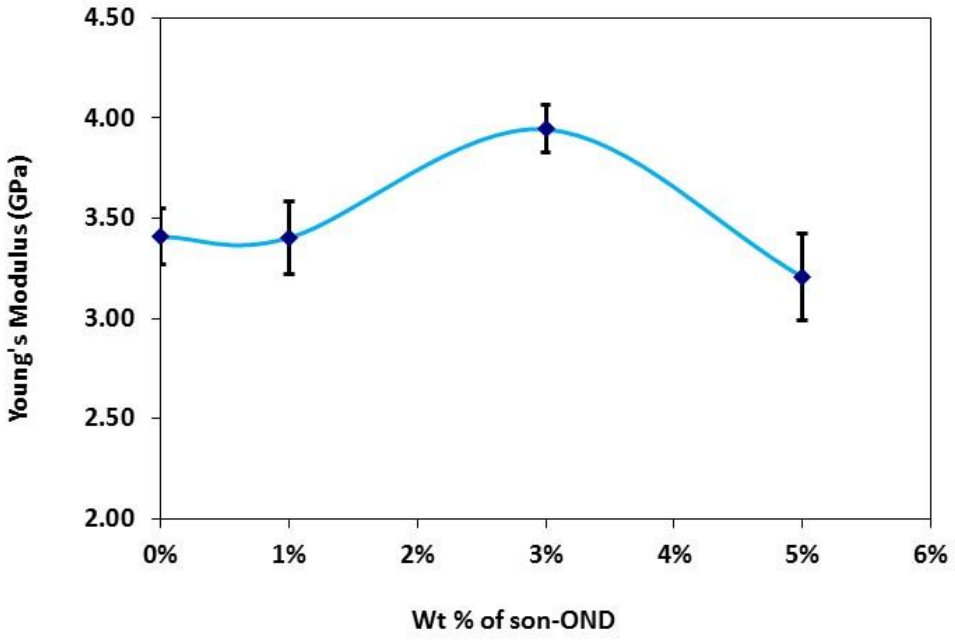

Figure 3.14. Young's Modulus of PEEK and ND/PEEK composites as a function of son-OND loading (wt%).

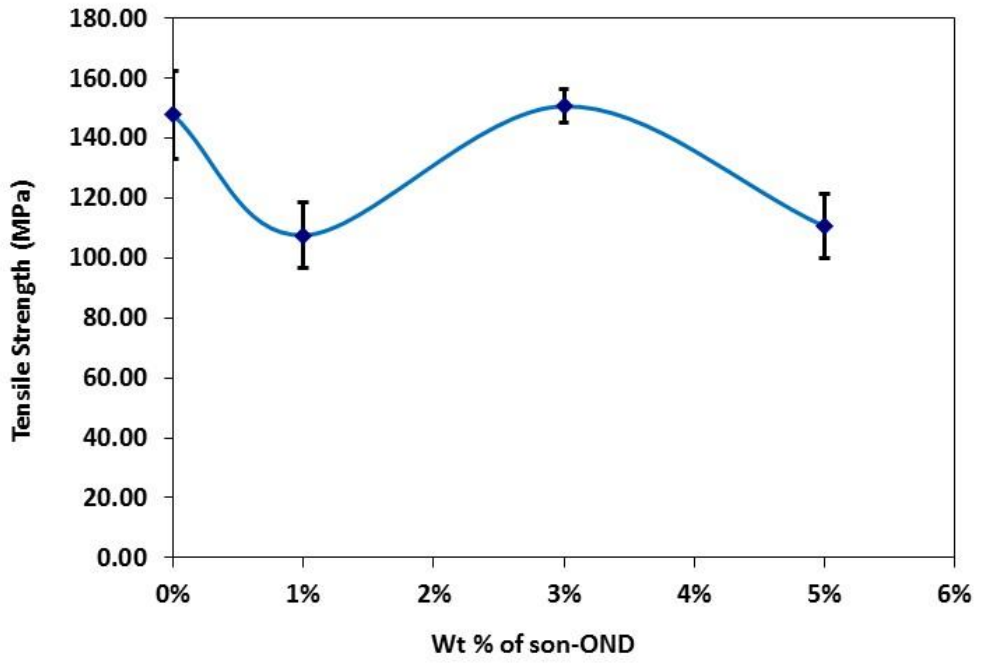

Figure 3.15. Tensile strength of PEEK and ND/PEEK composites as a function of son-OND loading (wt%).

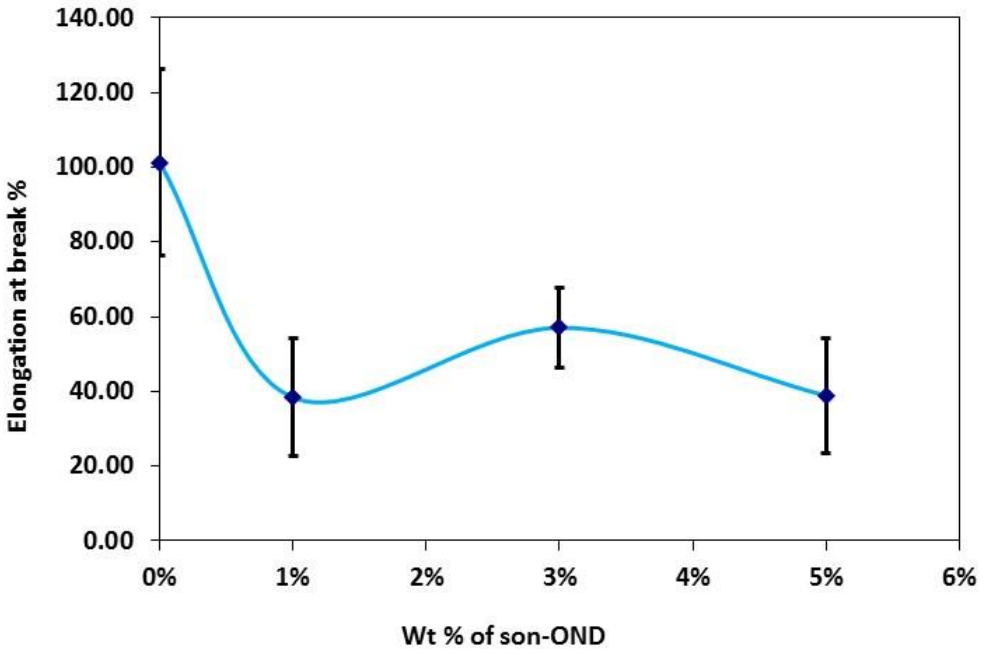

Figure 3.16. Elongation at break (%) for PEEK and ND/PEEK composites as a function of son-OND loading (wt%).

Figures 3.17-3.19 compare the tensile properties of 3% OND/PEEK, 3% CND/PEEK, and 3% son-OND/PEEK. The goal is to see if the type of PPA-modified ND (OND versus CND) or the use of sonication during grafting (son-OND versus OND) makes any difference in the composites' tensile properties. The tensile modulus (Figure 3.17) of 3% son-OND/PEEK is 20% higher than 3% OND/PEEK, 19% higher than 3% CND/PEEK and 16% higher than pure PEEK. This could be attributed to more complete surface coverage by PPA which results in better ND dispersion, weaker ND-ND attraction, or at least more favorable interaction between PEEK and the hydrophobic PPA-OND surface. In Figure 3.18, tensile strength results shows that the 3% son-OND/PEEK sample retained the strength of PEEK while the non-sonicated samples could not. Figure 3.19 shows that all ND/PEEK samples have reduced ductility than pure PEEK.

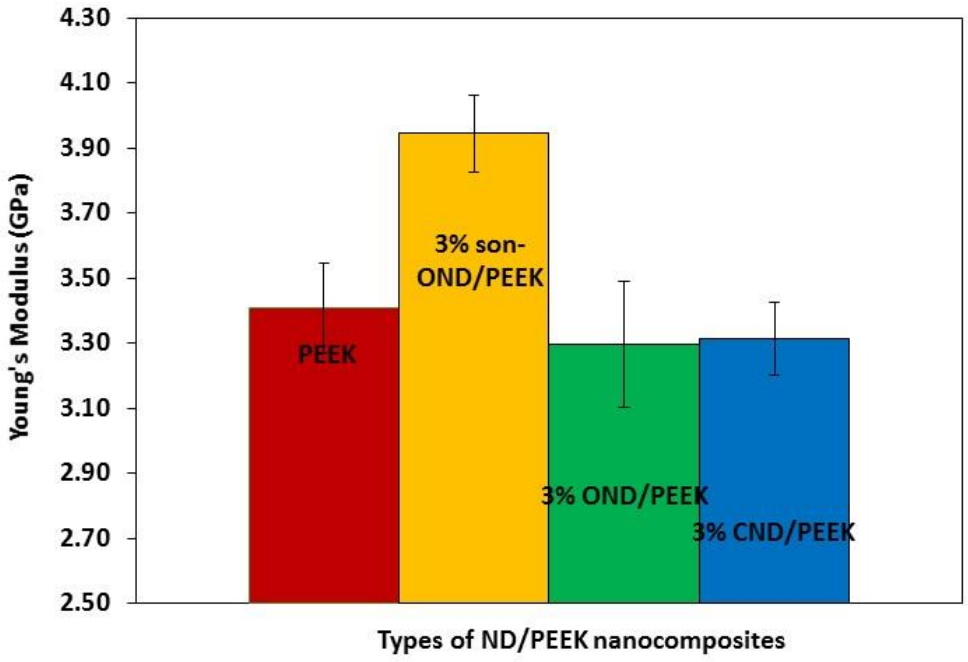

Figure 3.17. Young's modulus of pure PEEK, 3% son-OND/PEEK, 3% OND/PEEK, and 3% CND/PEEK.

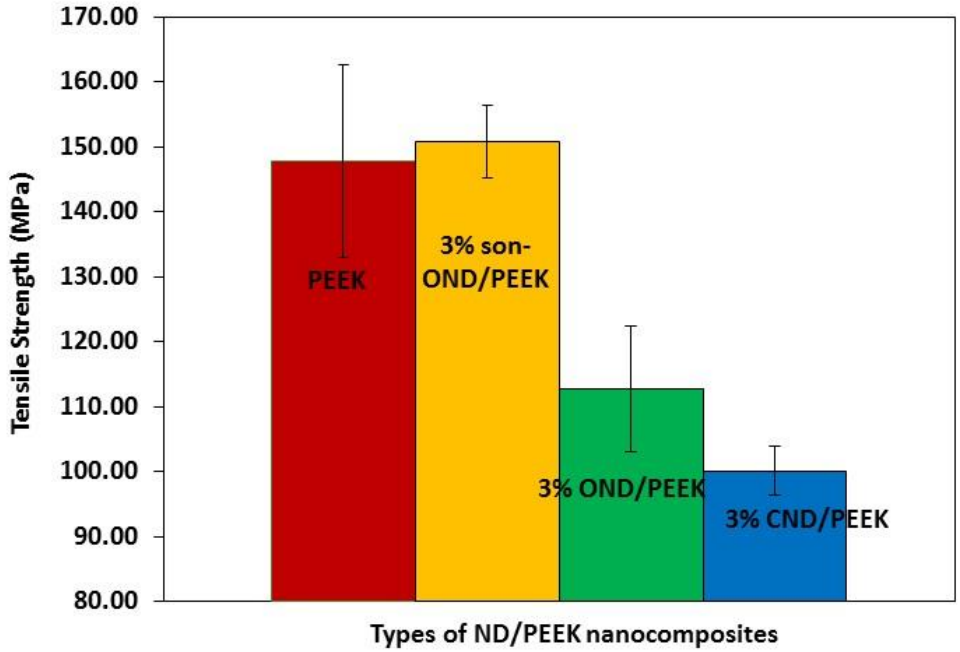

Figure 3.18. Tensile strength of pure PEEK, 3% son-OND/PEEK, 3% OND/PEEK, and 3% CND/PEEK.

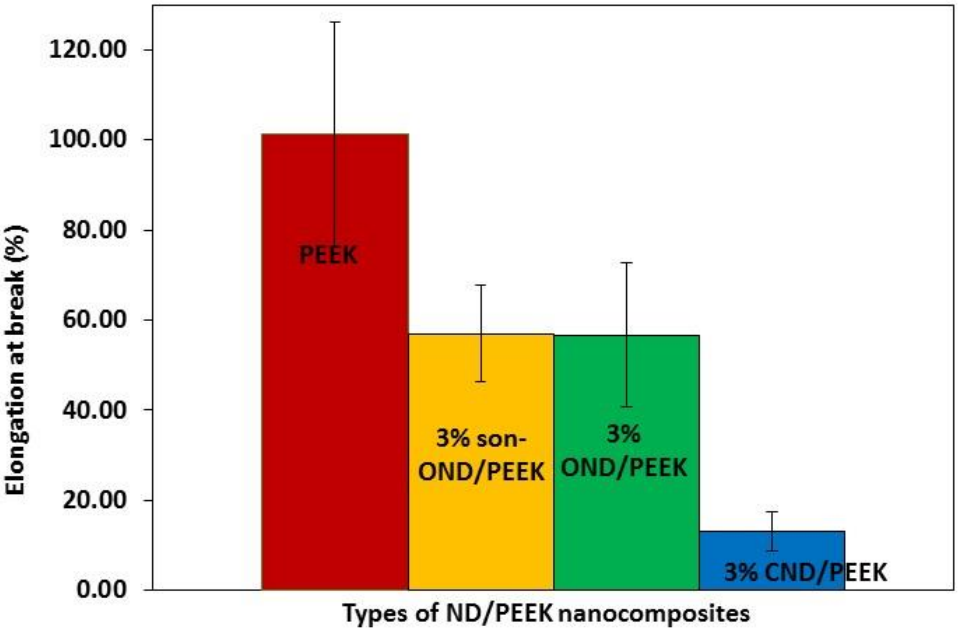

Figure 3.19. Elongation at break for pure PEEK, 3% son-OND/PEEK, 3% OND/PEEK, and 3% CND/PEEK.

3.4.2.2 DMA Measurements

Dynamic mechanical analysis (DMA) was used to characterize the effect of PPA-modified ND on the thermomechanical properties of the PEEK polymer. Figure 3.20 is a typical DMA storage modulus curve showing storage modulus (E') as a function of temperature for PEEK and various son-OND/PEEK composites. Figure 3.21 shows the corresponding loss tangent curves. At least three replicate specimens of each sample were tested, and average values were determined for storage modulus and loss tangent at specific temperatures, and the temperature of the loss tangent peak, which is one measure of T_g. The average values are compared in various figures below.

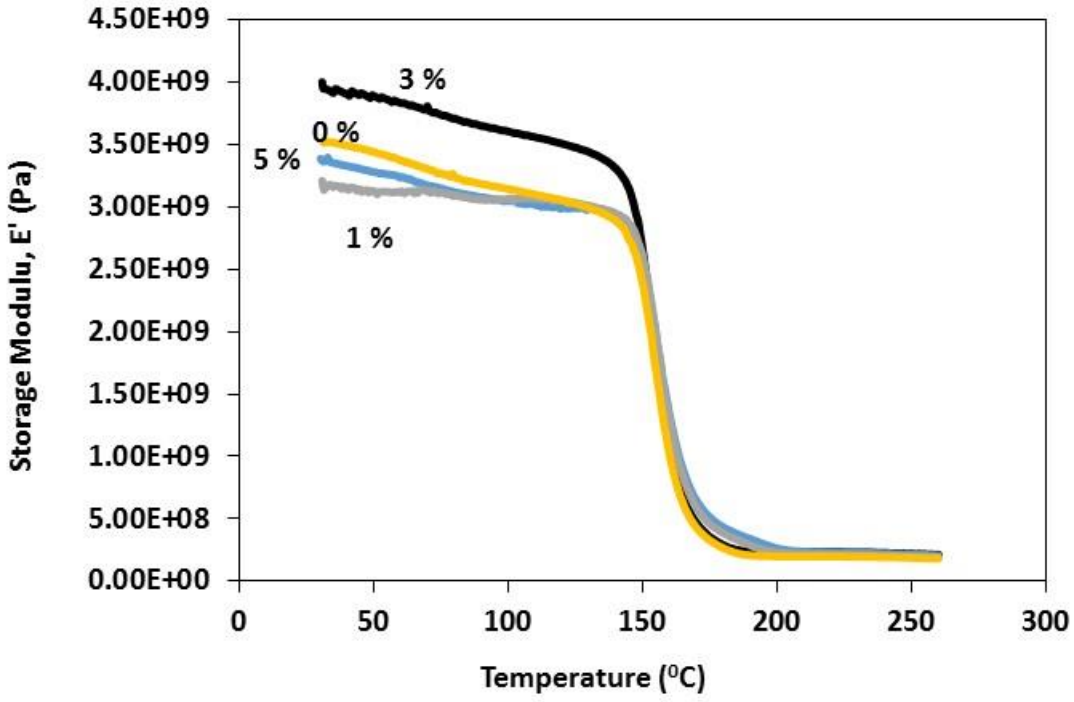

Figure 3.20. Storage modulus as a function of temperature for pure PEEK (0%) and son-OND/PEEK with 1, 3, and 5 wt % son-OND as labeled in the plot.

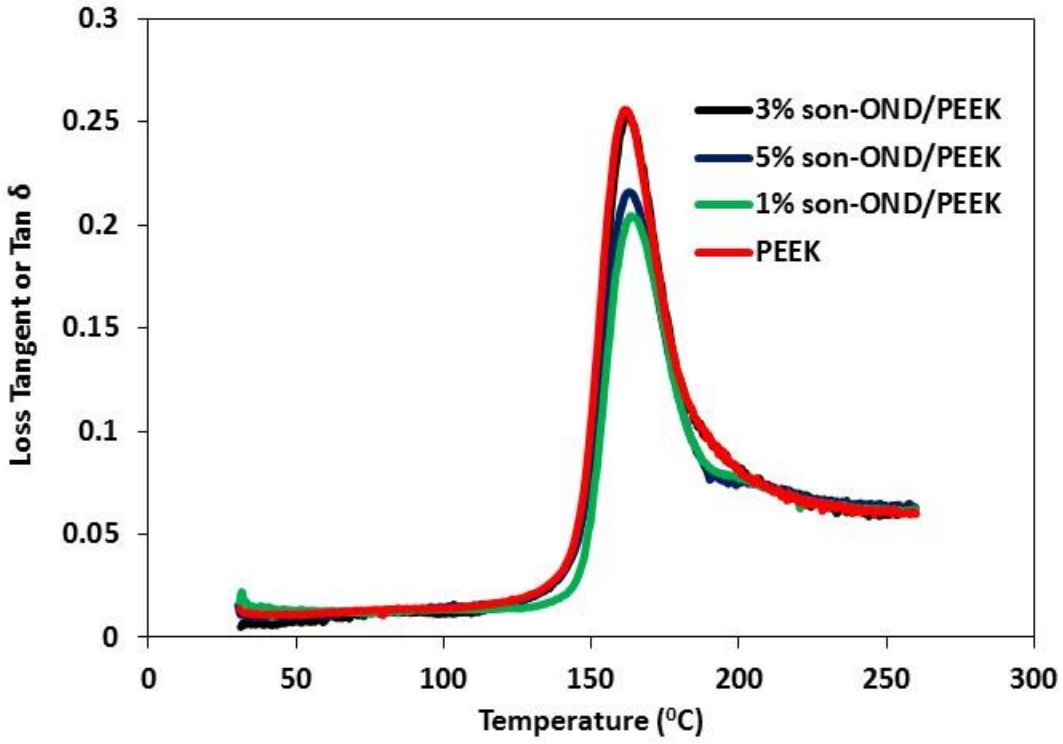

Figure 3.21. Loss Tangent (or Tan δ) as a function of temperature for pure PEEK (0%) and 1%, 3% and 5% son-OND/PEEK composite.

Figures 3.22 and 3.23 show the storage moduli (E') of PEEK and son-OND/PEEK composites at specific temperatures as functions of varying son-OND loading (wt%). It can be seen from this figure that the storage modulus of all son-ND/PEEK nanocomposites of different filler loading studied here reduces with increase in temperature due to the increased molecular relaxation of the PEEK molecules. The largest decrease in storage modulus is noticed beyond the glass transition temperature and above 150^{o}C as one would expect. At 50 ^{o}C addition of 1% son- OND didn't have any significant effect on the storage modulus, but addition of 3% son-OND increased the storage modulus by 16% (94% confidence). This observation is almost identical to what

was seen in the tensile results except the absolute modulus values are different in the two methods.

Figures 3.24 and 3.25 show the loss tangent (tan δ) of PEEK and son-OND/PEEK composites at specific temperatures as functions of varying son-OND loading (wt%). It can be seen that except for the curve of 150 ^{o}C, all curves of different temperatures are somewhat horizontal – indicating that the addition of different weight fractions (1-5%) doesn't have any significant effect to tan δ of the composite matrix. tan δ values of 50 ^{o}C and 100 ^{o}C is very similar and often overlaps.

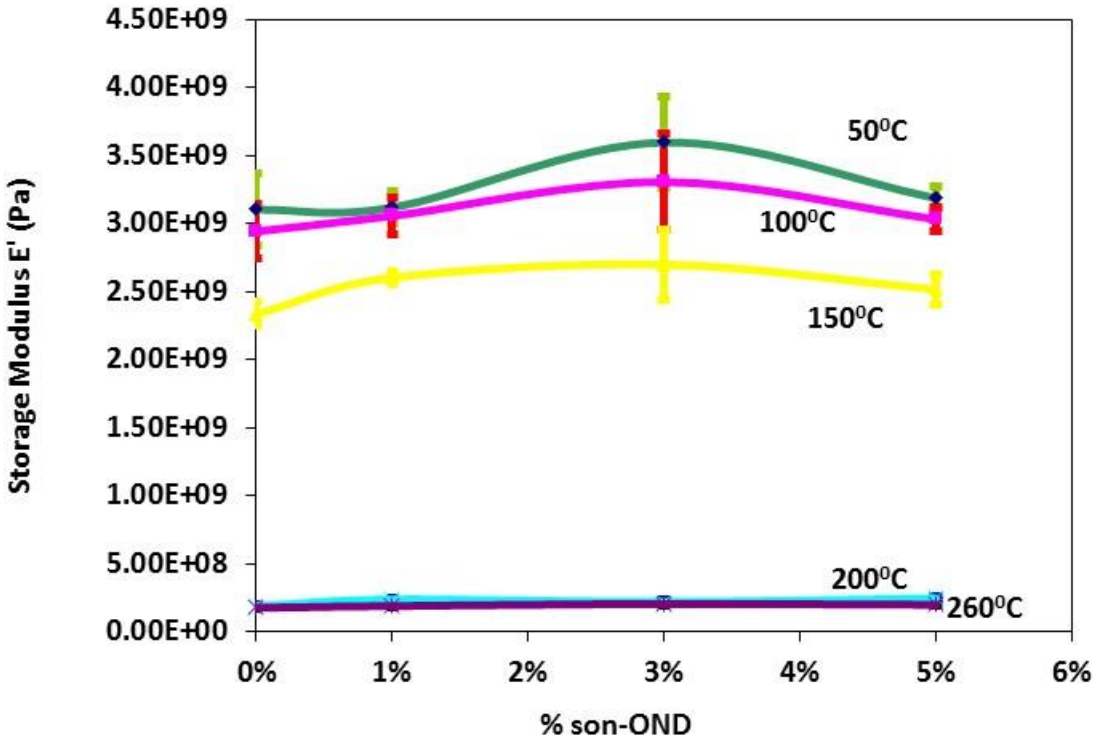

Figure 3.22. Storage modulus at specific temperatures for PEEK (0%) and son-OND/PEEK composites as functions of son-OND loading (wt%).

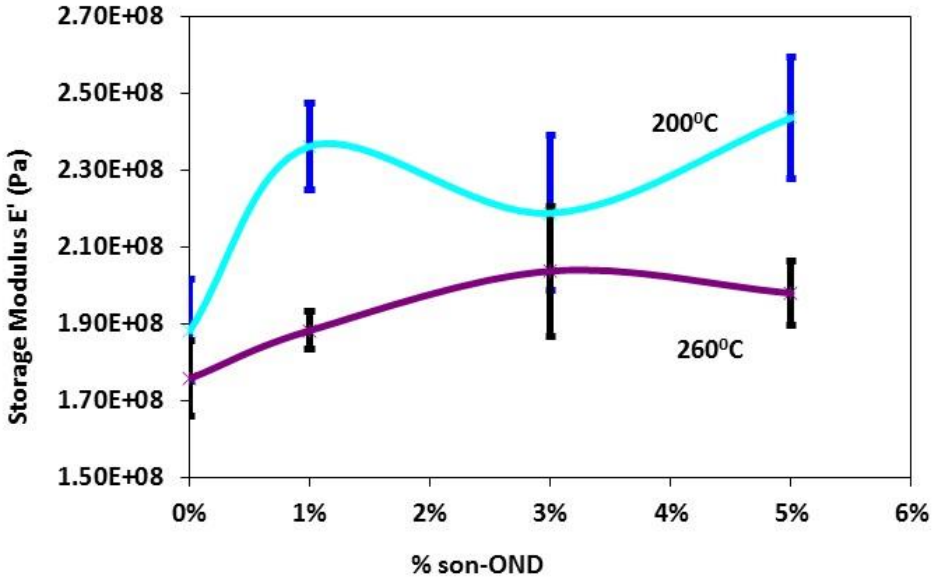

Figure 3.23. Storage modulus at specific temperatures in the rubbery regime for PEEK (0%) and son-OND/PEEK composites as functions of son-OND loading (wt%).

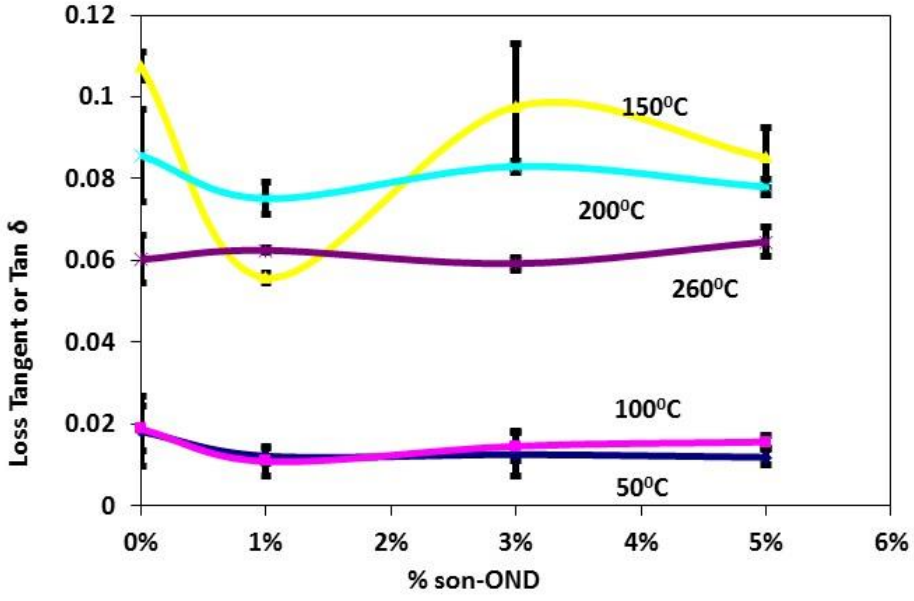

Figure 3.24. Loss tangent (tan δ) at specific temperatures for PEEK (0%) and son-OND/PEEK composites as functions of son-OND loading (wt%).

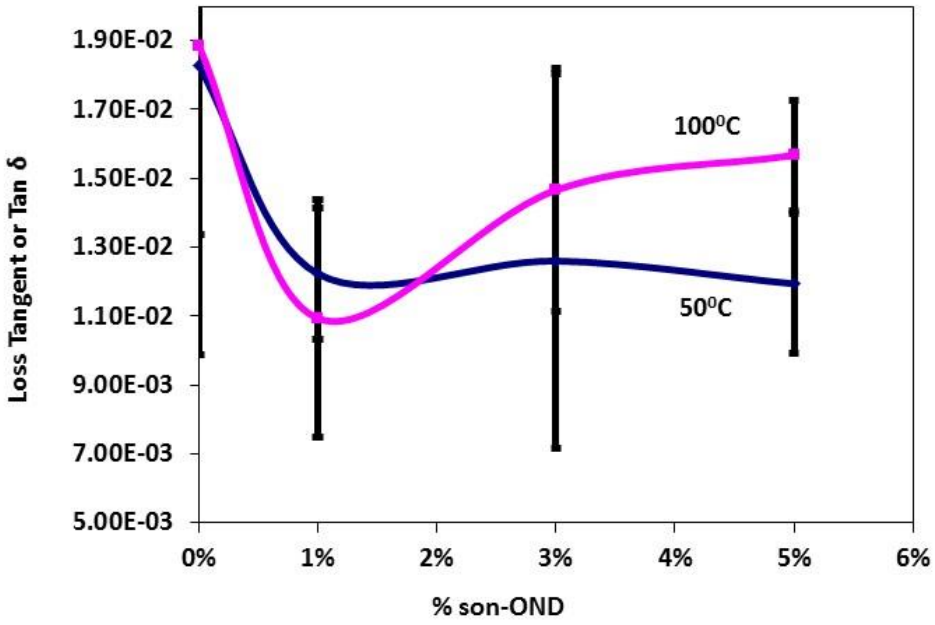

Figure 3.25. Loss tangent (tan δ) at specific temperatures in the rubbery regime for PEEK (0%) and son-OND/PEEK composites as functions of son-OND loading (wt%).

Figures 3.26 and 3.27 compare the storage moduli and loss tangents at 50°C of 3% OND/PEEK, 3% CND/PEEK, and 3% son-OND/PEEK. The goal is to see if the type of PPA-modified ND (OND versus CND) or the use of sonication during grafting (son-OND versus OND) makes any difference in the composites' thermomechanical properties. Figure 3.26 shows that the storage moduli of 3% son-OND/PEEK is 16% higher (94% CI) than pure PEEK. Figure 3.27 shows that if the variation of tan δ results (at 50 °C) of Pure PEEK, 3% son-OND/PEEK, 3% OND/PEEK and 3% CND/PEEK is taken into consideration, no significant difference is present between pure PEEK and these nanocomposites.

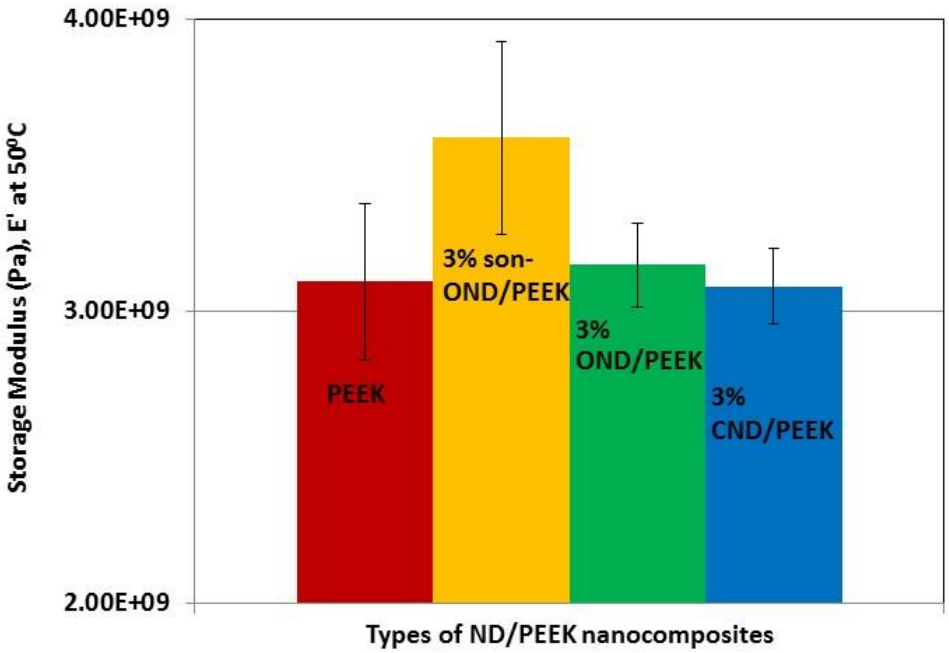

Figure 3.26. Storage modulus at 50°C for pure PEEK, 3% son-OND/PEEK, 3% OND/PEEK, and 3% CND/PEEK composites.

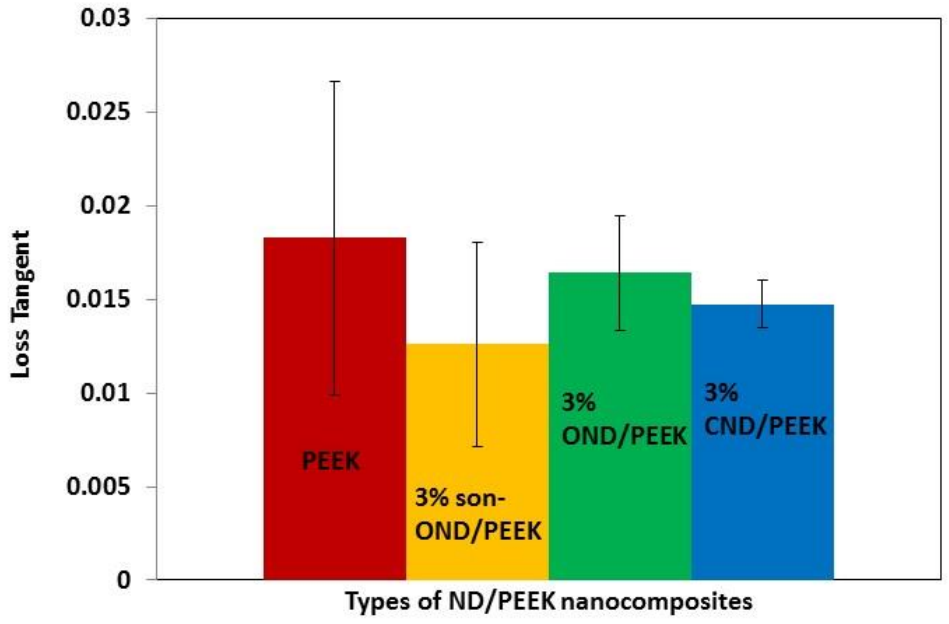

Figure 3.27. Loss tangent at 50°C for pure PEEK, 3% son-OND/PEEK, 3% OND/PEEK, and 3% CND/PEEK composites.

The temperature profiles of the storage moduli for PEEK and ND/PEEK composites (Figure 3.20) show the expected transition from glassy to rubbery behavior at approximately 150°C. The temperature of this transition is known as the glass transition temperature (T_g). There are several ways to define the value of T_g, all of which give slightly different values, including the inflection point in E'(T), the temperature of the peak value of the loss modulus E'' (not shown here), and the temperature of the loss tangent peak (Figure 3.21). This study uses the latter to define the T_g value. As shown in Figure 3.28, and also according to T-test, there is small but significant difference between T_g of pure PEEK and 1% and 5% son-OND/PEEK. Pure PEEK T_g is slightly lower than both. The difference between the T_g of 3% son-OND/PEEK and pure PEEK is not significant.

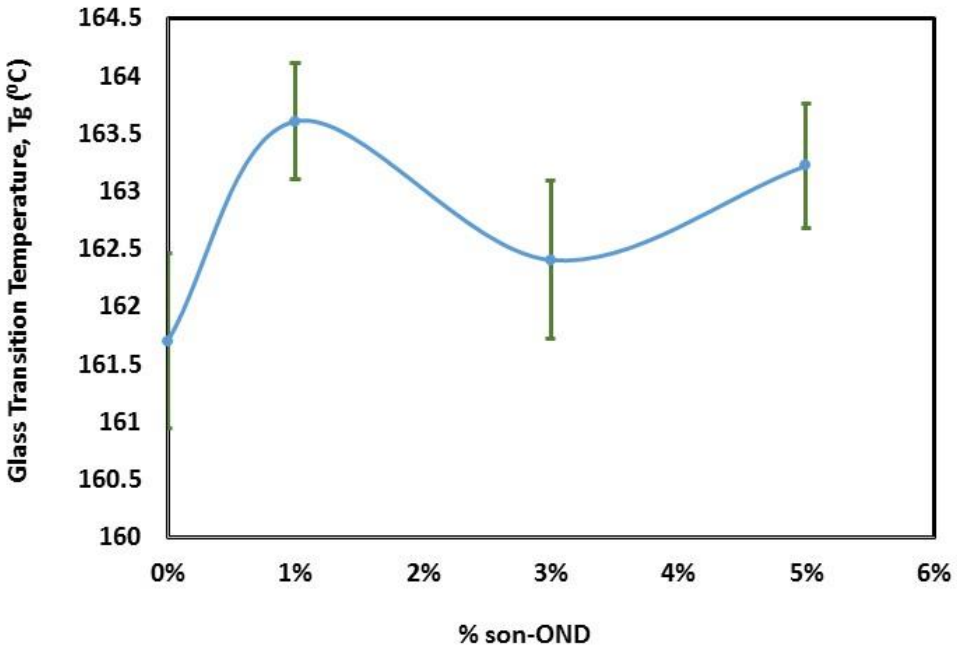

Figure 3.28. Glass transition temperature for PEEK (0%) and son-OND/PEEK composites as a function of son-OND loading (wt%).

Figure 3.29 compares T_g values for pure PEEK, 3% son-OND/PEEK, 3% OND/PEEK, and 3% CND/PEEK composites. In these samples, we don't observe any statistically significant differences in T_g values.

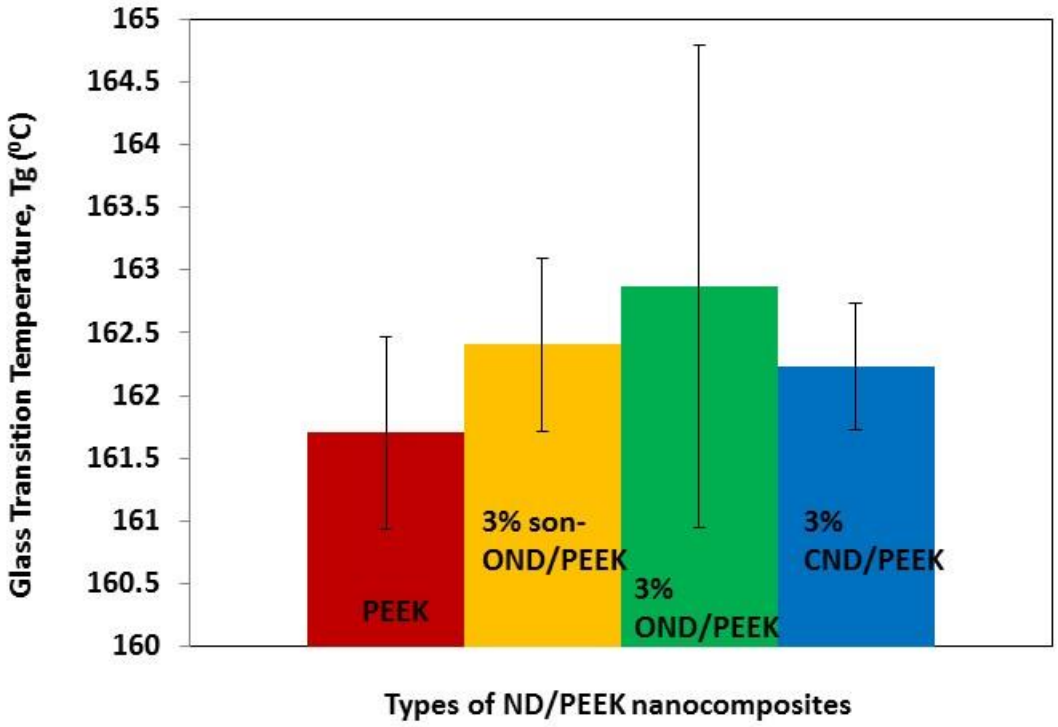

Figure 3.29. Glass transition temperatures for pure PEEK, 3% OND_{son}/PEEK, 3% OND/PEEK, and 3% CND/PEEK composites.

3.4.3. Thermal Properties

3.4.3.1. PEEK Crystallinity via DSC

The thermal properties of PEEK and ND/PEEK composites have been characterized by DSC measurements. These measurements provide information on

PEEK crystallinity that complements the results obtained from X-ray scattering. Figures 3.30-3.32 show first heating, first cooling, and second heating scans. Table 3.6 presents melting and crystallization characteristics extracted from the DSC scans.

Table 3.6. Thermal properties of PEEK and ND/PEEK composites as characterized by DSC.

Sample ID	Cooling Cycle			2nd Heating Cycle			
	T_C (^{0}C)	ΔH_C (J/gm)	X_C (%)	T_g (^{0}C)	T_m (^{0}C)	ΔH_f (J/gm)	X_C (%)
APEEK	305.21	50.18	38.60%	148.39	343.69	43.78	33.67%
PEEK	304.06	49.25	37.88%	146.66	343.30	44.22	34.02%
1% son-OND/PEEK	299.73	49.45	38.42%	146.90	342.49	45.25	35.16%
3% son-OND/PEEK	300.13	48.85	38.74%	146.84	342.36	45.21	35.85%
5% son-OND/PEEK	299.67	46.61	37.74%	145.84	341.94	43.43	35.16%
3% OND/PEEK	300.68	45.95	36.44%	145.56	342.43	44.05	34.93%
3% CND/PEEK	299.65	44.55	35.33%	148.12	342.13	40.83	32.38%

T_C (^{0}C)- Peak temperatures of crystallization exotherm, T_m (^{0}C) – Peak temperature of melting, T_g (^{0}C) – Glass transition temperature (mid point), ΔH_C – Heat of crystallization, ΔH_f – Heat of fusion, X_C (%) - % Crystallinity.

Considering the first heating scans (Figure 3.30), the most obvious feature is the crystallization exotherm in the heating curve for amorphous PEEK. This exotherm occurs at about 160°C, about 15°C above T_g, and occurs due to a cold crystallization process. This was the only sample that was not annealed before the test. Cold crystallization occurs in polymer samples that are rapidly cooled (quenched) below T_g, thereby locking in a metastable amorphous chain structure. Upon heating above T_g, the polymer chains have freedom to move, and the structure relaxes to the preferred equilibrium state by undergoing crystallization. Considering that all of the other samples had been thermally annealed at 200°C, we would not expect to observe cold crystallization exotherms in any of the other samples.

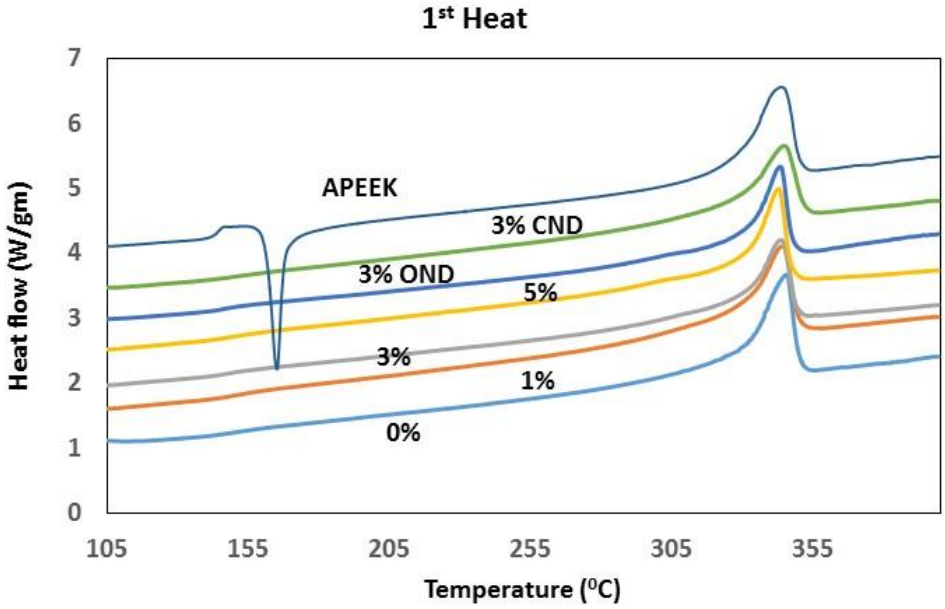

Figure 3.30. DSC first heating scans for PEEK, APEEK, and various ND/PEEK composites.

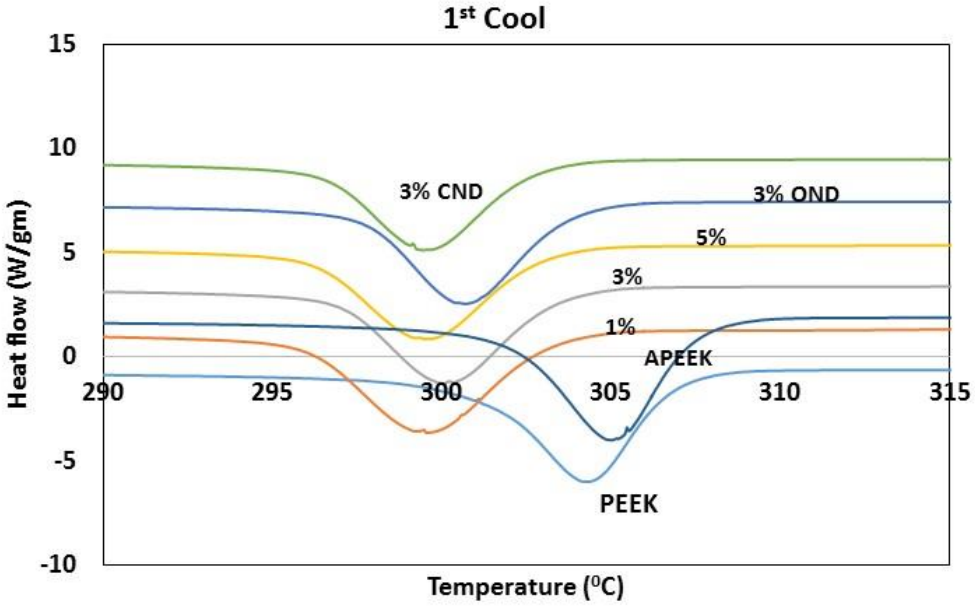

Figure 3.31. DSC first cooling scans for PEEK, APEEK, and various ND/PEEK composites.

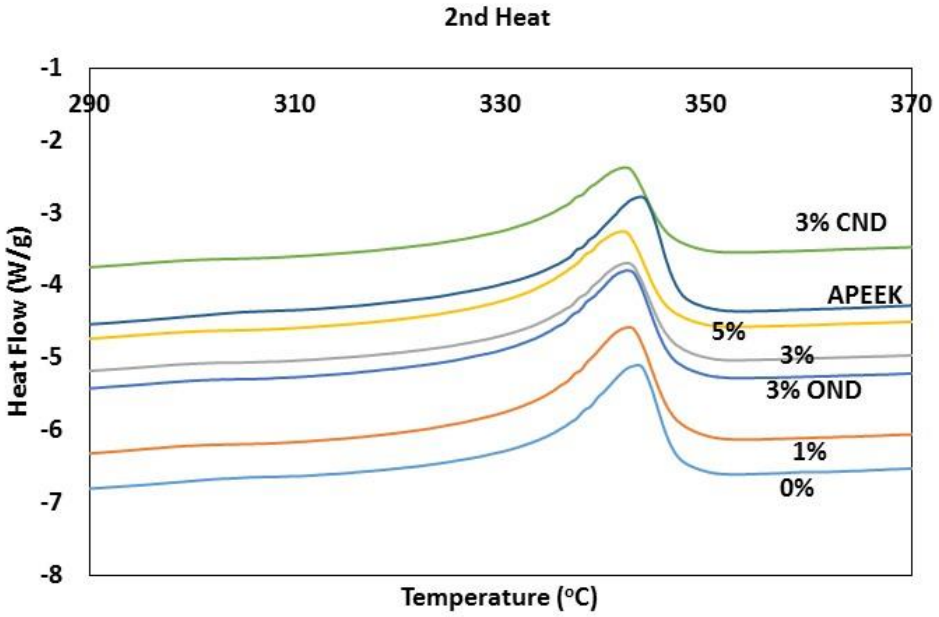

Figure 3.32. DSC second heating scans for PEEK, APEEK, and various ND/PEEK composites.

The first cooling curves (Figure 3.31) show a significant difference between the pure PEEK samples (both crystalline and amorphous) and the ND/PEEK composites. The peak temperatures of crystallization exotherms for all of the ND/PEEK composites are approximately 4-5°C lower than those of pure PEEK. This means that as cooling proceeded, crystallization was delayed in all of the ND/PEEK composites compared to pure PEEK. Other researchers have reported the similar crystallization behavior in other PEEK nanocomposite systems [16, 15, 18]. In some cases [4], small quantities of nanoparticles can act as a nucleation sites and increase the crystallization temperature of PEEK nanocomposites. However, larger quantities of filler particles have also been found to lower the crystallization temperature [18]. Addition of nanoparticles can have two competing effects on crystallization behavior, namely on heterogeneous

nucleation and polymer chain mobility. If the nanoparticles supply nucleating sites, this promotes heterogeneous nucleation, and the crystallization temperature may be higher than that of the pure PEEK during the cooling scan. On the other hand, the presence of filler particles hinders the mobility of polymer chains and thereby impedes the formation of crystal lamellae [18, 85], shifting the crystallization temperature to values lower than pure PEEK during cooling. For all of the PPA-modified ND/PEEK composites, the mobility effect dominates: the shift of crystallization temperatures to lower values indicates that the PPA-modified ND filler hinders the mobility of the PEEK chains.

Values of crystallization enthalpy and degree of crystallinity (X_c, Table 3.6) have unknown levels of uncertainty due to error and bias involved in computing the areas associated with the crystallization peaks. Considering the values derived from the crystallization exotherms in the first cooling curves, X_c values for son-OND/PEEK composites are comparable to those for pure PEEK. The crystallinity of 3% OND/PEEK appears to be slightly lower than PEEK. The crystallinity of 3% CND/PEEK is about 7% lower than that of PEEK, which appears to be significant.

The second heating curves (Figure 3.32) provide some corroborating information. The melting endotherms for all of the ND/PEEK composites have T_m values that are about 0.5 to 1°C lower than those for pure PEEK, but it is not clear if this difference is significant. Based on the melting endotherms in the second heating curves, PEEK's degree of crystallinity (X_c) is about 34%, those of OND/PEEK composites (both sonicated and non-sonicated) are about 35%, and that of 3% CND/PEEK is lower: about

32.4%, which is 5% lower than PEEK's X_c value. This is consistent with the observation based on the first cooling curves.

The overall picture is that PPA-modified CND inhibits PEEK crystallization. On the other hand, PPA-modified OND may enhance PEEK crystallization, or at least does not inhibit it. The different levels of PPA grafting on OND versus CND may explain this. In Chapter 2, we reported that PPA grafting was at least 2 times higher (per unit area) on OND compared to CND. The higher level of PPA grafting on OND creates a surface that is relatively rich in phenyl groups expected to interact favorably with aromatic PEEK. Because PPA-modified OND "looks" more like PEEK, it does not hinder PEEK crystallization. In contrast, the surface of PPA-modified CND has half the PPA graft density, so it's "aromaticity" lies between unmodified CND and PPA-modified OND. The interaction between PEEK and the surface of PPA-modified CND, whatever it may be, apparently inhibits PEEK crystallization.

3.4.3.2 Thermal Stability

The thermal stability of PEEK and ND/PEEK composites were characterized via TGA, which measures sample weight loss in air and nitrogen atmospheres, during dynamic thermal ramping and isothermally over time. Figure 3.33 compares the thermal stability of son-OND/PEEK composites with pure PEEK measured dynamically in air. These materials exhibit little or no weight loss upon heating from room temperature to about 500°C. Significant weight loss may be observed beginning at 500°C for 5 wt% son-OND/PEEK, and at about 560°C for 1 and 3 wt% son-OND/PEEK. In Chapter 2 [77], we observed that PPA-modified OND starts to degrade at about 500-550°C when heated in

air. Based on this information, the onset of thermal degradation observed in son-OND/PEEK composites can probably be attributed to PPA degradation. For 5 wt% son-OND/PEEK, the degradation becomes apparent at a lower temperature due to the higher PPA content.

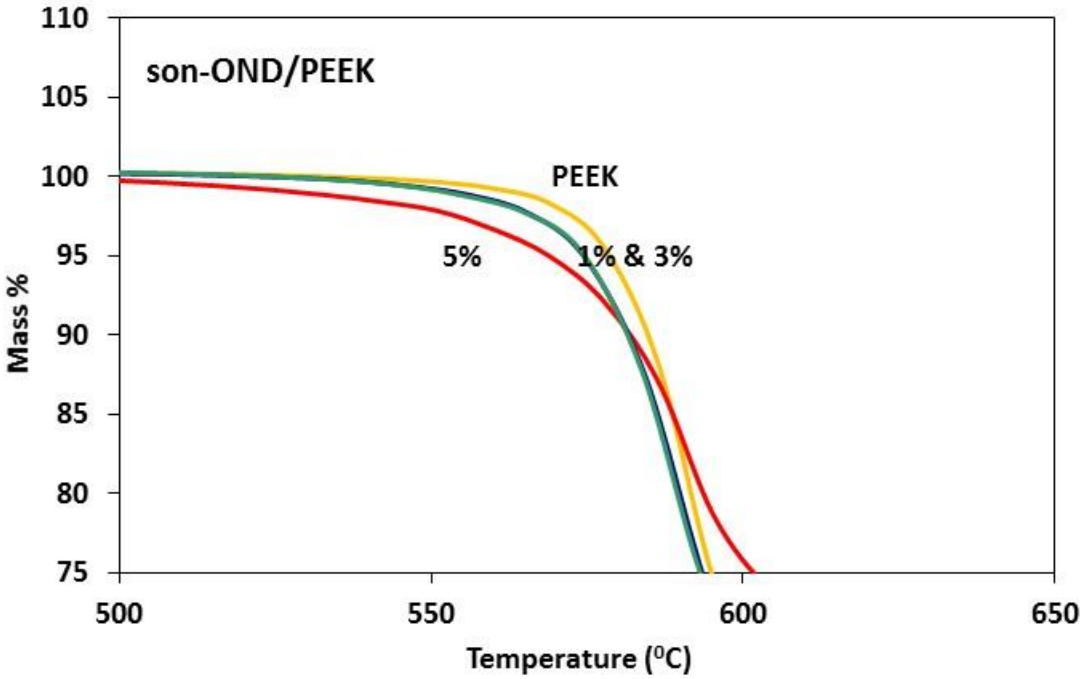

Figure 3.33. Weight loss (%) in air versus temperature for pure PEEK (0%) and son-OND/PEEK composites with the indicated son-OND weight loadings. Temperature ramp was 10°C/min.

Figure 3.34 compares the thermal stability in air of 3% OND/PEEK (sonicated and non-sonicated during PPA modification), 3% CND/PEEK, and pure PEEK. In terms of thermal stability, the observed trends are similar to the observations reported above. The onset of thermal degradation becomes apparent at about 550°C for all of the

composites. Again, this appears to be due to the onset of PPA thermal degradation. The additional sonication step for PPA grafting on ND does not confer any additional benefit for thermal stability of PPA-modified ND/PEEK composites.

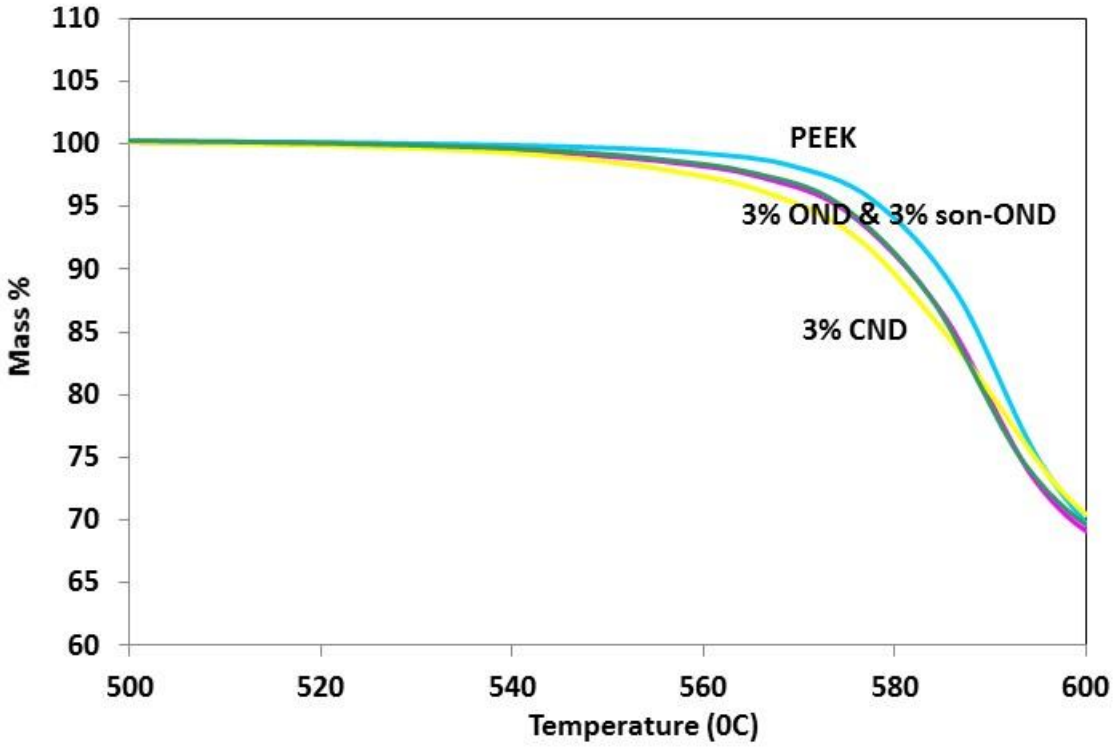

Figure 3.34. Weight loss (%) in air versus temperature for pure PEEK (0%), 3% son-OND/PEEK, 3% OND/PEEK, and 3% CND/PEEK composites. Temperature ramp was 10°C/min.

Figures 3.35 and 3.36 presents the dynamic TGA weight loss data for PEEK and ND/PEEK composites heated in a nitrogen gas environment. The absence of oxygen precludes thermal degradation due to oxidation. Nonetheless, Figures 3.35 and 3.36 show the same trends observed previously for thermal degradation in air. This implies that oxidation of the ND itself is not playing a significant role in thermal stability. This

result supports the view that the non-oxidative thermal degradation of PPA is responsible for the onset of thermal degradation in these PPA-modified ND/PEEK composites.

Figures 3.37 and 3.38 present the isothermal TGA data for ND/PEEK composites in air and nitrogen environments. The temperature was ramped to 365°C (the typical melt processing temperature for PEEK) and then maintained at that temperature for one hour. None of the ND/PEEK composites show any significant weight loss during the isothermal period, either in air or nitrogen. The isothermal TGA data indicates that, irrespective of surface modification or ND content, all ND/PEEK composites have excellent thermal stability at PEEK processing temperature for at least 60 minutes.

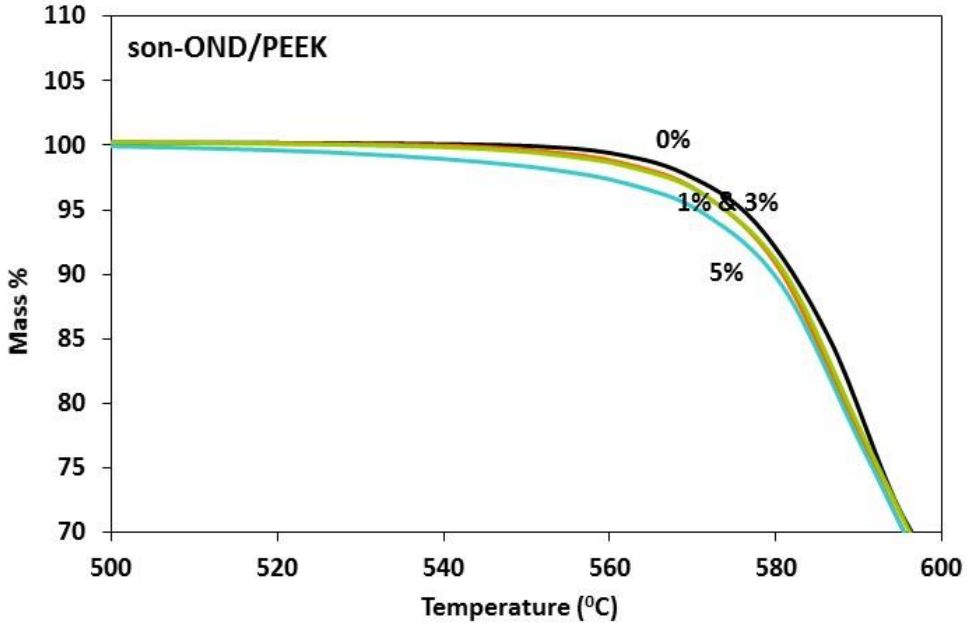

Figure 3.35. Weight loss (%) in nitrogen versus temperature for pure PEEK (0%) and son-OND/PEEK composites with the indicated son-OND weight loadings. Temperature ramp was 10°C/min.

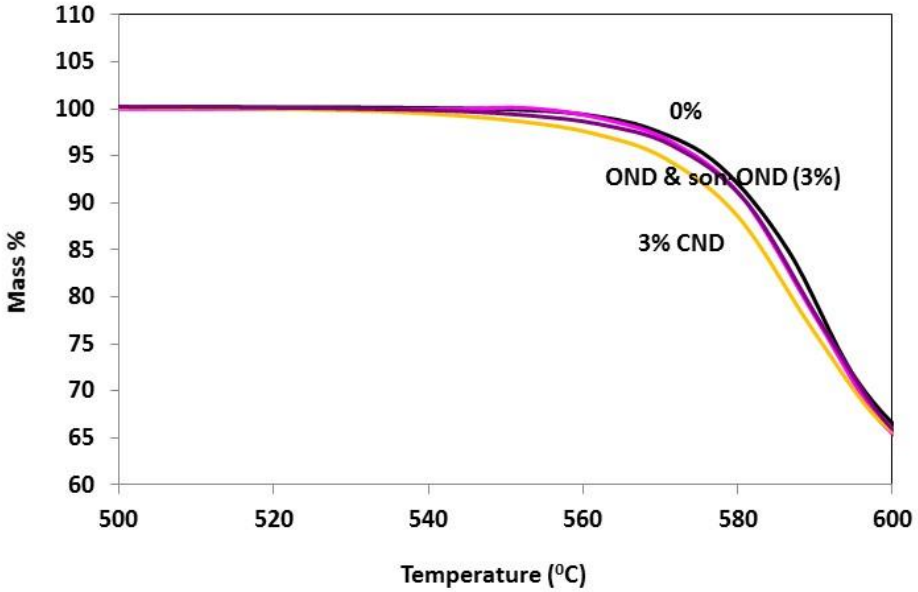

Figure 3.36. Weight loss (%) in nitrogen versus temperature for pure PEEK (0%), 3% OND_{son}/PEEK, 3% OND/PEEK, and 3% CND/PEEK composites. Temperature ramp was 10°C/min.

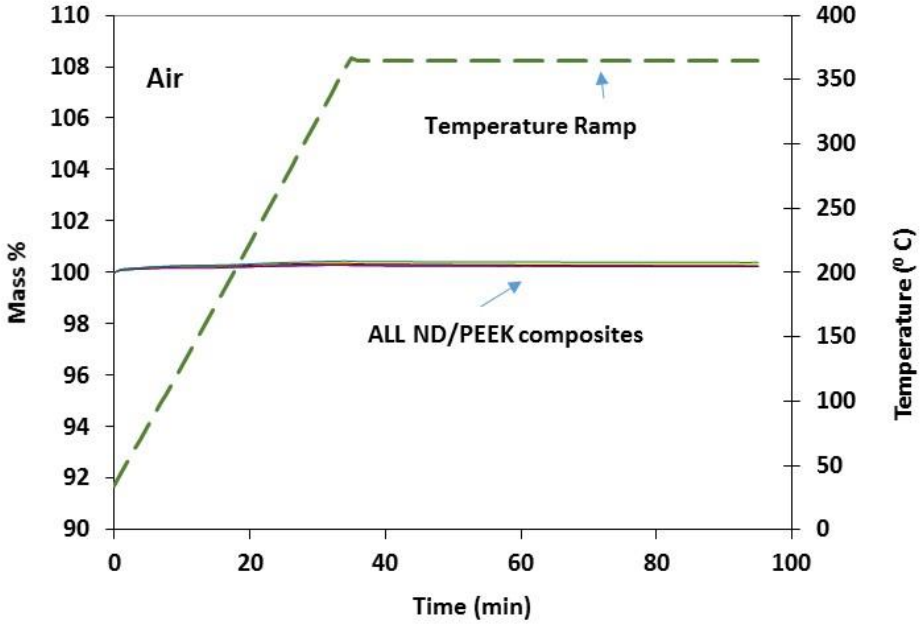

Figure 3.37. Weight loss (%) in air versus time for pure PEEK (0%), 1%, 3% and 5% son-OND/PEEK, 3% OND/PEEK, and 3% CND/PEEK composites. The dashed curve indicates the time-dependent temperature profile.

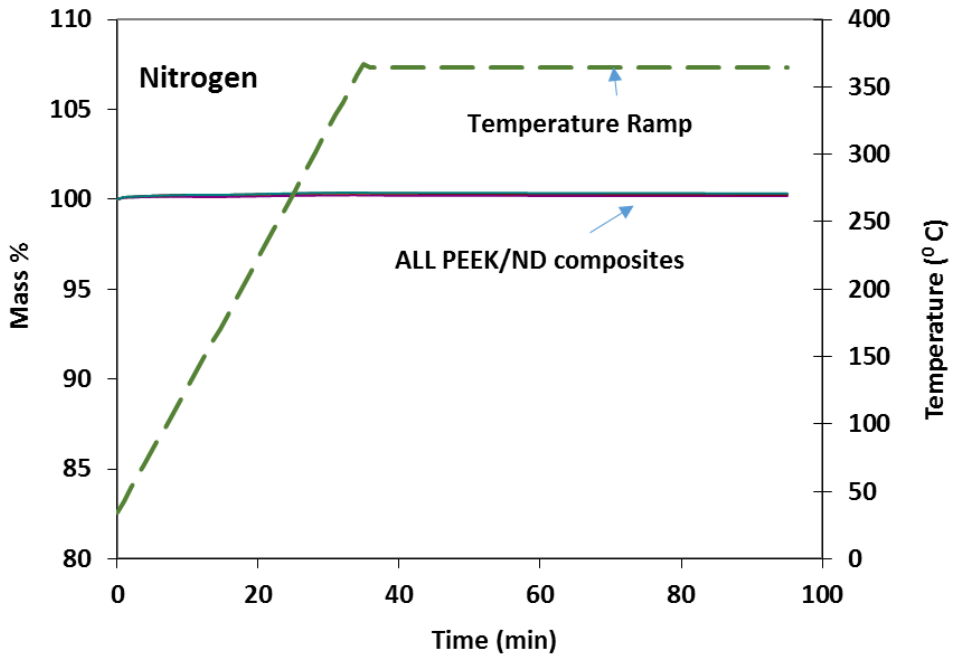

Figure 3.38. Weight loss (%) in nitrogen versus time for pure PEEK (0%), 1%, 3% and 5% son-OND/PEEK, 3% OND/PEEK, and 3% CND/PEEK composites. The dashed curve indicates the time-dependent temperature profile.

3.4.4 Thermal Conductivity

Figure 3.39 shows the thermal conductivity (k) of son-OND/PEEK composites containing varying loadings of son-OND. The measured k value for pure PEEK, about 0.26 W/mK is close to the values (0.23 to 0.29) reported in literature [6, 9, 10]. Upon addition of son-OND, the composite thermal conductivity increases. Adding 1% son-OND results in a k= 0.32 W/mK, a 25% increase over pure PEEK. The composite thermal conductivity reaches a maximum value of about 0.35W/mK for 3% son-OND/PEEK, a value 38% higher than pure PEEK. For the highest loading of 5% son-OND, the

composite thermal conductivity declined relative to that for 3% son-OND/PEEK, but the k value at 0.31 is still 22% greater than that of pure PEEK.

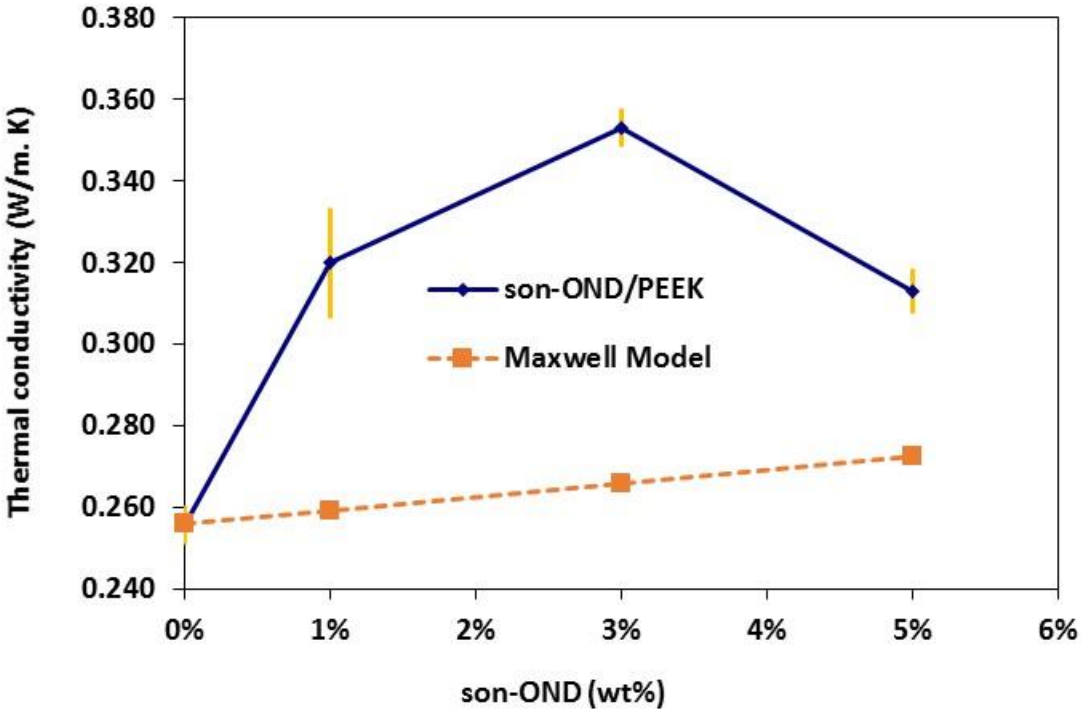

Figure 3.39. Thermal conductivity of son-OND/PEEK composites as a function of the son-OND loading (wt%). The dashed curve shows the Maxwell model prediction for the composites' effective thermal conductivity.

Figure 3.39 also plots the predicted composite thermal conductivity based on the Maxwell model [86], given by

$$\lambda_c = \lambda_m \frac{\lambda_f + 2\lambda_m - 2V_f(\lambda_m - \lambda_f)}{\lambda_f + 2\lambda_m + V_f(\lambda_m - \lambda_f)}$$

where λ_c, λ_m and λ_f are the effective thermal conductivities of the composite, PEEK matrix, and filler particles, respectively, and V_f is the filler volume fraction. These calculations used λ_m = 0.26 W/mK, the measured value for PEEK, and assumed λ_f = 2000 W/mK [42] for the ND filler. Weight fractions were converted into volume fractions assuming 1.3 and 3.15 for the densities of PEEK and ND, respectively. The predicted values of composite thermal conductivity increase monotonically with son-OND loading (Figure 3.39), but they are much lower than the experimental values for of son-OND/PEEK composites.

The increase in composite thermal conductivity at 1% and 3% son-OND loadings are consistent with the trend predicted by the Maxwell model, but the decrease at 5% son-OND is not. This decrease could be attributed to son-OND agglomeration or relatively poor dispersion. This explanation is supported by the nSPEC surface topography results shown in Figures 3.6 and 3.8. Incomplete dispersion or agglomeration of OND may result in increased interfacial thermal resistance between aggregated ND particles and lower thermal conductivity values.

Figure 3.40 compares the thermal conductivities of PEEK and various 3 wt% ND/PEEK composites. The 3% OND/PEEK and 3% CND/PEEK composites have similar thermal conductivity values. The 3% OND/PEEK has 7% higher thermal conductivity than PEEK (94% confidence), while 3% CND/PEEK has 12% higher thermal conductivity than PEEK (88% confidence). The 3% son-OND/PEEK composite clearly has a much higher thermal conductivity (by 29%) than that made with PPA-modified OND prepared

without sonication. Results in Table 2.4 (Chapter 2, [77]) show that sonication during PPA grafting onto OND results in superior ND dispersion in organic solvents. This suggests that sonication during PPA grafting onto OND may also improve OND dispersion in hydrophobic PEEK. This would increase the amount of OND/PEEK interfacial area, which may have lower interfacial resistivity than OND-OND interfaces in particle agglomerates.

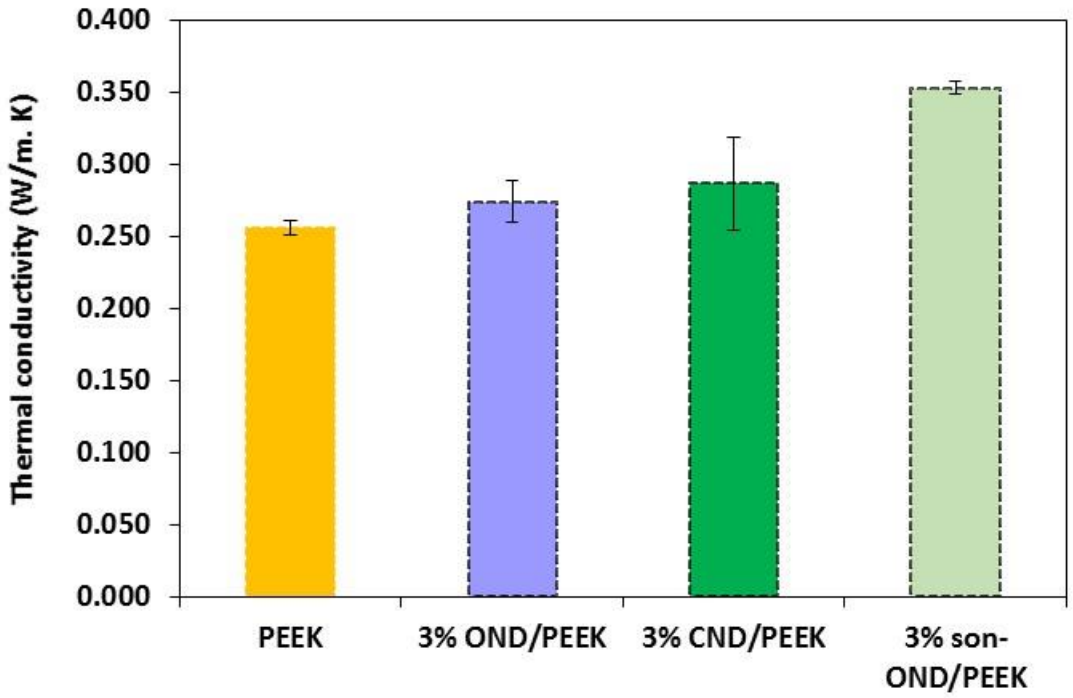

Figure 3.40. Thermal conductivity of PEEK and various 3 wt% ND/PEEK composites.

Considering the exceptionally high thermal conductivity of ND (~2000 W/mK, [42], the enhanced thermal conductivity values of son-OND/PEEK composites seem plausible. Previous studies [42, 45, 49] where ND was used as a filler in different

polymer matrices have also reported comparable enhancement of thermal conductivity values.

3.4.5 Dielectric Properties

Dielectric (impedance) spectroscopy and polarization testing were used to characterize the dielectric properties of PEEK and ND/PEEK composites. Figure 3.41 shows the frequency-dependent dielectric constant for PEEK and son-OND/PEEK composites with varying son-OND loading. The dielectric constant of pure PEEK has a value between 4.0 and 4.2 and nearly independent of frequency above 1 kHz. This value is consistent with past studies [87] for thermally annealed PEEK. The dielectric constant for 1% son-OND/PEEK varies between 3.9 and 3.4 over the measured frequency range. The reason for the frequency dependence of the dielectric constant of this composite is not clear. The presence of an ionic contaminant may result in charge migration and energy dissipation; we will return to this point below. The key result is that the 1% son-OND/PEEK composite has a dielectric constant that is 10 to 15 % lower than that of pure PEEK.

The 3% son-OND/PEEK composite has a dielectric constant of about 3.7 that is nearly independent of frequency. This value is lower than that of pure PEEK but does not differ significantly from the dielectric constant of 1% son-OND/PEEK. For the 5% son-OND/PEEK composite, the dielectric constant value rises to about 4.0, again nearly independent of frequency, but not significantly different than the dielectric constant of pure PEEK. The increase in dielectric constant with increasing son-OND loading may be

explained by the roughness of the composite surface (Figures 3.6 and 3.8). Figure 3.8 shows that the 5% son-OND/PEEK composite has a surface asperity density much higher than that of the other son-OND/PEEK composites. The higher asperity density results in a higher effective sample surface area compared to the nominal surface area used to calculate the dielectric constant from the measured sample capacitance.

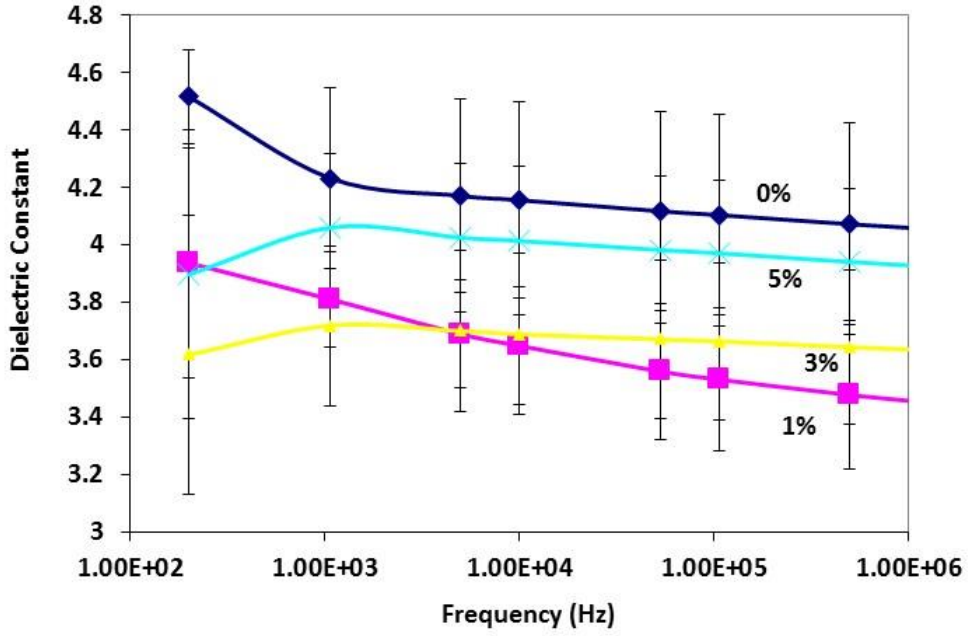

Figure 3.41. Dielectric constant versus frequency for pure PEEK (0%) and son-OND/PEEK composites with varying son-OND loading (wt%).

The data clearly show lower dielectric constants for 1% and 3% son-OND/PEEK composites relative to that for pure PEEK. The reduction in dielectric constant may be attributed to the reportedly low dielectric constant of the ND filler [88] as well as restriction of the mobility of polarizable groups in the PEEK through interactions with the ND [89]. Similar observations have been made for

silica/polyacrylamide [89] and phenyltrimethoxysilane-treated nano-silica/PEEK nanocomposites [2].

Figure 3.42 shows the frequency-dependent loss tangent (tan δ) for PEEK and son-OND/PEEK composites with varying son-OND loading. In general, pure PEEK, 3% son-OND/PEEK, and 5% son-OND/PEEK composites have loss tangents below 1% and independent of frequency above 1.0 kHz. The greater loss tangent values at low frequency may be due to dielectric loss in the PEEK matrix, possibly associated with local molecular motion of polarizable groups in PEEK. The loss tangent for 1% son-OND/PEEK composite has larger values at all frequencies and a peak value near 1.0 kHz. This supports the view that this composite contains an ionic contaminant that migrates in response to the applied electric field, resulting in energy dissipation. Additional evidence comes from the measured specific conductivity (Figure 3.43). This data shows that the 1% son-OND/PEEK composite has a higher specific conductivity than pure PEEK at all frequencies, whereas the other composites have conductivities similar to or lower than PEEK.

Figure 3.44 compares the frequency-dependent dielectric constants of pure PEEK with various ND/PEEK composites (all with 3% ND loading). For all materials, the dielectric constants are essentially independent of frequency above 1.0 kHz. Within experimental error, we observe no difference in the dielectric constants of 3% son-OND/PEEK and 3% OND/PEEK composites. Thus sonication during PPA grafting on OND appears to have no impact on dielectric properties, even if it does improve OND particle

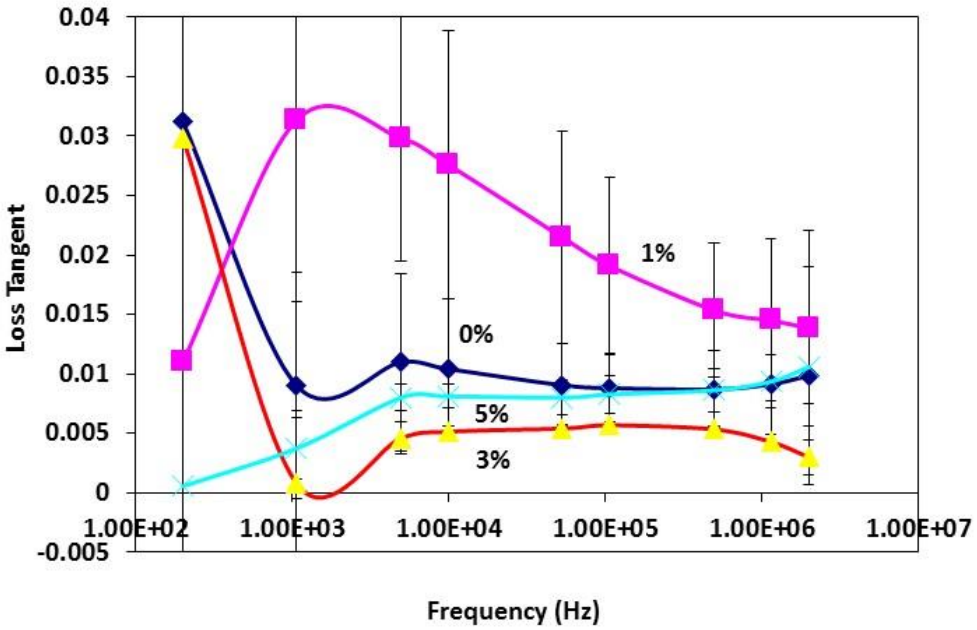

Figure 3.42. Loss tangent (tan δ) versus frequency for pure PEEK (0%) and son-OND/PEEK composites with varying son-OND loading (wt%).

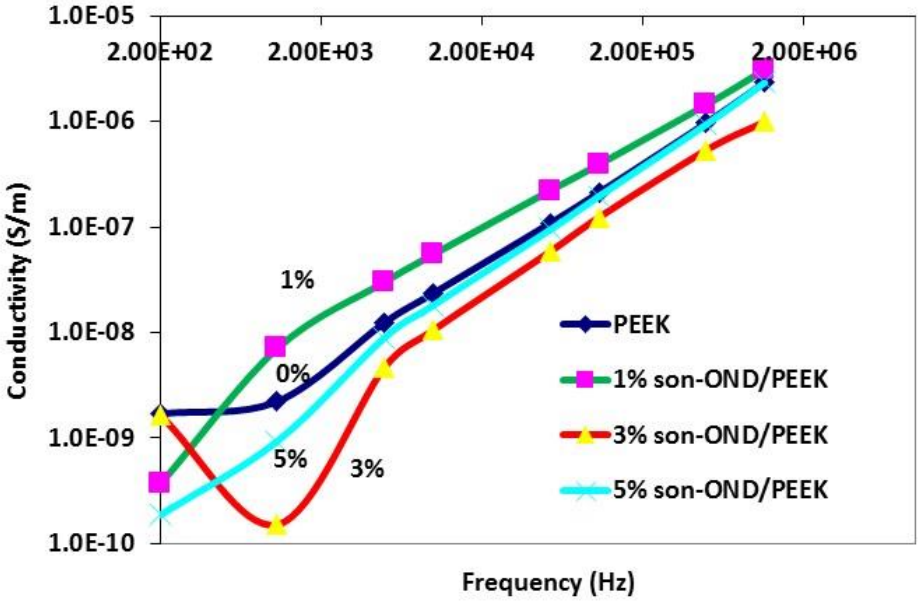

Figure 3.43. Specific conductivity versus frequency for pure PEEK (0%) and son-OND/PEEK composites with varying son-OND loading (wt%).

dispersion in PEEK. This result also shows the reproducibility of the dielectric measurement, since both composites are essentially 3% OND in PEEK.

Figure 3.44 also indicates essentially no difference in the dielectric constants of 3% CND/PEEK and pure PEEK. The same factors could be at play here as in the 5% son-OND/PEEK composite. Considering the 3 wt% loading of ND, one might expect the dielectric constant of 3% CND/PEEK to be similar to that of the two 3% OND/PEEK composites. However, Figure 3.8 indicates that the surface of the 3% CND/PEEK composite has a high asperity density, comparable to that of the 5% son-OND/PEEK composite. These two composites may have large "effective" surface areas, much larger than the nominal sample surface area, which would result in higher-than-expected dielectric constant values when these are computed from the measured sample capacitances. This may explain why 3% CND/PEEK has an apparent dielectric constant comparable to that of pure PEEK.

The loss tangent values for all of the 3% ND/PEEK composites (Figure 3.45) are all below about 1.5% and independent of frequency above 1.0 kHz. Below 1.0 kHz, PEEK and both 3% OND/PEEK composites manifest higher loss tangent values. Again we speculate that this may be due to dissipation arising from the local molecular motion of polarizable groups in PEEK. The loss tangent for the 3% son-OND/PEEK composite is much lower than that of 3% OND/PEEK above 1.0 kHz. This observation suggests that more complete and uniform grafting of PPA on OND, achieved through sonication, may play a role in mitigating dielectric loss in ND/PEEK composites. This observation also

suggests that the dielectric loss in ND/PEEK composites has an interfacial origin, at least at frequencies above 1.0 kHz.

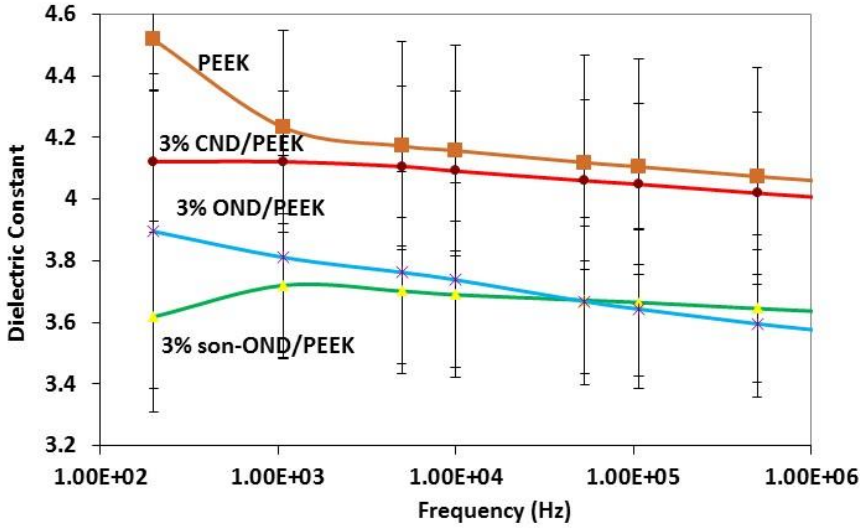

Figure 3.44. Dielectric constant versus frequency for pure PEEK (0%), 3% CND/PEEK, 3% OND/PEEK, and 3% son-OND/PEEK.

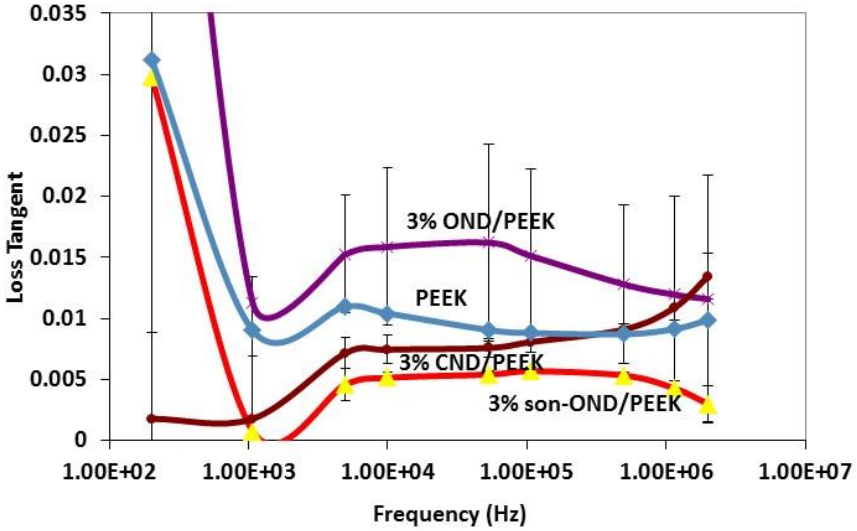

Figure 3.45. Loss tangent (tan δ) versus frequency for pure PEEK (0%), 3% CND/PEEK, 3% OND/PEEK, and 3% OND_{son}/PEEK.

Specific conductivity measurements (Figure 3.46) are consistent with the loss tangent results. The specific conductivity of 3% OND/PEEK is similar to that of pure PEEK, as is 3% CND/PEEK at frequencies greater than 1.0 kHz. However, the specific conductivity of the 3% son-OND/PEEK composite lies below those of the other composites and pure PEEK. Again, more complete and uniform grafting of PPA on OND, achieved through sonication, may reduce the role of charge conduction mechanisms at the ND/PEEK interface, thereby decreasing the composite's specific conductivity.

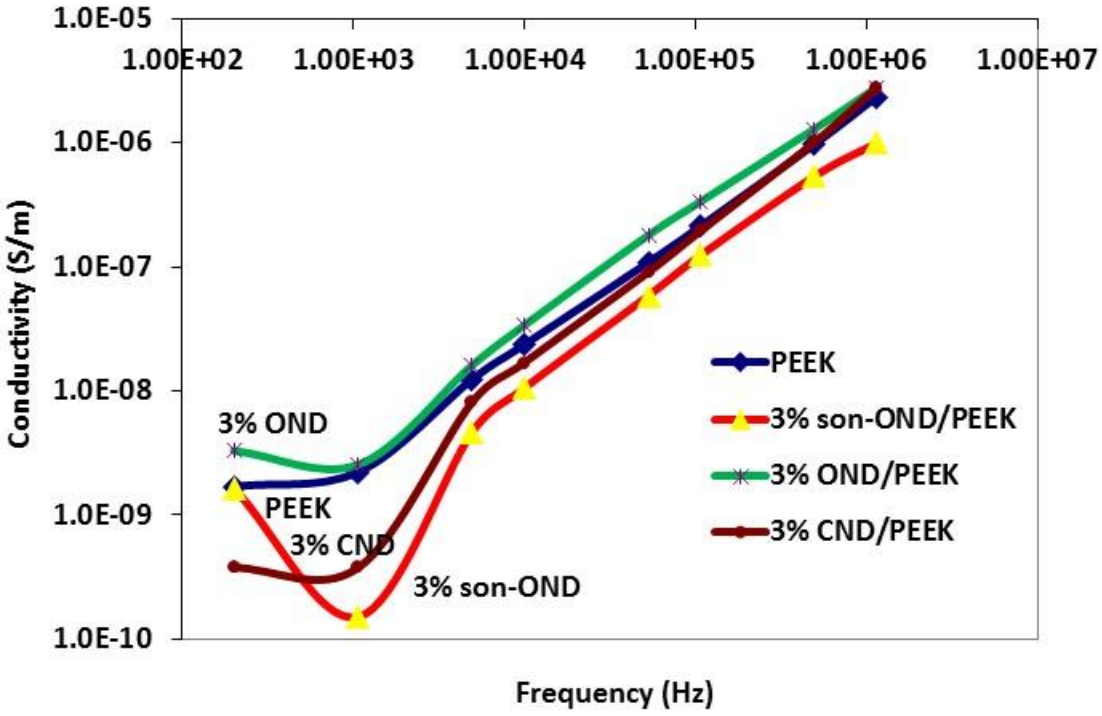

Figure 3.46. Specific conductivity versus frequency for pure PEEK (0%), 3% CND/PEEK, 3% OND/PEEK, and 3% son-OND/PEEK.

Polarization measurements (Figures 3.47 and 3.48) provide additional support for the mechanisms invoked to explain dielectric constant, loss tangent, and specific conductivity results. Figures 3.47 and 3.48 show dielectric displacement versus applied electric field curves (D-E loops) for pure PEEK and all ND/PEEK composites. All of the D-E loops have similar appearance: none of them are perfectly linear, and all manifest similar levels of hysteresis, as indicated by the areas enclosed by the D-E loops.

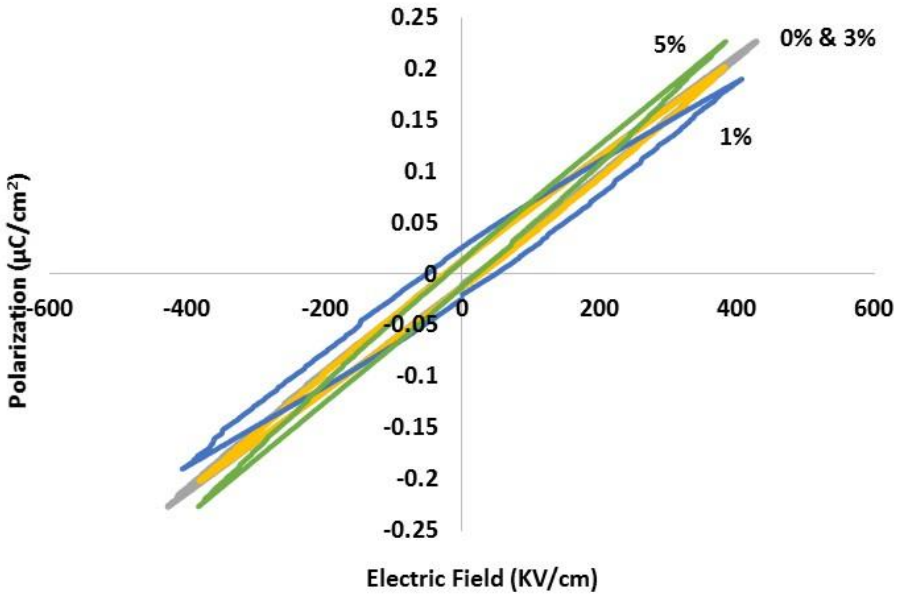

Figure 3.47. Dielectric displacement versus applied electric field for pure PEEK (0%) and son-OND/PEEK composites with varying son-OND loading (wt%).

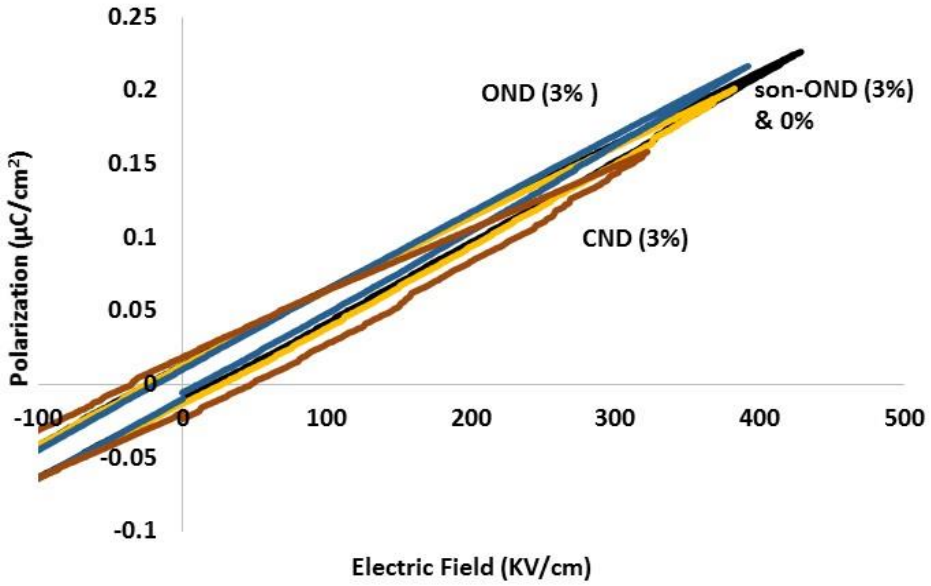

Figure 3.48. Dielectric displacement versus applied electric field for pure PEEK (0%), 3% CND/PEEK, 3% OND/PEEK, and 3% son-OND/PEEK.

A few points are noteworthy. First, pure PEEK exhibits a hysteresis loop; this indicates the existence of a dissipation mechanism in the polymer itself. The mechanism may involve field-induced motion of the polarizable groups in PEEK, resulting in dissipation of electrical energy as heat. All of the ND/PEEK composites have similar D-E loops because dissipation occurs in the PEEK matrix in all of the materials. The second point is that the D-E loop for the 1% son-OND/PEEK composite (Figure 3.47) has a larger hysteresis loop area than PEEK or the other composites. This observation is consistent with the speculation that 1% son-OND/PEEK contains an ionic contaminant that migrates in the applied field, resulting in additional dissipation. Finally, the 3% CND/PEEK composite appears to have a relatively large hysteresis loop area (Figure

3.48). This composite did not exhibit a large loss tangent in dielectric spectroscopy measurements (Figure 3.45). Nonetheless, we know that this particular ND material has a lower PPA graft density (Table 2.4) than the PPA-modified OND. The lower PPA graft density, and/or the more polar CND surface, may facilitate higher rate of surface charge conduction when subjected to the much higher applied electric fields in the polarization measurements.

3.5 Conclusions

Our preliminary effort to produce ND/PEEK composites with as-received ND from Nanoblox had poor dispersion in PEEK and inferior mechanical properties. Having demonstrated successful grafting of PPA on to CND and OND (Chapter 2), this work continued with melt-blending of PPA-modified OND or CND with PEEK, including PPA-modified OND that was sonicated during the grafting process.

Surface tomography results from nSpec® 3D suggest that both qualitatively and quantitavely, OND/PEEK samples has good dispersion in PEEK but the added sonication step during the PPA grafting process does not offer any added benefit during melt blending. nSpec® 3D results also suggest that CND/PEEK composite has inferior dispersion and possibly formed large aggregates in PEEK matrix. The results also show that with increased ND loading, a higher incidence of particle aggregation cam be observed in son-OND/PEEK composites.

WAXS patterns show that all of the ND/PEEK composites have the same peaks as seen in the pure PEEK polymer. However, the peaks in the ND/PEEK patterns are shifted

to somewhat larger values of 2θ, suggesting slight contraction of the unit cell dimensions. Mostly small variations in unit cell dimensions among the samples were found, although there are definitive changes. MAXS results show that the scattered intensities for the ND/PEEK composites are significantly greater than that for pure PEEK at all q values below q~0.25 $Å^{-1}$. Also the peak in I(q) for PEEK becomes considerably broadened in the ND/PEEK profiles. Lorentz-corrected MAXS patterns for pure PEEK and ND/PEEK composites show a peak in $q^2I(q)$ at approximately q=0.04 $Å^{-1}$. corresponding to a long-period lamellar spacing of about 16 nm. This result shows that the addition of PPA-modified OND to PEEK does not change the lamellar structure of the PEEK.

Tensile testing and DMA results show that the extra sonication step either helped retaining or increasing the modulus of PEEK matrix. Tensile strength on the other hand either decreased or stayed the same as PEEK with the sacrifice of reduced ductility. Based on the loss tangent results of DMA, ND addition caused very little or no change in the glass transition temperature of the composites.

DSC results show that the peak temperatures of crystallization exotherms for all of the ND/PEEK composites are approximately 4-5°C lower than those of pure PEEK indicating a delayed crystallization. DSC results also suggest that the PPA-modified CND inhibits PEEK crystallization while the PPA-modified OND may enhance PEEK crystallization, or at least does not inhibit it.

The isothermal TGA data indicates that, irrespective of surface modification or ND content, all ND/PEEK composites have excellent thermal stability at PEEK processing

temperature for at least 60 minutes. Dynamic TGA both in air and nitrogen show that, beyond 500°C to 550°C, thermal stability of the ND/PEEK composites are affected due to the onset of thermal degradation of PPA.

Thermal conductivity results show that addition of OND or CND in general increases the thermal conductivity of ND/PEEK composite; the increase is much more significant when son-OND was added to the PEEK matrix. Thermal conductivity increased as much as 38% with increased filler loading. A decline in thermal conductivity was noticed for the 5% son-OND/PEEK composite, but it was still higher than pure PEEK.

Dielectric spectroscopy data shows that 1% son-OND/PEEK composite has a dielectric constant that is 10 to 15 % lower than pure PEEK. Dielectric constant of son-OND/PEEK composite increases with increased son-OND loading, possibly due to higher effective surface area caused by increased roughness. The dielectric data also show that pure PEEK, 3% son-OND/PEEK, and 5% son-OND/PEEK composites have loss tangents below 1% and independent of frequency above 1.0 kHz. 1% son-OND/PEEK composite has higher loss tangent and higher specific conductivity at all frequencies. Both of these results indicate the presence of an ionic contaminant in this sample that may have resulted in charge migration and energy dissipation.

Dielectric polarization results show that pure PEEK as well as all of the ND/PEEK composites have similar D-E loops. The D-E loop for the 1% son-OND/PEEK composite has a larger hysteresis loop area than PEEK or the other composites, possibly due to the presence of an ionic contaminant previously mentioned. Also the 3% CND/PEEK

composite appears to have a relatively large hysteresis loop area. The lower PPA graft density, and/or the more polar CND surface could be responsible for this observation.

CHAPTER 4

GRAFTING OF HYDROXYLATED POLY(ETHER ETHER KETONE) TO THE SURFACE OF NANODIAMOND

4.1 Introduction

One of PEEK's primary properties is its high chemical resistivity towards most organic solvents. This property makes it an excellent choice for many critical applications in automobile, aerospace, medical and electronic industries. Unfortunately, this same property makes it very difficult to functionalize and creates unfavorable interactions with other substances such as fillers.

To overcome this disadvantage and promote compatibility between composite phases, one approach is to employ a "compatibilizer", a polymer derivative with functional groups having affinity for both the filler and the polymer matrix. To this end, previous research [4] has explored chemical modification of PEEK to synthesize PEEK-based compatibilizers. The aromatic rings in the PEEK structure are good targets for chemical modification, since they provide electrons for electrophilic substitution reactions. Furthermore, the ketone group in the benzophenone segment is also a versatile reactive handle for selective modifications of this polymer [90]. Treatment of

filler particles with such modified polymers could lead to PEEK nanocomposites with superior mechanical, thermal and electrical properties.

Another approach to increase nanoparticle dispersion quality in a polymer matrix is to use a small amount of a second polymer or polymeric surfactant that can act as a compatibilizing agent to reduce interfacial tension and promote adhesion between the primary polymer matrix and the dispersed phase. The selection of the polymeric surfactant is based on its affinity for both the matrix and the nanofillers [4]. Compatibilizers such as polyetherimide (PEI), poly(bisphenol-A-ether sulfone) (PES) and poly(1-4-phenylene ether-ether sulfone) (PEES), being miscible with and structurally similar to PEEK, have been used as surfactants to incorporate carbon nanotubes (CNTs) into PEEK [8-10].

This chapter describes preliminary efforts using each of these two approaches to incorporate nanodiamond in PEEK. As before, the objective was to produce ND/PEEK composites with superior dispersion quality. In the first method, PEEK was first converted to hydroxylated PEEK (HPEEK) by carbonyl reduction, followed by an attempt to covalently graft HPEEK onto CND. In the second method, some initial experiments were performed on the use of PEES and PEI as surfactants to promote ND dispersion in PEEK.

4.2 Synthesis of HPEEK and Grafting onto CND

This method involves two reaction steps. First, hydroxylated PEEK (HPEEK or PEEK-OH) was synthesized with different degrees of chain modification by selective

carbonyl reduction of ketone to alcohol. The derivatives with a low degree of functionalization are expected to retain the exceptional thermal and mechanical properties of the parent PEEK. Simultaneously, HPEEK should exhibit increased hydrophilicity and number of reactive functional groups that can act as potential anchorage points for other molecules. In the second step, an attempt was made to covalently attach HPEEK onto the surface of carboxylic nanodiamond (CND), which possess carboxylic functional groups on its surface. These experiments were performed in collaboration with Yating Mao of USC Department of Chemical Engineering.

4.2.1 Materials and Experimental Method

4.2.1.1 Materials

The polymer (PEEK 450PF) in fine powder form was sourced from Victrex® plc. This standard viscosity, fine powder grade has the following physical characteristics: T_g = 143°C (onset), T_m = 343°C, density = 1.3 g/cm^3, melt viscosity = 350 Pa.s at 400°C, average particle size (D50) = 50 µm [78]. Carboxylic acid modified nanodiamond (CND) was purchased from NanoBlox, Inc. and used as received. BET measurements indicate a specific surface area of 327 m^2/g for CND (Chapter 2, [77]). PEEK was ground with a ball mill in order to diminish the particle size, vacuum dried at 120°C for 4 h, and stored in a dry environment. CND was also dried at the same conditions. Dimethylsulfoxide (DMSO, 99%) and dimethylformamide (DMF, 99%), obtained from Aldrich, were dried for a few days with a Merck 4 A molecular sieve. Sodium borohydride ($NaBH_4$), N,N-

dicyclohexylcarbodiimide (DCC, 99%) and 4-dimethylaminopyridine (DMAP, 99%) were also purchased from Aldrich and used without further purification.

4.2.1.2 Synthesis of HPEEK by Carbonyl Reduction

The synthesis of HPEEK was carried out by selective carbonyl reduction in $NaBH_4$ per the procedure described in the literature [91]. PEEK (12 g) was added added gradually over 5 min into a stirred solution of $NaBH_4$ (3.6 g) in DMSO (300 mL). The suspension was heated at 120°C for 20 h using a thermostat with ethylene glycol heating liquid. After cooling to room temperature, the suspension was filtered; the recovered solid was washed successively with ethanol, water, HCl; and the washed solid was dried at 80°C under vacuum.

4.2.1.3 Preparation of HPEEK@CND

The covalent grafting of HPEEK on CND was performed according to the procedure described in literature [11, 12]. In this method, the grafting was attempted through Steglich esterification reaction [92]. Carboxylated nanodiamond (CND) (500 mg) were dispersed in DMF (125 mL) by ultrasonication for 30 min. Separately, HPEEK (4.5 g) was suspended in DMF (125 mL) and maintained at 50°C for 24 h under gentle stirring. The polymer suspension was added to a solution of DCC (23.1 g, 112 mmol) and DMAP (1.7 g, 13.8 mmol) in DMF (250 mL). Then, both polymer and C-ND dispersions were mixed with sonication and stirring under nitrogen at 40°C for 68 h. The coagulation of the mixture was accomplished by adding the suspension into 3 L of anhydrous methanol

under vigorous stirring. The resulting solid product (HPEEK@CND) was filtered, washed with methanol, and dried at 50^0C under vacuum.

4.2.1.4 Characterization

Fourier transform infrared spectroscopy (FTIR) measurements utilized a Shimadzu FTIR-8400 spectrometer with a diffuse reflectance solid state attachment (Pike Technologies). Thermogravimetric analysis (TGA) data were obtained using a model Q600 TGA (TA Instruments). TGA samples were heated in N_2 from room temperature to 900°C using a heating rate of 10°C/min. Isothermal TGA tests were also performed in N_2 by heating the sample from room temperature to 370°C and then holding at this temperature for 60 min.

For NMR results, solid state ^{13}C CP-MAS spectra were collected on a Bruker Avance III-HD 500 MHz spectrometer fitted with a 1.9mm MAS probe. The spectra were collected at ambient temperature with sample rotation rate of 20 kHz. 2.0 ms contact time with linear ramping on the ^{1}H channel and 62.5kHz field on the ^{13}C channel were used for cross polarization. ^{1}H dipolar decoupling was performed with SPINAL64 modulation and 145kHz field strength. Free induction decays were collected with a 27 ms acquisition time over a 300 ppm spectra width with a relaxation delay of 1.5 s. The NMR tests were performed by Dr. Perry J. Pellechia of USC Department of Chemistry and Biochemistry.

4.2.2 Results and Discussion

4.2.2.1 Synthesis of HPEEK by Carbonyl Reduction

Figures 4.1 and 4.2 compare the ATR-FTIR spectra of PEEK and the derivative HPEEK to show the changes in the chemical structures resulting from the carbonyl reduction process. We may consider the C-C stretching band (1490 cm^{-1}) to be a reference: it has comparable intensity in both spectra, as expected. Comparing the intensity of the peak at 1650 cm^{-1} (C=O stretching), the intensity of this band is reduced significantly for HPEEK compared to PEEK. At the same time, a weak band appears in the HPEEK spectrum at 3670 cm^{-1}, attributed to the stretching vibration of isolated OH groups. These observations are in accord with previous studies [91]. Both of these spectral changes indicate conversion of the PEEK ketone groups to hydroxyls.

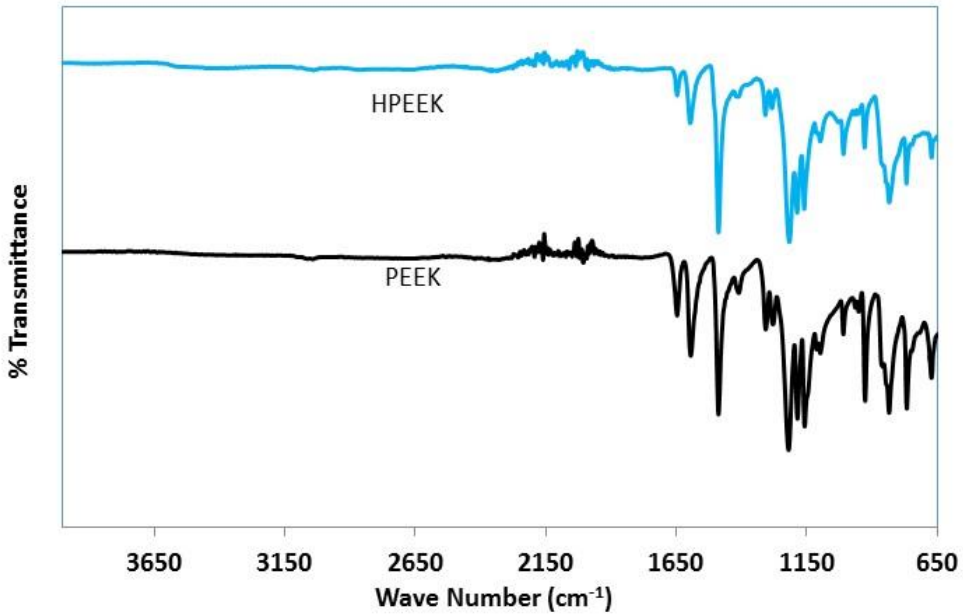

Figure 4.1. FTIR spectra of PEEK and HPEEK.

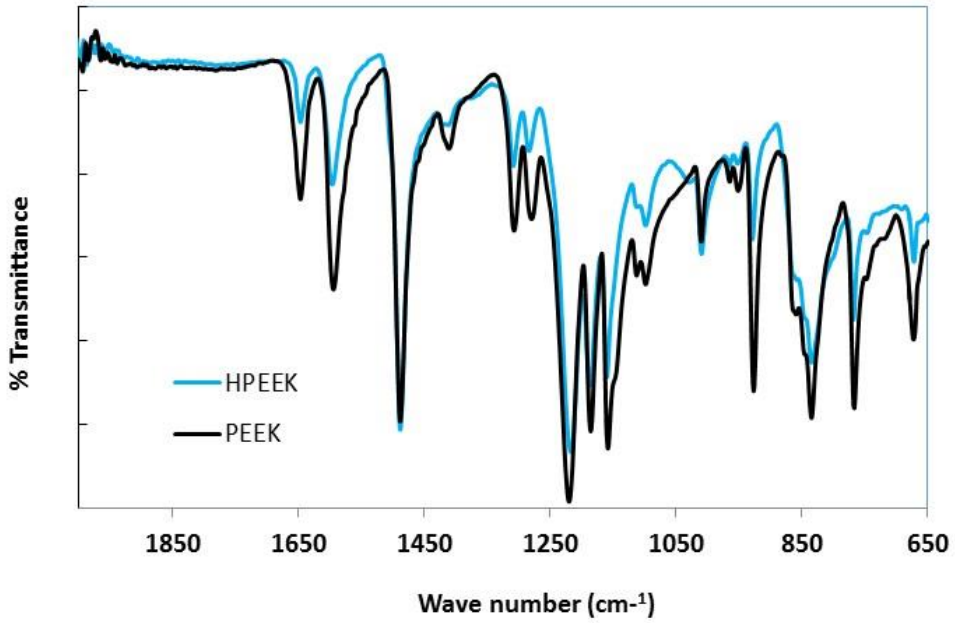

Figure 4.2. FTIR spectra of PEEK and HPEEK.

Figure 4.3 compares the solid-state ^{13}C-CP/Mass NMR spectra of PEEK and HPEEK to monitor the reduction of the ketone group from the benzophenone segment. The most intense signals appear in the spectral range between 110 and 165 ppm, associated with the carbons of the aromatic rings. In the HPEEK spectra, we observe a reduction of the peak intensity at around 193 ppm (associated with the carbon of the carbonyl group) and simultaneous appearance of a new signal at 75 ppm (associated with the carbon linked to the hydroxyl group). Thus the NMR results provide additional evidence of partial reduction of PEEK carbonyls to hydroxyls in HPEEK.

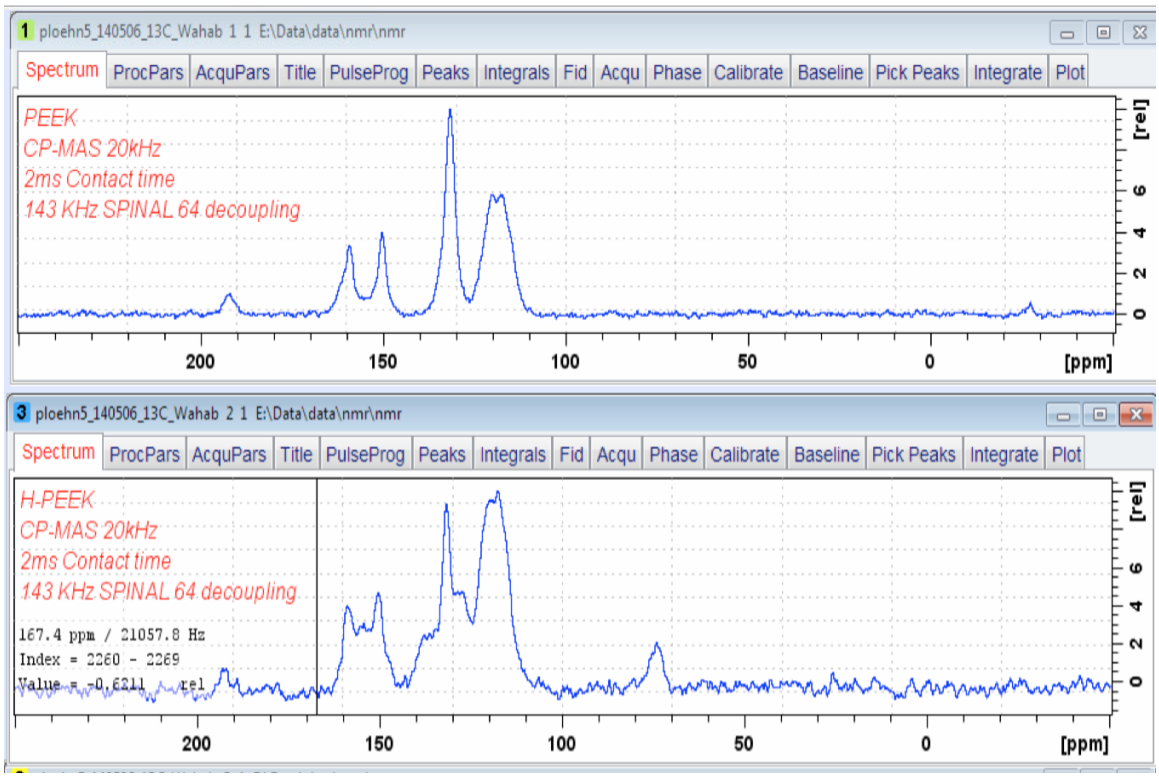

Figure 4.3. ^{13}C NMR spectra of PEEK (top) and HPEEK (bottom)

Figure 4.4 compares the thermal stability of PEEK and HPEEK by plotting the dynamic weight loss of the two samples in an inert atmosphere. The weight loss of the parent PEEK shows a relatively sharp onset of degradation at about 550°C, suggesting essentially a one step process. Literature suggests [91] that the degradation of PEEK's main chain involves decarboxylation, decarbonylation, and dehydration processes, leading to the formation of phenol groups, carbon dioxide, and water. The ether and aromatic structures remain in the residue until very high temperatures. For HPEEK, a small weight loss can be seen before 250°C, possibly due to the water loss. This occurs because HPEEK is more hydrophilic and absorbed some water at room temperature. At

higher temperatures, HPEEK appears to undergo two degradation stages. The first (250-400°C) can be attributed to the splitting-off of the –OH group, since this stage does not occur in the parent PEEK. The second degradation step above 450°C can be attributed to the decomposition of the main chain. The observations from FTIR, NMR and TGA results are similar to those reported by previous researchers [91].

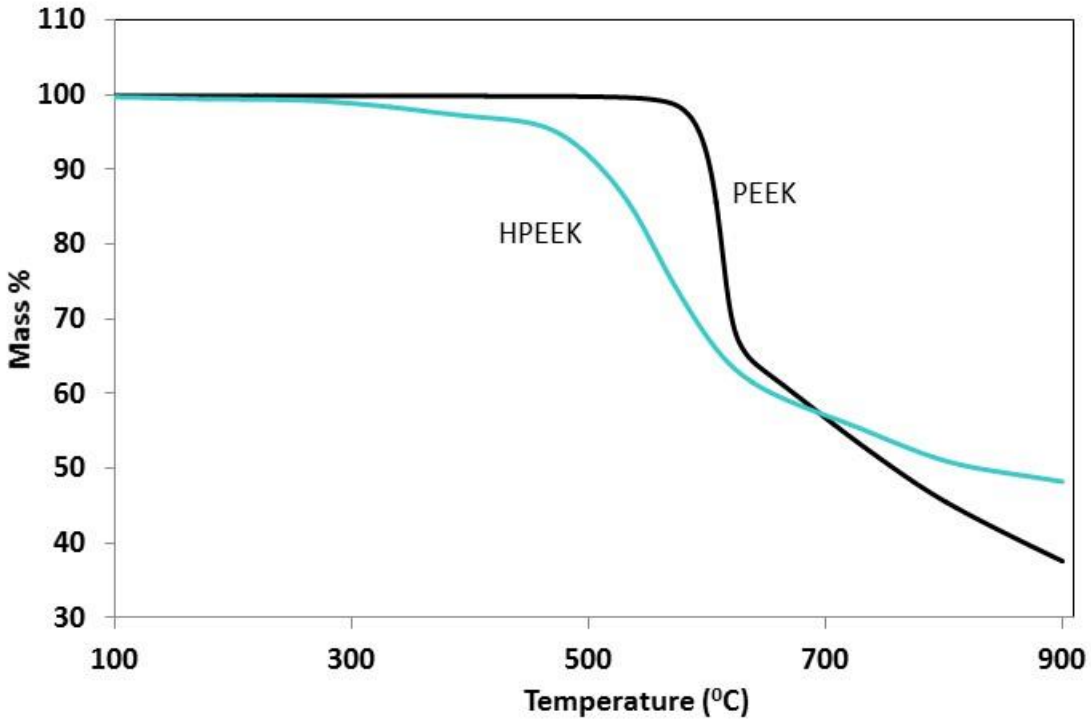

Figure 4.4. TGA characterization of mass percentage as a function of temperature for PEEK and HPEEK. Samples were heated in N_2 with a temperature ramp rate of 10°C/min.

4.2.2.2 Preparation of HPEEK@CND

In Steglich esterification, DCC reacts with carboxylic acid to form an intermediate (*O*-acylisourea). In the present work, DCC reacts with the carboxylic acid groups in CND. The activated CND is then expected to react with the –OH groups of HPEEK to form an

ester linkage with urea as a byproduct. The DMAP is added as a catalyst to accelerate the grafting reaction and avoid a side reaction [92]. Figure 4.5 compares the FTIR spectra of PEEK, HPEEK and the esterification reaction product HPEEK@CND. The spectra of HPEEK and HPEEK@CND seemed almost identical. According to literature, a peak at 1730-1738 cm^{-1} is an indication of the C=O stretching of an ester group [11]. This peak is not visible in our HPEEK@CND sample. As a result, at least based on the FTIR data, we cannot confirm that an esterification reaction has taken place.

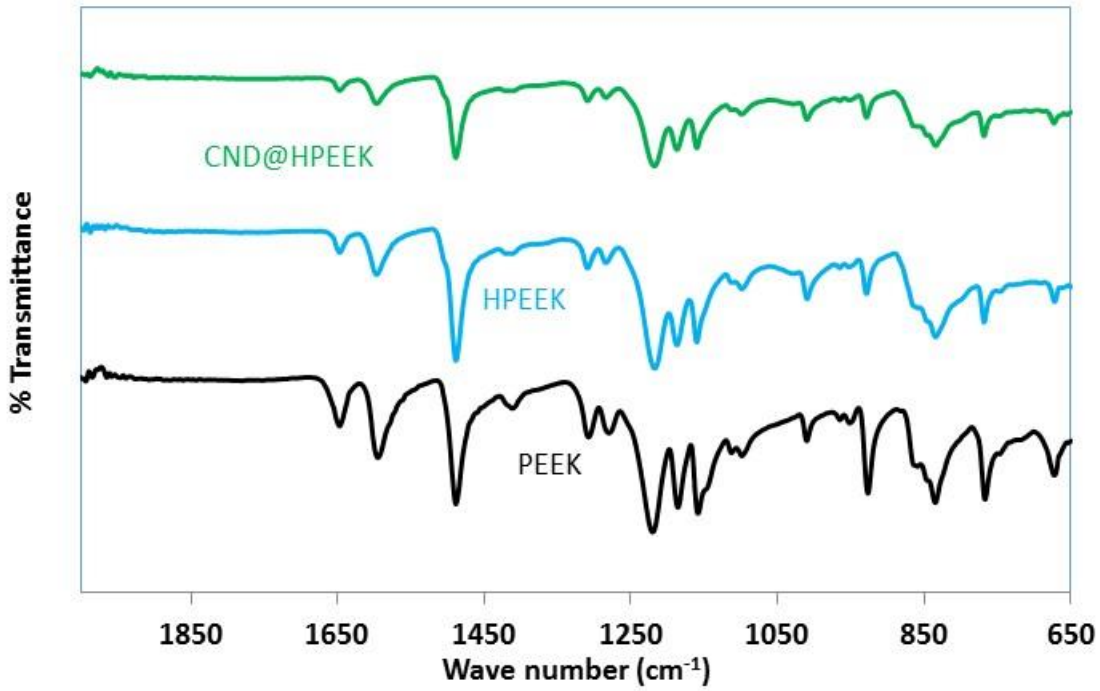

Figure 4.5. FTIR spectra of PEEK, HPEEK and HPEEK@CND.

Figure 4.6 compares the NMR spectra of PEEK, HPEEK and the HPEEK@CND. The NMR spectra of HPEEK and HPEEK@CND appear to be identical. The peak at 75 ppm

(associated with the carbon linked to the hydroxyl group) is visible for both HPEEK and HPEEK@CND, and the peak shape and intensity appear to be identical. A reduction of the intensity of this peak would have indicated the conversion of some of the –OH groups to ester. Also, a peak at about 177 ppm would have indicated the presence of a carbon of an ester group [11]. However, no such peak was noticed in the spectrum for HPEEK@CND.

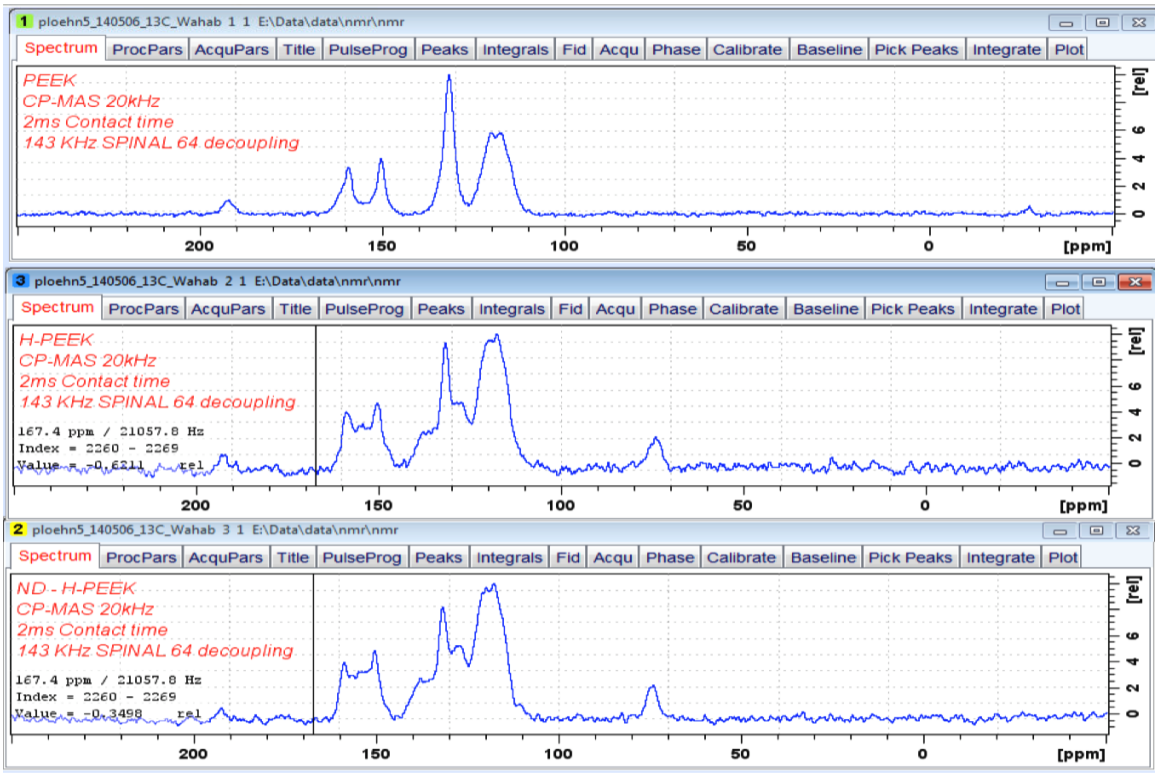

Figure 4.6. ^{13}C NMR spectra of PEEK (top), HPEEK (middle), and CND@HPEEK (bottom).

Figures 4.7 and 4.8 compare the dynamic and isothermal weight loss of PEEK, HPEEK, CND and HPEEK@CND as measured by TGA. As mentioned previously, HPEEK has less thermal stability than PEEK, as indicated by HPEEK's lower temperature for onset of degradation. CND loses some weight at lower temperature due to loss of absorbed

moisture, and then shows a gradual decomposition weight loss that accelerates above 500°C. Based on its formulation, HPEEK@CND contains about 10 wt% CND. The TGA weight loss results show that HPEEK@CND has intermediate thermal stability, that is, in between that of HPEEK and CND. The TGA results do not offer any evidence that confirms the grafting of HPEEK on CND.

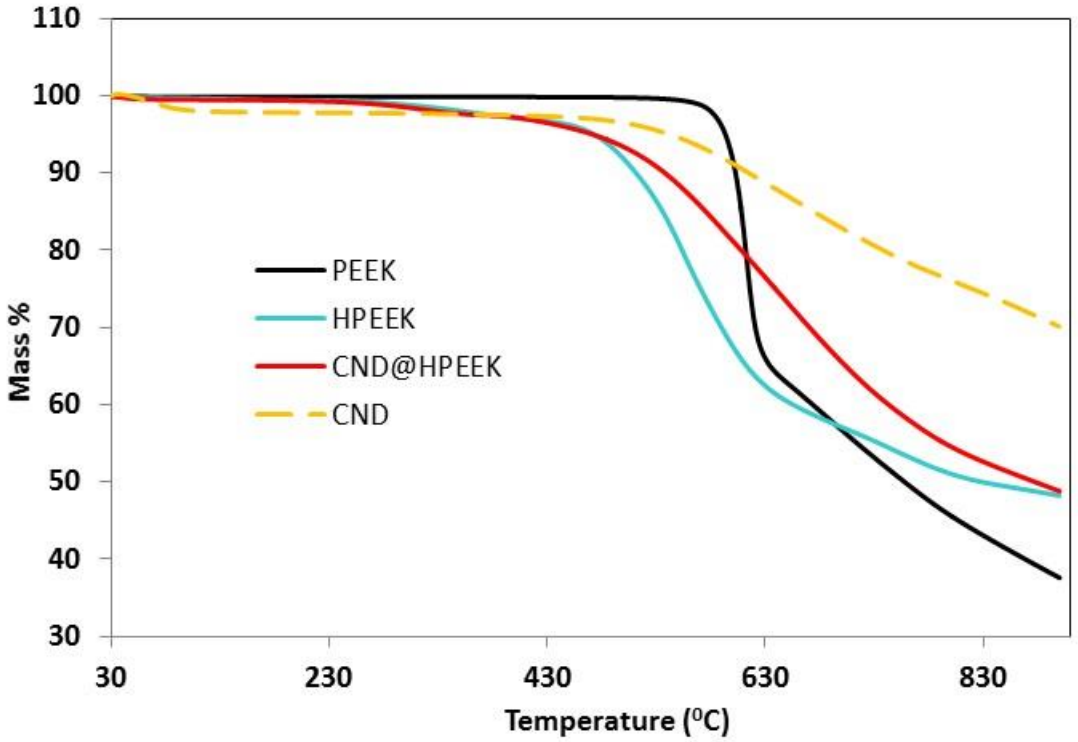

Figure 4.7. TGA characterization of mass percentage as a function of temperature for PEEK, HPEEK, CND@HPEEK and CND. All samples were heated in N_2 with a temperature ramp rate of 10°C/min.

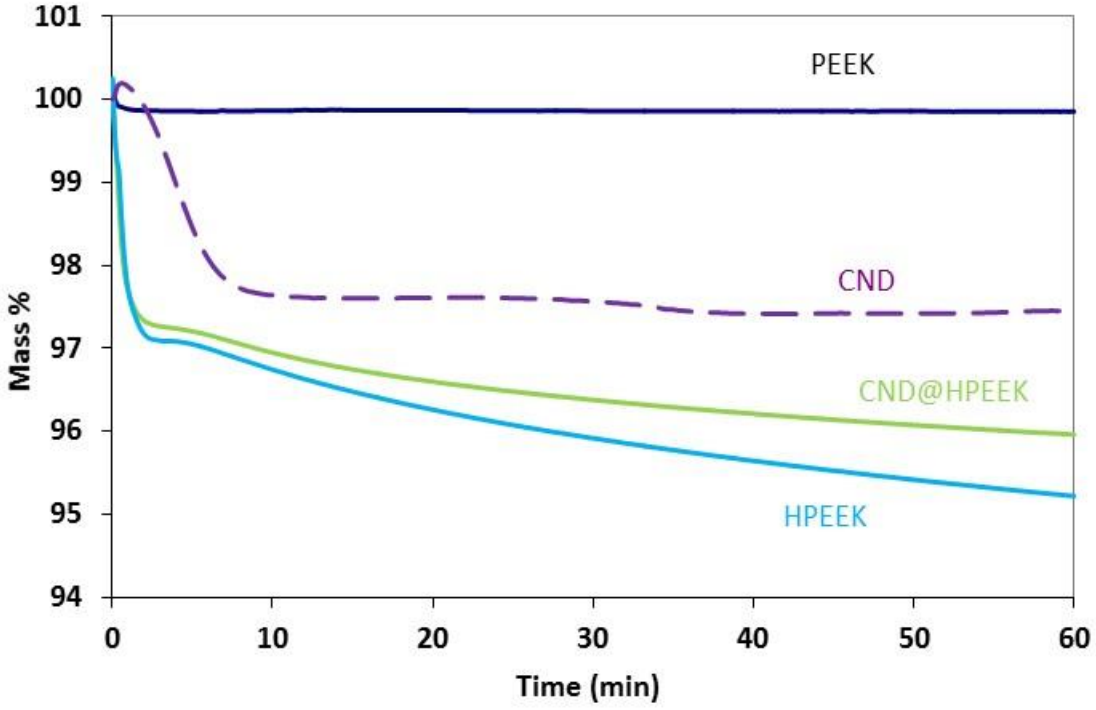

Figure 4.8. Isothermal TGA results for PEEK, CND, HPEEK@CND, and HPEEK. The temperature was ramped up to 370°C and held for 60 min in an N_2 atmosphere**.**

4.2.3. Conclusions

The FTIR and NMR results indicate that the carbonyl reduction reaction successfully converted PEEK to HPEEK. However, no evidence indicates that HPEEK was successfully grafted on CND to produce HPEEK@CND. The product HPEEK@CND is possibly just a blend of CND and HPEEK. The HPEEK@CND has higher thermal stability than HPEEK due to the contribution of more thermally stable CND. However, both HPEEK and HPEEK@CND have significantly reduced thermal stability compared with PEEK. The weight loss observed in the isothermal TGA data for HPEEK and HPEEK@CND

indicates that severe outgassing might be expected when these materials were to be compounded at standard PEEK processing temperatures.

4.3 Use of PEES and PEI as Compatibilizers for ND/PEEK Composites

4.3.1 Materials and Experimental Methods

4.3.1.1 Materials

The PEEK and CND used in this study are the same as those described previously. Polyetherimide (PEI; melt index 18g/10 min, at 337°C and 6.6 Kg load) was sourced from Sigma Aldrich in pellet form. Poly(1-4-phenylene ether-ether sulfone) (PEES) was also sourced from Sigma Aldrich in pellet form. Both PEI and PEES were dried at 120°C for 4 h and stored in a dry environment.

4.3.1.2 Dispersing CND in PEES and PEI

Dispersion of CND in PEI began with the preparation of a solution of PEI in chloroform (1.5% w/w). Then 370 mg of CND was dispersed in 25 mL of the PEI-chloroform solution with intense mixing at 50°C until complete dissolution of the PEI was observed. This mixture was sonicated with a sonic horn and then dried in a vacuum oven initially at room temperature overnight and then at 60°C overnight. The product mixture appeared to be uniform; no agglomerates could be observed visually. This method of mixing is similar to the methods reported by previous researchers [9]

For the PEES/CND blend, a 1.5% w/w solution of PEES in NMP (1-methyl-2-pyrrolidone) was first prepared. Then 370 mg of CND was dispersed in 25 mL of the

PEES-NMP solution with intense mixing at 50°C. This mixture was sonicated with a sonic horn and then dried in a vacuum oven at 80°C for several days. This method of mixing is similar to that reported by previous researchers [10]

4.3.1.3 Characterization

Isothermal TGA is one way to determine if a polymer blend can be processed at a desired temperature. Before proceeding to mix PEI-CND or PEES-CND with PEEK, TGA characterization was carried out to ensure that the solvents were driven off completely from the mixtures and to test their thermal stability under PEEK processing conditions.

Thermogravimetric analyses (TGA) were performed using a Mettler Toledo TGA/SDTA851. Isothermal TGA tests were performed in either air or N_2 by heating the sample from room temperature to a target hold temperature and then holding at this temperature for a specified time. Since the eventual plan for this project was to compound PEI-coated CND with PEEK, PEEK's usual processing temperature of 370°C was chosen as the hold temperature. Assuming that the materials' residence time in extrusion/compounding equipment could be as long as 60 min, the hold time was fixed at 60 min.

4.3.2 Results and Discussion

4.3.2.1 Thermal Stability of CND/PEI Blend

Figure 4.9 compares the isothermal TGA weight loss data for PEEK, PEI, CND, and PEI-coated CND in both at air and N_2. As expected, PEEK is quite thermally stable at its

processing temperature of 370°C. PEI has a small weight loss of about 0.25% after 25 min, possibly due to the presence of moisture absorbed by the PEI during the experimental setup. CND also exhibits a mass loss of about 2.5% after 15 minutes in both air and N_2, followed by no further weight loss for the remaining 45 min. Since CND is quite hydrophilic due to its surface chemistry and high surface area, this initial weight loss also can be attributed to moisture.

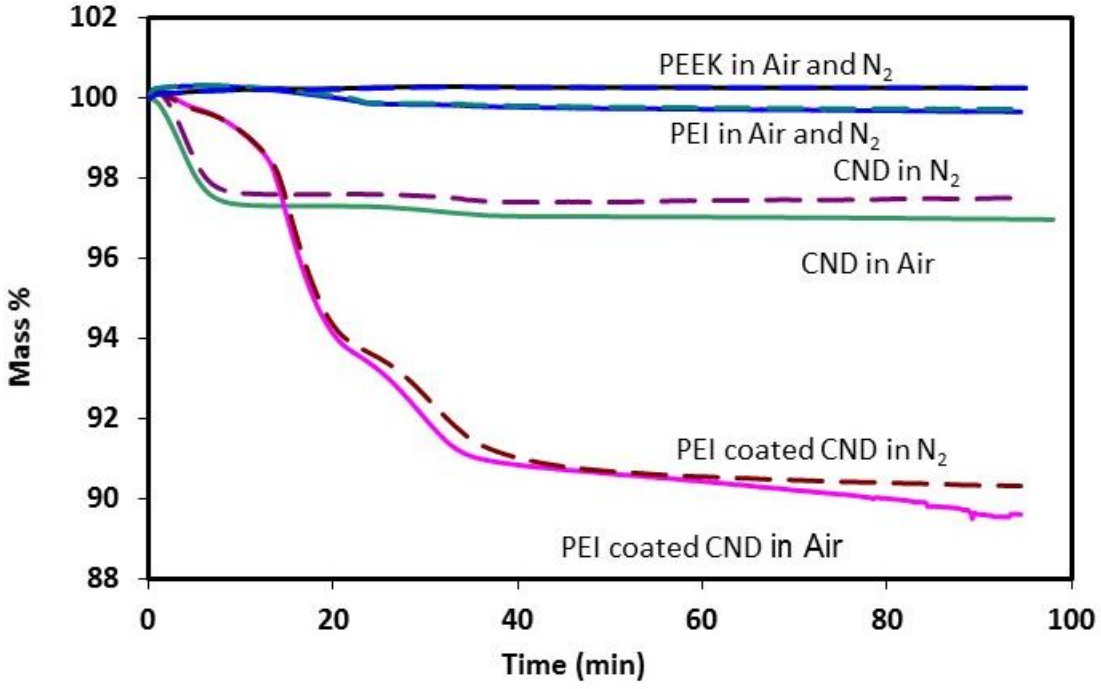

Figure 4.9. Isothermal TGA weight loss for PEEK, PEI, CND, and PEI-coated CND. The temperature was ramped to 370°C and held at this temperature for 60 min both in air and N_2.

The PEI-coated CND manifests significant weight loss of almost 10% over the first 35 min both in air and N_2 environments. After 35 minu, the mass of CND-PEI stabilizes in N_2 but continues to decrease at a slow rate in air. Since both PEI and CND are thermally

stable at 370°C, the significant weight loss observed for PEI-coated CND was not expected. It is possible that the chloroform used to dissolve PEI and mix with CND may not have completely evaporated, and that the material may need further solvent removal before proceeding with melt-blending with PEEK. Another less likely possibility is that the mixing and sonication procedure used for this experiment may have degraded the PEI, thereby rendering it less thermally stable. Gas chromatography or mass spectroscopy analysis of the off-gases could possibly identify if volatile is related to chloroform or PEI.

4.3.2.2 Thermal Stability of CND/PEES Blend

Isothermal TGA characterization was also performed on PEES-coated CND at the same conditions as the PEI-coated CND. The results were also found to be quite similar to those of the PEI-coated CND. Figure 4.10 shows that the PEES-coated CND undergoes a similar weight loss of 10-12% within the first 35 minutes before reaching a steady state. NMP was used as a solvent to dissolve PEES and to mix it with CND for this experiment. Since NMP has a high boiling point (~204°C), it was quite difficult to completely eliminate the solvent from the blend. It is possible that some NMP still remained in the blend after drying and then evaporated during the TGA test. Again, there is a small possibility that the mixing procedure somehow degraded the PEES, rendering it less thermally stable as a result.

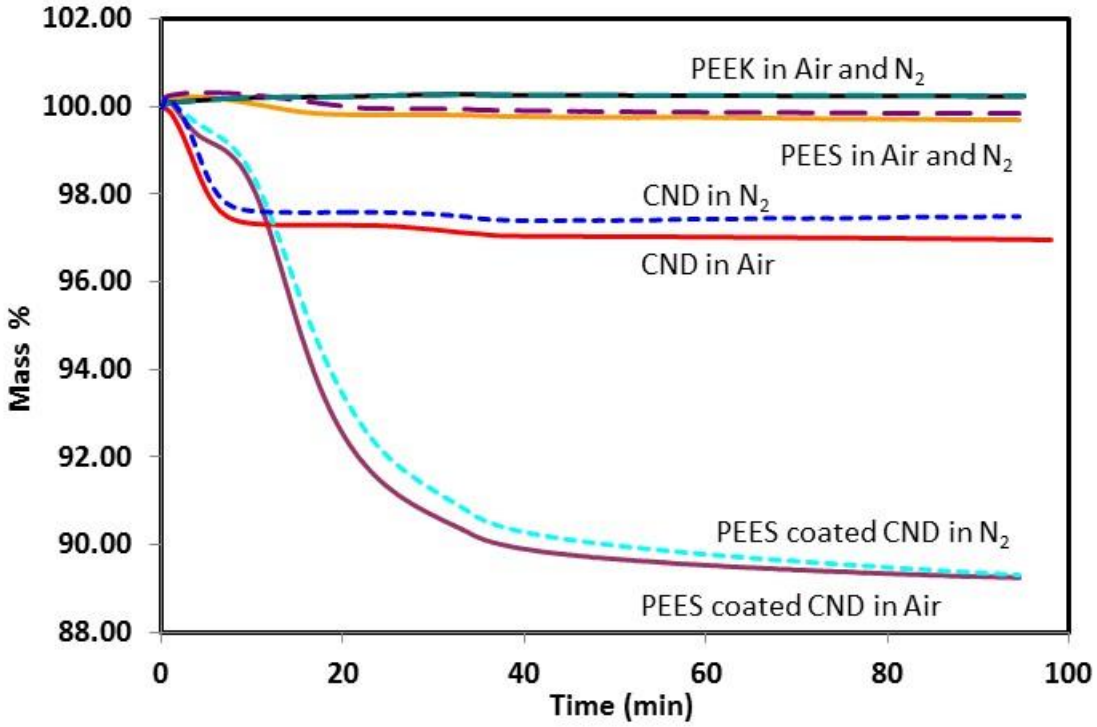

Figure 4.10. Isothermal TGA weight loss for PEEK, PEES, CND, and PEES-coated CND. The temperature was ramped to 370°C and held at this temperature for 60 min both in air and N_2.

4.3.3 Conclusions

TGA results suggests that both PEI-coated CND and PEES-coated CND are significantly less thermally stable than PEEK. This could be due to the presence residual solvents or the degradation of the material through the mixing procedure. It is expected that if such thermally unstable materials were blended with PEEK and then compounded at the standard PEEK processing temperature, severe outgassing could take place. Such outgassing could affect the blend quality and possibly be a safety issue. As a result, it

was decided not to proceed with any PEEK compounding experiments until reasons for the reduced thermal stability could be identified.

If the thermal stability issue could be overcome, new formulation work would be required to to produce thermally stable PEI- or PEES-coated CND materials. Materials that are thermally stable at the PEEK processing temperature can then be compounded with PEEK to produce the CND/PEEK composites. Such efforts were not possible due to time constraints.

REFERENCES

1. Y. Hwang, M. Kim, J. Kim, Composites: Part A 55 (2013) 195.

2. R.K. Goyal, A.S. Kapadia, Composites: Part B 50 (2013) 135.

3. M. Dwivedi, S. Alam, Sarfaraz, A, G.L. Verma, Polymer-Plastics Technology and Engineering 44 (2005) 1235.

4. A.M. Diez-Pascual, M. Naffakh, C. Marco, G. Ellis, M.A. Gomez-Fatou, Progress in Materials Science 57 (2012) 1106.

5. J. Sandler, A.H. Windle, P. Werner, V. Altstadt, M.V. Es, M.S.P. Shaffer, J. Mater. Sci. 38 (2003) 2135.

6. D.S. Bangarusampath, H. Ruckdaschel, V. Altstadt, J.K.W. Sandler, D.Garray, M.S.P. Shaffer, Polymer 50 (2009), 5803.

7. A.M. Diez-Pascual, M. Naffakh, C. Marco, G. Ellis, M.A. Gomez-Fatou, Prog. Mater. Sci. 57 (2012) 1106.

8. S. Zhang, H. Wang, G. Wang, Z. Jiang, App. Phys. Letter 101 (2012) 012904-1.

9. A.M. Diez-Pascual, M. Naffakh, M.A. Gomez, C. Marco, G. Ellis, J.M. Gonzalez-Dominguez, A. Anson, M.T. Martinez, Y. Martinez -Rubi, B. Simard, B. Ashrafi, Nanotechnology 20 (2009) 315707.

10. A.M. Diez-Pascual, M. Naffakh, J.M. Gonzalez-Dominguez, A. Anson, Y. Martinez –Rubi, M.T. Martinez, B. Simard, M.A. Gomez, Carbon 48 (2010) 3500.

11. A.M. Diez-Pascual, G. Martinez, J.M. Gonzalez-Dominguez, A. Anson, M.T. Martinez, M.A. Gomez, J. Mater. Chem. 20 (2010) 8285.

12. A.M. Diez-Pascual, G. Martinez, M.T. Martinez, M.A. Gomez, J. Mater. Chem. 20 (2010) 8247.

13. M. Dwivedi, S. Alam, G.L. Verma, J. Therm. Anal. Calor. 77 (2004) 947.

14. M. Dwivedi, S. Alam, G.L. Verma, Polym. Int. 54 (2005) 401.

15. M.C. Kuo, C.M.Tsai, J.C. Huang, M. Chen, Mater. Chem. Phys. 90 (2005) 185.

16. Y.H. Lai, M.C. Kuo, J.C. Huang, M. Chen, Mater. Sci. Eng. A. 458 (2007) 158.

17. L. Chang, Z. Zhang, L. Ye, K. Friedrich, Trib. Int. 40 (2007) 1170.

18. G. Zhang, A.K. Schlarb, S. Tria, O. Elkedim, Compos. Sci. Tech. 68 (2008) 3073.

19. R.K. Goyal, A.N. Tiwari, U.P. Mulik, Y.S. Negi, J. Nanosci. Nanotechnol, 9 (2009) 6902.

20. V.S. Nisa, S. Rajesh, K.P. Murali, V. Priyadarsini, S.N. Potty, R. Ratheesh, Compos. Sci. Tech. 68 (2008) 106.

21. V. Balaji, A.N. Tiwari, R.K. Goyal, Polym. Eng. Sci. (2011) 509.

22. T. Apeldorn, C. Keilholz, F. Wolff-Fabris, V. Altstadt, J. Appl. Polym. Sci. (2013) 3758.

23. V.V. Danilenko, Phys. Solid state 46 (2004), 595.

24. V.N. Mocohalin, O. Shenderova, D. Ho, Y. Gogotsi, Nature Nanotechnology 7 (2012), 11.

25. D.H. Wang, L-S. Tan, H. Huang, L. Dai, E. Osawa, Macromolecules 42 (2009), 114.

26. A. Krüger, F. Kataoka, M. Ozawa, T. Fujino, Y. Suzuki, A.E. Aleksenskii, A. Y. Vul, E. Osawa, Carbon 43 (2005), 1722.

27. A. Krueger, J. Mater.Chem 18 (2008), 1485.

28. E. Ōsawa, Diamond. Rel. Mater. 16 (2007), 2017.

29. E. Ōsawa, Pure Appl. Chem. 80 (2008), 1365.

30. Q. Xu, X. Zhao, J. Mater. Chem. 22 (2012), 16416.

31. T. Meinhardt, D. Lang, H. Dill, A. Krueger, Adv. Funct. Mater. 21 (2011), 494.

32. Y. Liang, M. Ozawa, A. Krueger, ACS Nano 3(8) (2009), 2288.

33. X. Xu, Z. Yu, Y. Zhu, B. Wang, Diamond. Rel. Mater. 14 (2005), 206.

34. Y. Liu, Z. Gu, J. L. Margrave, V. N. Khabashesku, Chem. Mater. 16 (2004), 3924.

35. A. Krüger, Y. Liang, G. Jarre, J. Stegk, J. Mater. Chem. 16 (2006), 2322.

36. O. Kuznetsov, Y. Sun, R. Thaner, A. Bratt, V. Shenoy, M. S. Wong, J. Jones, W. E. Billups, Langmuir 28 (2012), 5243.

37. W. S. Yeap, S. Chen, K. P. Loh, Langmuir 25 (2009), 185.

38. Y. Liang, T. Meinhardt, G. Jarre, M. Ozawa, P. Vrdoljak, A. Schöll, F. Reinert, A. Krueger, J. Colloid and Interface. Sci. 354 (2011), 23.

39. V.L. Kuznetsov, Y.V. Butenko, A.L. Chuvilin, A.I. Romanenko, A.V. Okotrub, Chem. Phys. Lett. 336 (2001) 397.

40. M. Bevilacqua, S. Patel, A. Chaudhary, H. Ye, R.B. Jackman, Appl. Phys. Lett. 93 (2008) 132115.

41. U. Maitra, K.E. Prasad, U. Ramamurty, C.N.R. Rao, Sol. Stat. Comm. 149 (2009) 1693.

42. S. Morimune, M. Kotera, T. Nishino, K. Goto, K. Hata, Macromolecules 44 (2011) 4415.

43. AY. Jee, M. Lee, Curr.Appl.Phys. 11 (2011) 1183.

44. AY. Jee, M. Lee, J. Nano. Nanotech. 11 (2011) 533.

45. I. Neitzel, V. Mochalin, I. Knoke, G.R. Palmese, Y. Gogotsi, Compos. Sci. Tech. 71 (2011) 710.

46. YJ. Zhai, ZC. Wang, W. Huang, JJ. Huang, YY. Wang, YQ. Zhao, Mater. Sci. Eng. A 528 (2011) 7295.

47. Q. Zhang, V.N. Mochalin, I. Neitzel, I.Y. Knoke, J. Han, C.A. Klug, J.G. Zhou, P.I. Lelkes, Y. Gogotsi, Biomaterials 32 (2011) 87.

48. YQ. Zhao, KT. Lau, JK. Kim, CL. Xu, DD. Zhao, HL. Li, Composites Part B: Engineering, 41 (2010) 646.

49. O. Shenderova, T. Tyler, G. Cunningham, M. Ray, J. Walsh, M. Casulli, S. Hens, G. Mcguire, V. Kuznetsov, S. Lipa, Diam. Rel. Mater. 16 (2007) 1213.

50. J.Y. Lee, D.S. Lim, Surf.Coat.Tech. 188-189 (2004) 534.

51. I. Kovalenko, D.G. Bucknall, G. Yushin, Adv. Funct. Mater. 20 (2010) 3979.

52. H. Hou, R. Polini, M.L.D. Vona, X. Liu, E. Sgreccia, JF. Chailan, P. Knauth, Int. J. Hydr. Ener. 38 (2013) 3346.

53. O. Shenderova, A. M. Panich, S. Moseenkov, S. C. Hens, V. Kuznetsov, H. M. Vieth, J. Phys. Chem. 115 (2011) 19005.

54. V. N. Mocohalin, Y. Gogotsi, J. Am. Chem. Soc. 131 (2009) 4594.

55. W. Gao, L. Dickinson, C. Grozinger, F. G. Morin, L. Reven, Langmuir 12 (1996) 6429.

56. P. H. Mutin, G. Guerrero, A. Vioux, J. Mater. Chem. 15 (2005) 3761.

57. S. E. Koh, K. D. McDonald, D. H. Holt, C. S. Dulcey, Langmuir 22 (2006) 6249.

58. P. Kim, S. C. Jones, P. J. Hotchkiss, J. N. Haddock, B. Kippelen, S. R. Marder, J. W. Perry, Adv. Mater. 19 (2007) 1001.

59. S. Shori, P.J. Pellechia, H. zur Loye, H.J. Ploehn, J. Colloid Interface Sci. 437 (2015) 97.

60. A. Krueger, Carbon Materials and Nanotechnology, Wiley-VCH: Weinheim, Germany, 2010.

61. H. Nijs, A. Clearfield, E. F. Vansant, Microporous Mesoporous Mater. 23 (1998) 97.

62. A. Shimada, Y. Yoneyama, S. Tahara, P. H. Mutin, Y. Sugahara, Chem. Mater. 21 (2009) 4155.

63. A. M. B. do Rego, A. M. Ferraria, J. El Beghdadi, F. Debontridder, P. Brogueira, R. Naaman, M. R. Vilar, Langmuir 21 (2005) 8765.

64. N. K. Mal, A. Bhaumik, M. Fujiwara, M. Matsukata, Microporous Mesoporous Mater. 93 (2006) 40.

65. J. Svoboda, V. Zima, L. Beneš, K. Melánová, M. Vlček, M. Trchová, J. Phys. Chem. Solids 69 (2008) 1439.

66. J. Randon, P. Blanc, R. Paterson, J. Membr. Sci. 98 (1995) 119.

67. S. Yagyu, M. Yoshitake, N. Tsud, T. Chikyow, Jpn. J. Appl. Phys. 50 (2011) 081606.

68. G. Guerrero, P. H. Mutin, A. Vioux, J. Mater. Chem. 11 (2001) 3161.

69. G. Guerrero, P. H. Mutin, A. Vioux, Chem. Mater. 13 (2001) 4367.

70. C. Breen, N. D'Mello, J. Yarwood, J. Mater. Chem. 12 (2002) 273.

71. E. Jaimez, A. Bortun, G. B. Hix, J. R. García, J. Rodríguez, R. C. T. Slade, J. Chem. Soc., Dalton Trans. (1996) 2285.

72. P. Persson, E. Laiti, L.-O. Öhman, J. Colloid Interface Sci. 190 (1997) 341.

73. W. O. Yah, A. Takahara, Y. M. Lvov, J. Am. Chem. Soc. 134 (2012) 1853.

74. L. D. Quin, A. J. Williams, Practical Interpretation of P-31 NMR Spectra and Computer Assisted Structure Verification, Advanced Chemistry Development, Inc.: Toronto, Canada, 2004.

75. O. Shenderova, A. M. Panich, S. Moseenkov, S. C. Hens, V. Kuznetsov, H. M. Vieth, J. Phys. Chem. 115 (2011) 19005.

76. T. Gaebel, C. Bradac, J. Chen, J.M. Say, L. Brown, P. Hemmer, J.R. Rabeau, Diamond Relat. Mater. 21 (2012) 28.

77. Z. Wahab, E.A. Foley, P.J. Pellechia, B.L. Anneaux, H.J. Ploehn, J. Colloid Interface Sci. 450 (2015) 301-309.

78. Victrex® 450PF data sheet

79. A. Tessema, A. Kidane, Compos. Hybr.Multi. Mat. 4 (2015) 151.

80. M. Islam, Ph.D. Dissertation, University of South Carolina, 2014.

81. J.N. Hay, J.L.Langford, J.R.Lloyd, Polymer 30 (1989) 489

82. R.K.Verma, V. Velikov, R.G.Kander, H. Marand, Polymer 37 (1996) 5357.

83. J. Wang, M. Alvarez, W. Zhang, Z. Wu, Y. Li, B. Chu, *Macromolecules*, 25 (1992) 6943.

84. F. Cser, J. App. Polym. Sci. 80 (2001) 2300.

85. M.C. Kuo, J.S. Kuo, M.H. Yang, J.C. Huang, Mater. Chem. Phys. 123 (2010) 471.

86. W. Jiajun, Y. Xiao-Su, Compos. Sci. Tech. 64 (2004) 1623.

87. M. Arous, I.B. Armor, A. Kallel, Z. Fakhfakh, G. Perrier, J. Phys. Chem. Sol. 68 (2007) 1405.

88. Carbodeon Ltd, Electronic Brochure.

89. A.A.F. Zikry, Int. J. Polym. Mat. 57 (2008) 383.

90. A.M. Diez-Pascual, G. Martinez, M.A. Gómez M. A, Macromolecules 42 (2009) 6885.

91. A.M. Diez-Pascual, G. Martinez, M.A. Gómez M. A, Macromolecules 42 (2009) 6885.

92. B. Neises, W. Steglich, Angew. Chem. Int. Ed. 17 (1978) 522.

APPENDIX A

SURFACE FUNCTIONALIZATION OF NANODIAMOND WITH PHENYLPHOSPHONATE

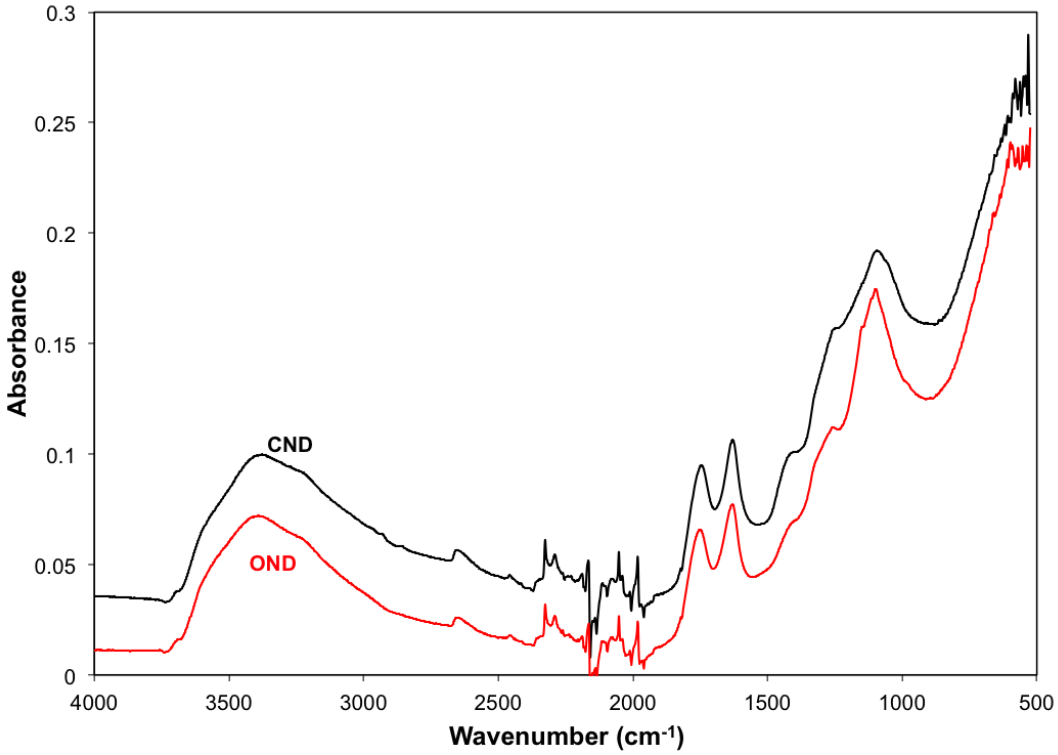

Figure A.1. FTIR spectra for OND and CND.

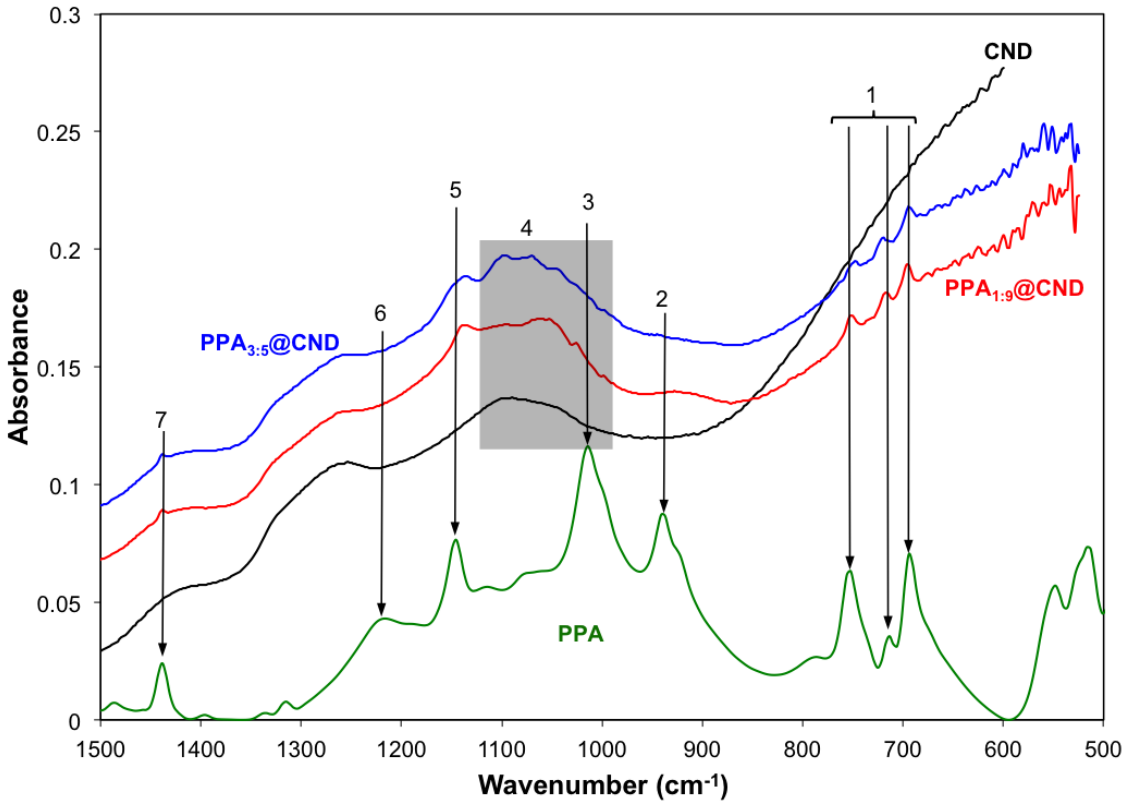

Figure A.2. FTIR spectra for PPA, CND, and PPA@CND products.

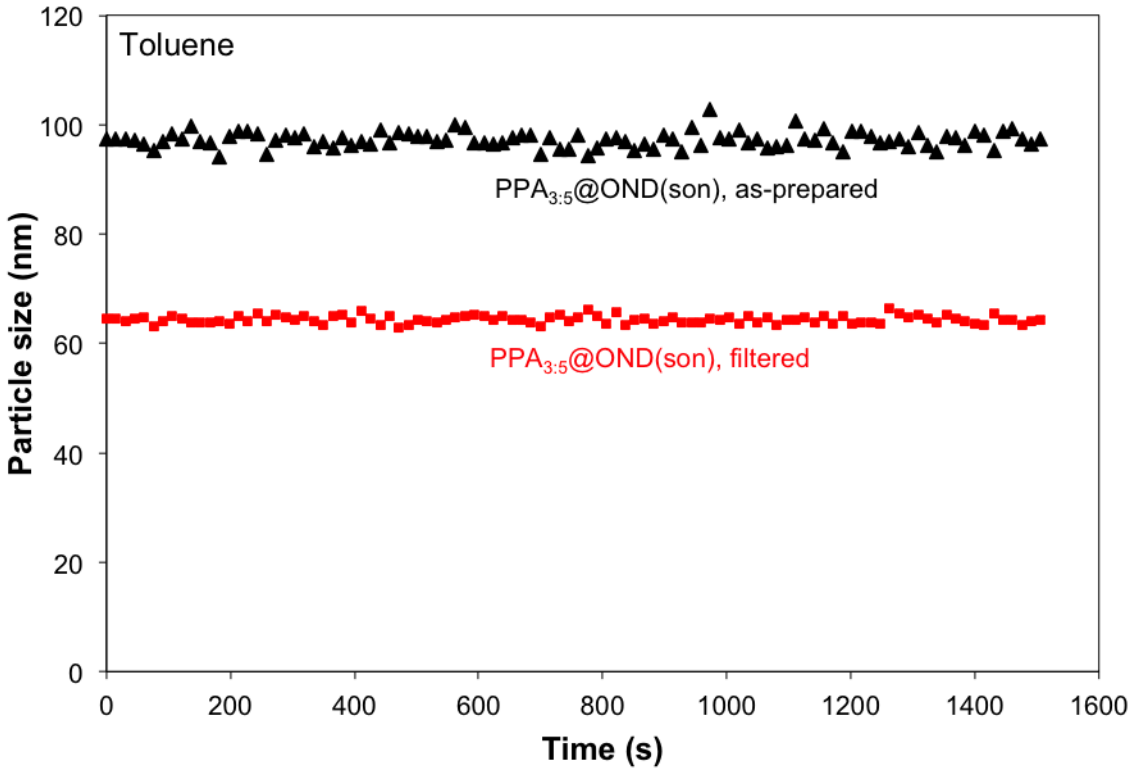

Figure A.3. DLS measurements of particle size as a function of time for $PPA_{3:5}$@OND prepared with sonication, dispersed in toluene. Filtration state (as-prepared or filtered) is indicated on the plot.

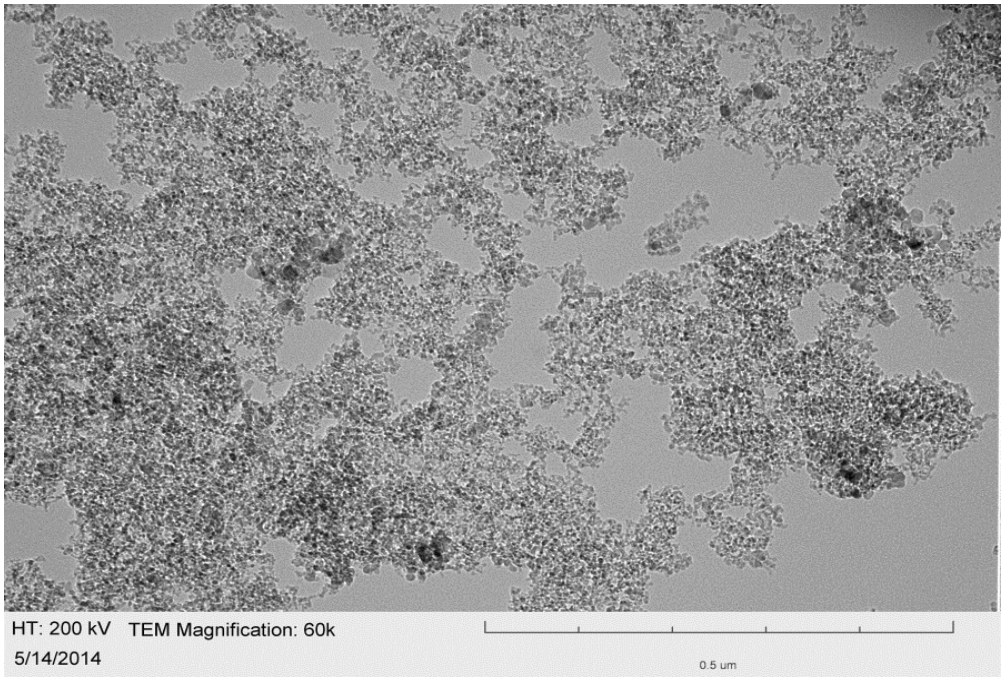

Figure A.4. TEM images of $PPA_{3:5}$@OND prepared with sonication.

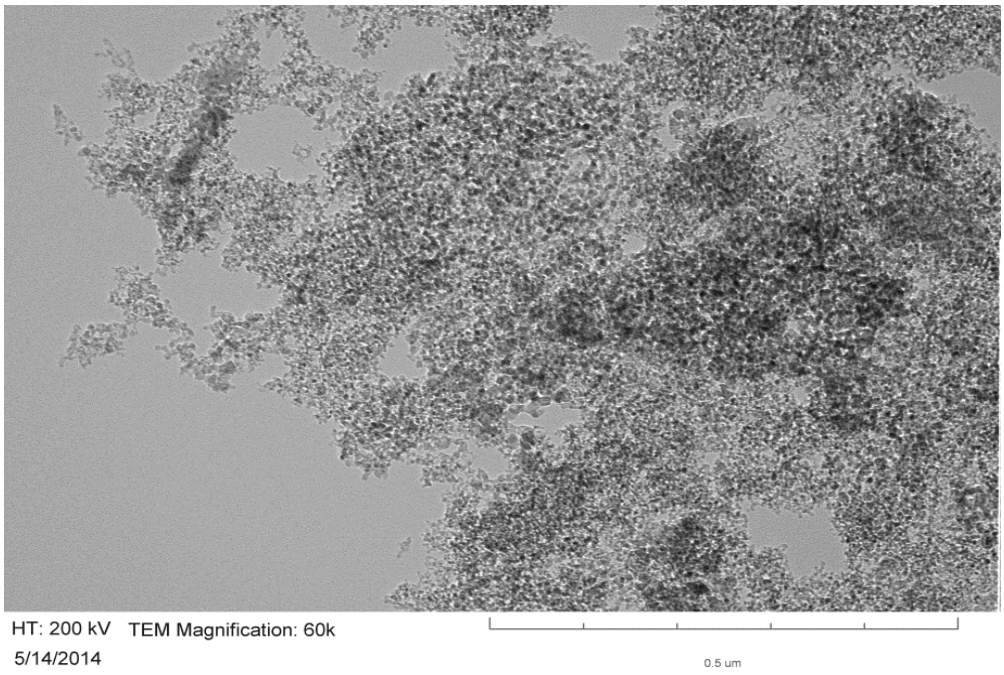

Figure A.5. TEM images of OND.

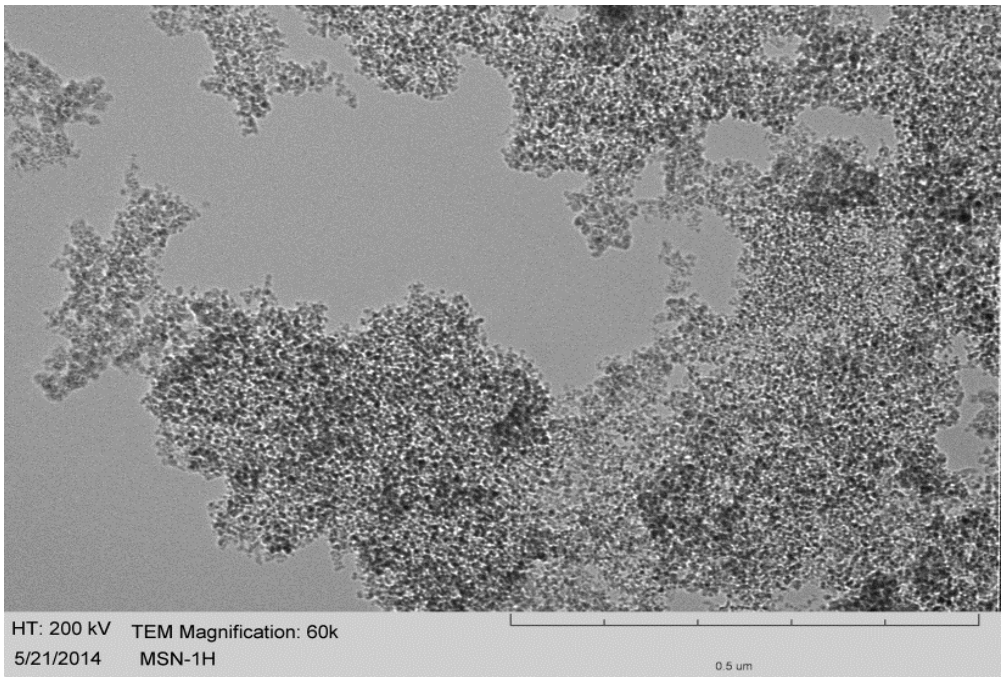

Figure A.6. TEM images of CND.

APPENDIX B

NANODIAMOND/PEEK COMPOSITES

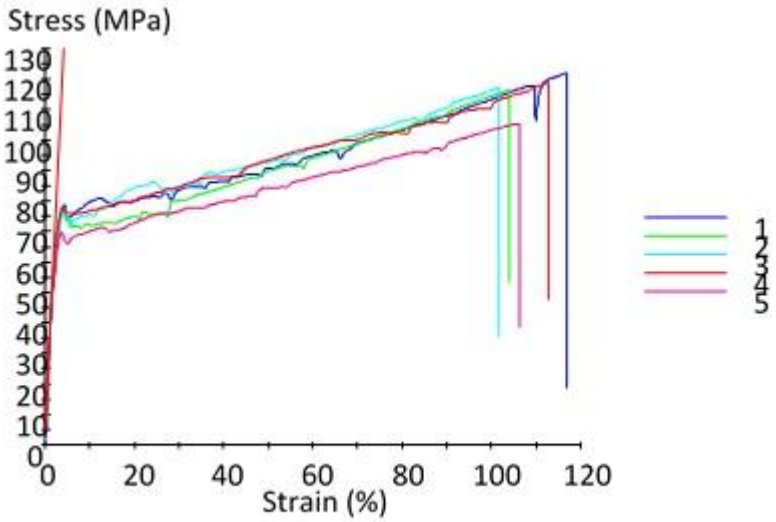

Figure B.1. Stress-Strain curve of PEEK 450PF (not annealed)

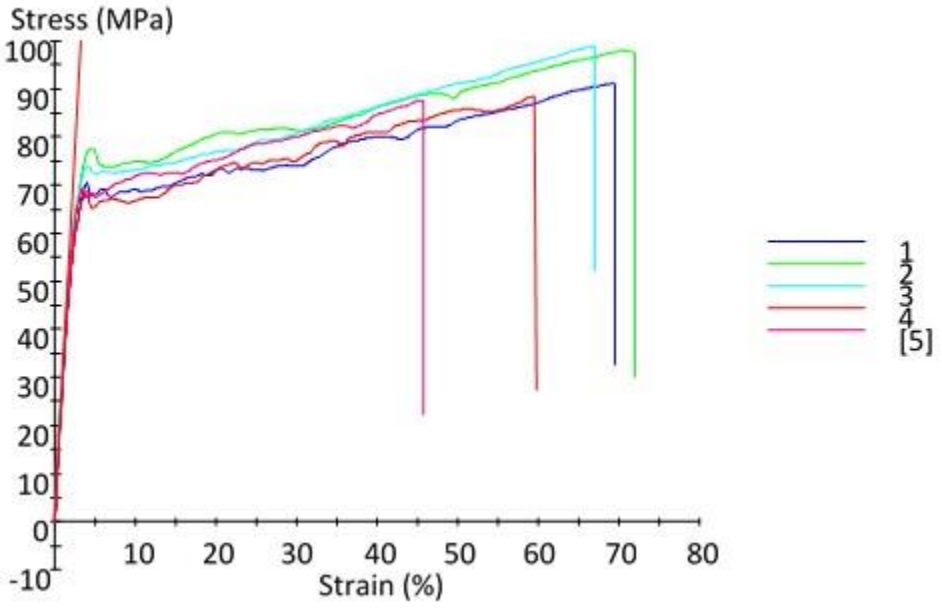

Figure B.2. Stress-Strain curve of OND_{NB}/PEEK (1%) (not annealed)

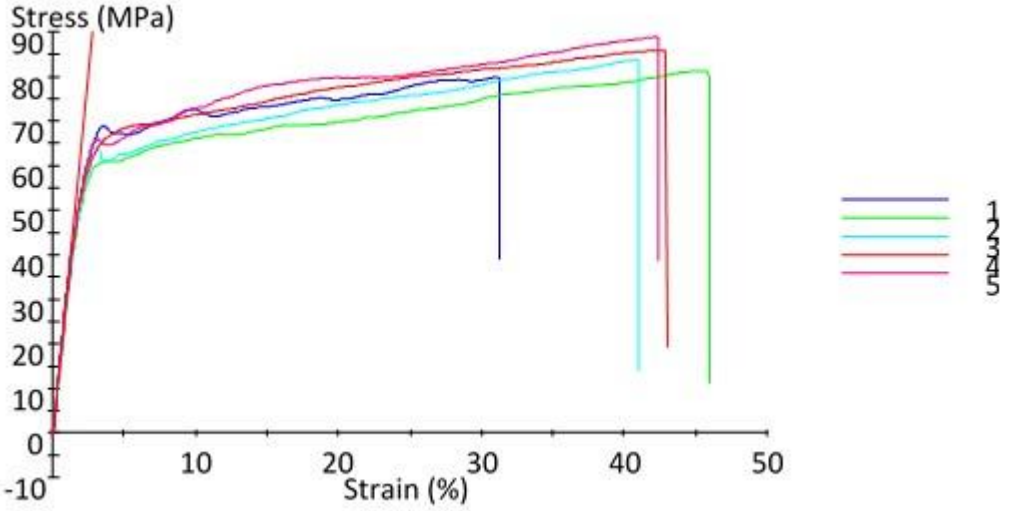

Figure B.3. Stress-Strain curve of OND_{NB}/PEEK (2%) (not annealed)

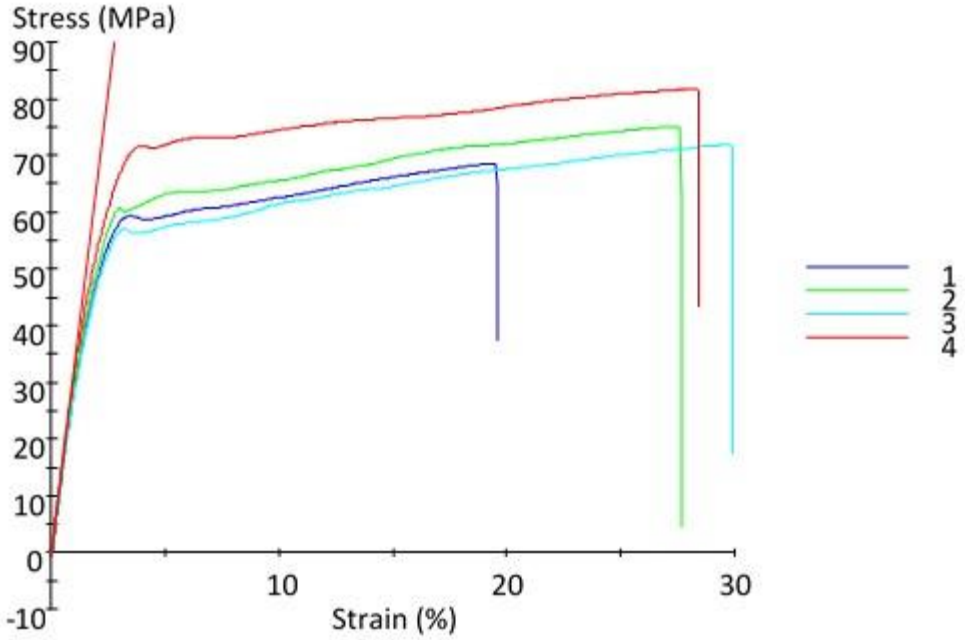

Figure B.4. Stress-Strain curve of OND_{NB}/PEEK (4%) (not annealed)

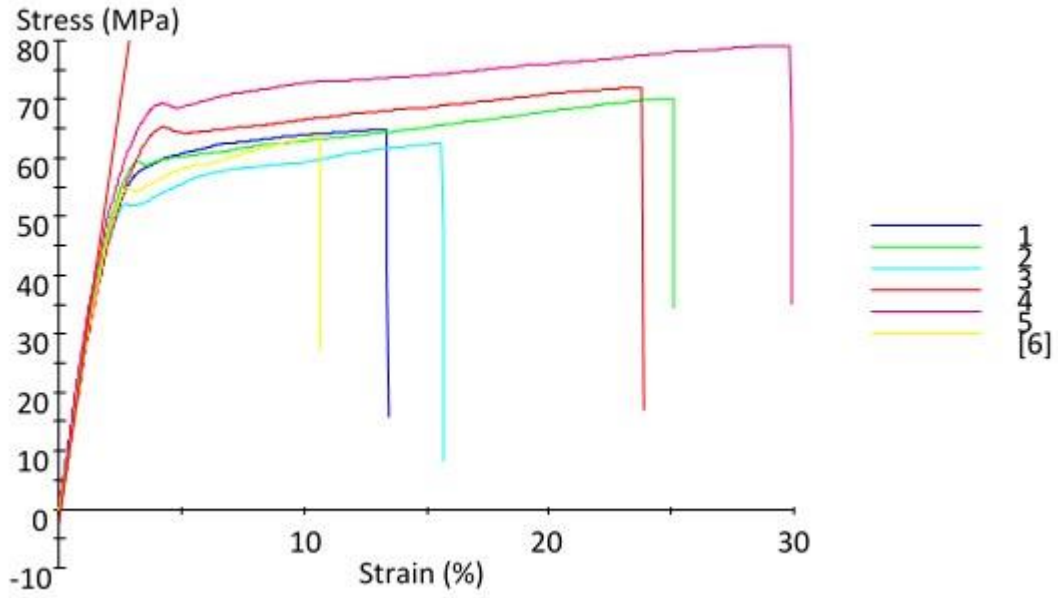

Figure B.5. Stress-Strain curve of OND_{NB}/PEEK (6%) (not annealed)

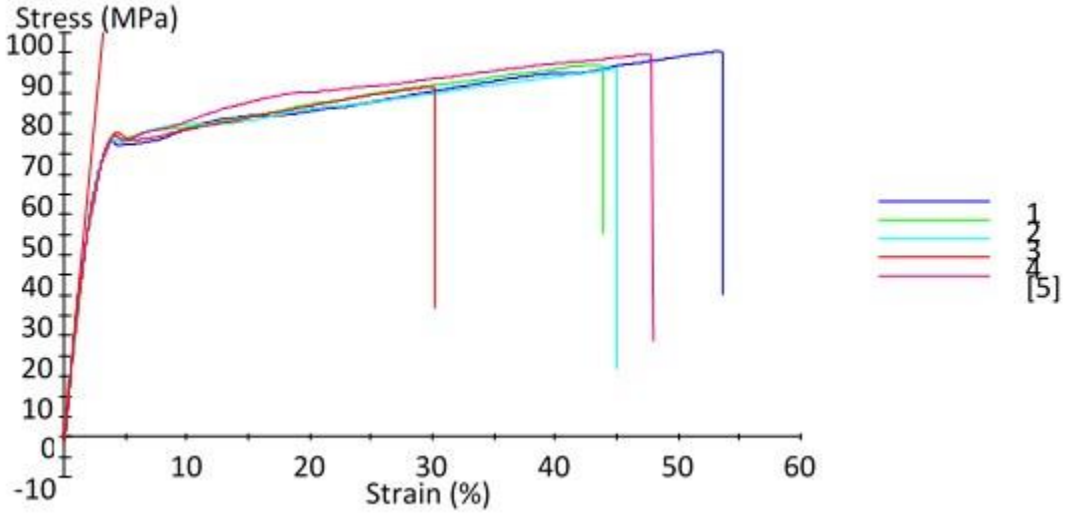

Figure B.6. Stress-Strain curve of CND_{NB}/PEEK (2%) (not annealed)

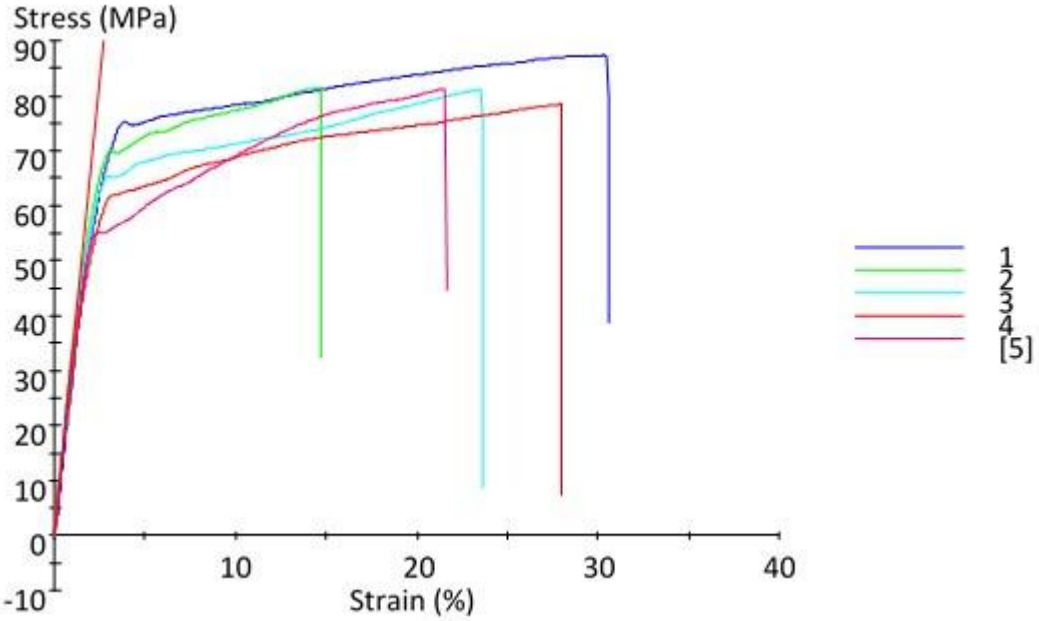

Figure B.7. Stress-Strain curve of CND_{NB}/PEEK (4%) (not annealed)

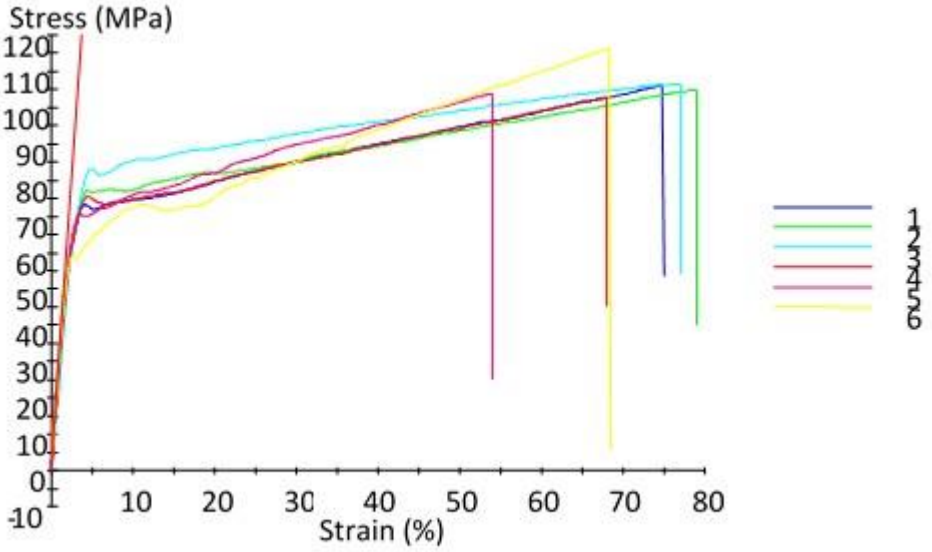

Figure B.8. Stress-Strain curve of ODA-ND_{NB}/PEEK (0.5%) (not annealed)

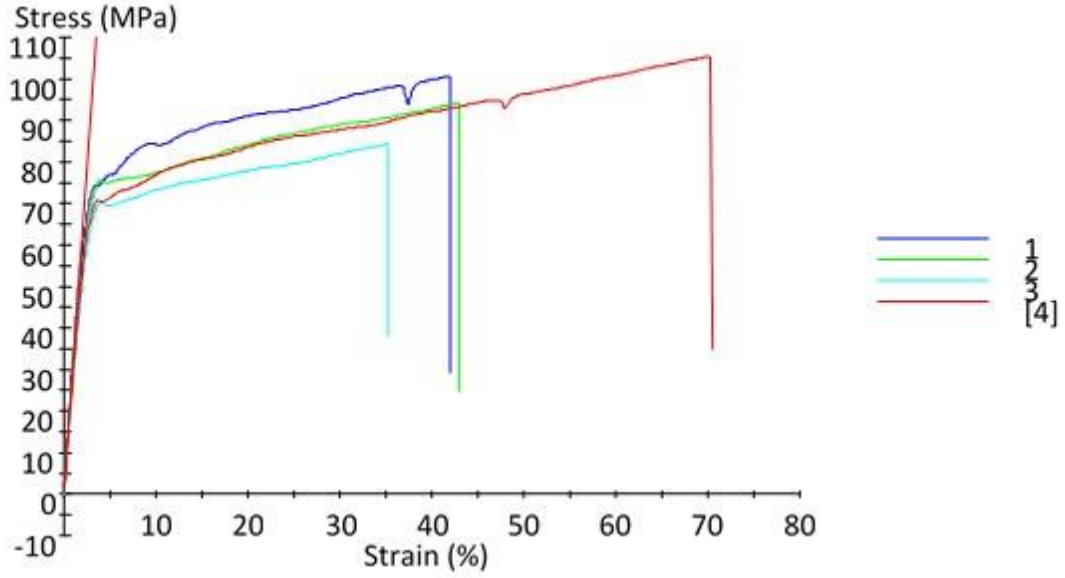

Figure B.9. Stress-Strain curve of ODA-ND_{NB}/PEEK (2%) (not annealed)

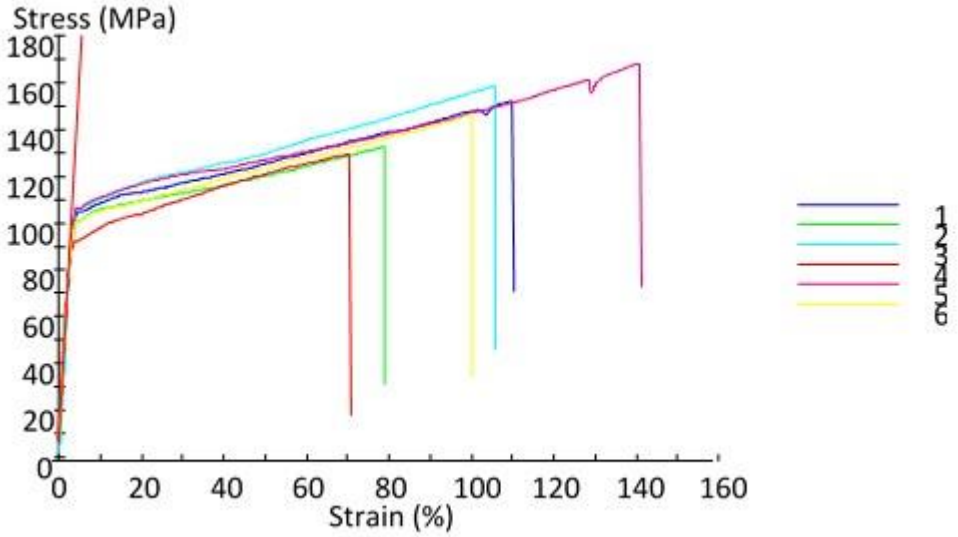

Figure B.10. Stress-Strain curve of PEEK (annealed)

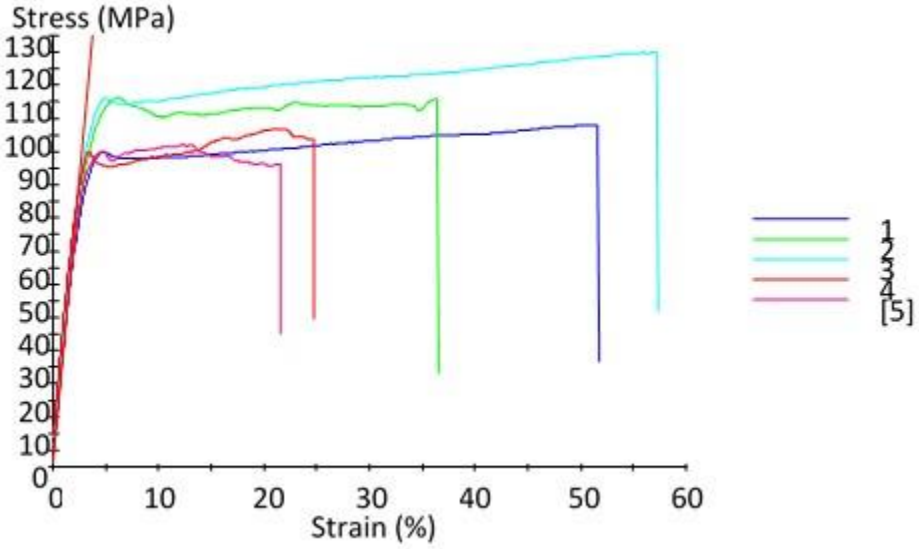

Figure B.11. Stress-Strain curve of 1% son-OND/PEEK (annealed)

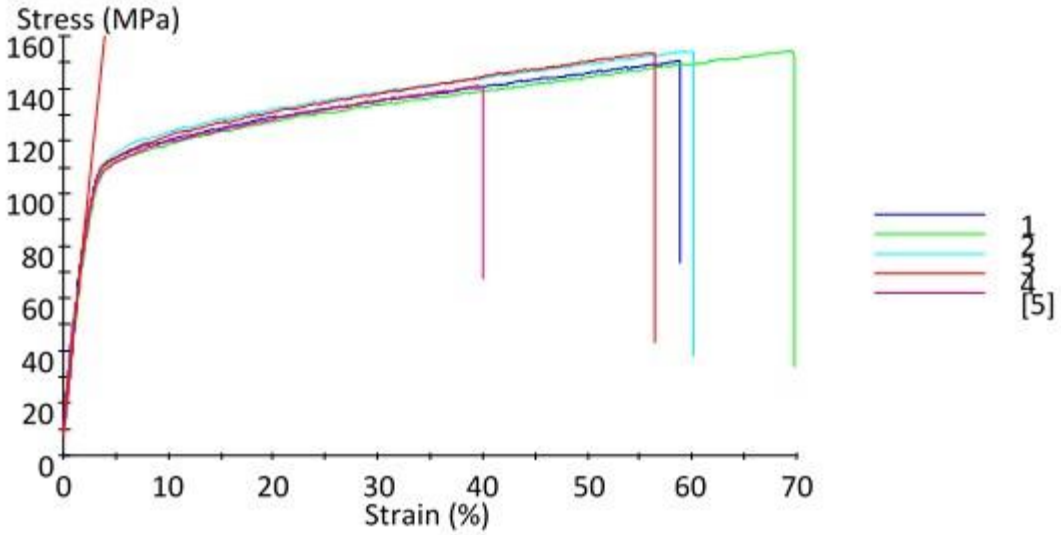

Figure B.12. Stress-Strain curve of 3% son-OND/PEEK (annealed)

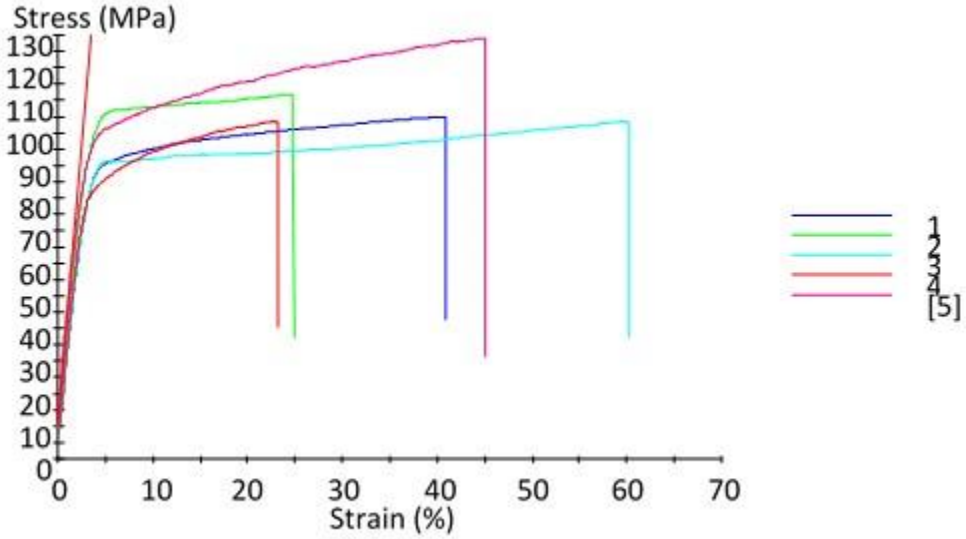

Figure B.13. Stress-Strain curve of 5% son-OND/PEEK (annealed)

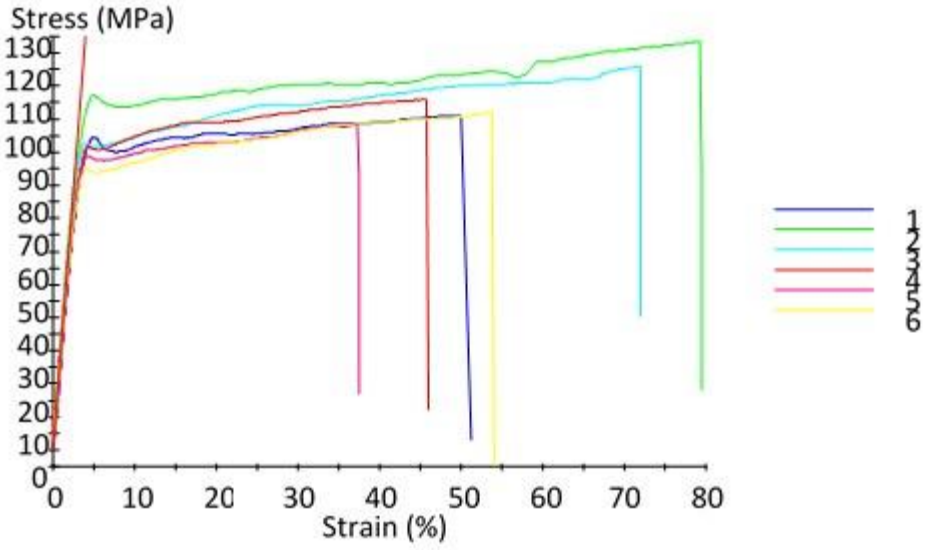

Figure B.14. Stress-Strain curve of 3% OND/PEEK (annealed)

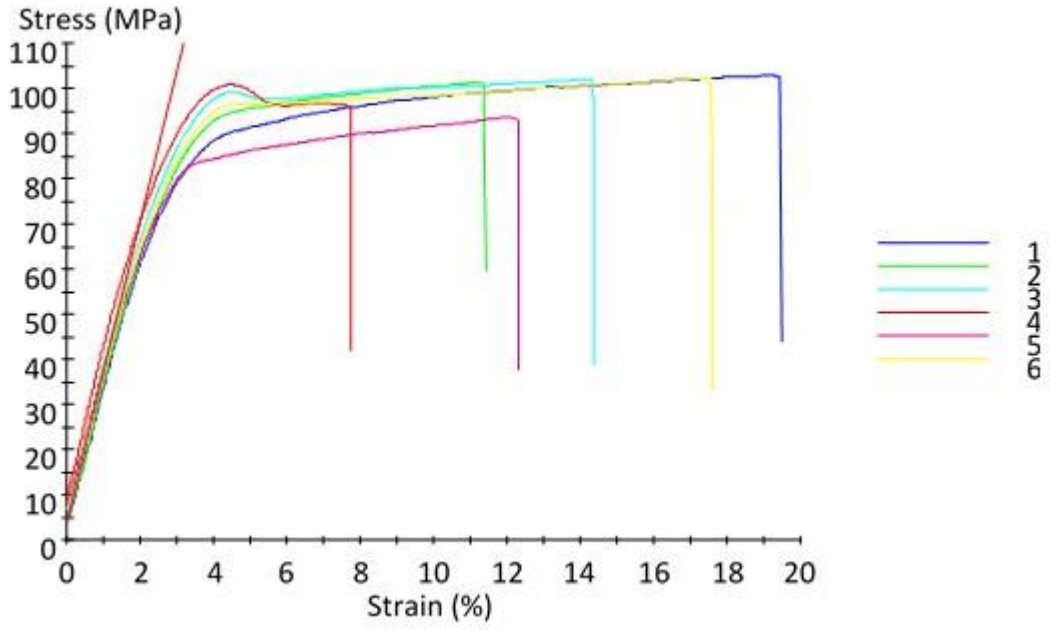

Figure B.15. Stress-Strain curve of 3% CND/PEEK (annealed)

APPENDIX C

COPYRIGHT RELEASES

This is a License Agreement between Zahidul Wahab ("You") and Nature Publishing Group ("Nature Publishing Group") provided by Copyright Clearance Center ("CCC"). The license consists of your order details, the terms and conditions provided by Nature Publishing Group, and the payment terms and conditions.

All payments must be made in full to CCC. For payment instructions, please see information listed at the bottom of this form.

License Number	3743430354521
License date	Nov 06, 2015
Licensed content publisher	Nature Publishing Group
Licensed content publication	Nature Nanotechnology
Licensed content title	The properties and applications of nanodiamonds
Licensed content author	Vadym N. Mochalin, Olga Shenderova, Dean Ho, Yury Gogotsi
Licensed content date	Dec 18, 2011
Volume number	7
Issue number	1
Type of Use	reuse in a dissertation / thesis
Requestor type	academic/educational
Format	print and electronic
Portion	figures/tables/illustrations
Number of figures/tables/illustrations	2
High-res required	no
Figures	Figure 1a and Figure 5
Author of this NPG article	no
Your reference number	None
Title of your thesis / dissertation	SURFACE MODIFICATION OF NANODIAMOND AND ITS INCORPORATION IN NANODIAMOND/PEEK NANOCOMPOSITES
Expected completion date	Dec 2015
Estimated size (number of pages)	200
Total	0.00 USD

Figure C.1. Copyright release for Figure 1.1 and Figure 1.6

ROYAL SOCIETY OF CHEMISTRY LICENSE
TERMS AND CONDITIONS

Nov 07, 2015

This is a License Agreement between Zahidul Wahab ("You") and Royal Society of Chemistry ("Royal Society of Chemistry") provided by Copyright Clearance Center ("CCC"). The license consists of your order details, the terms and conditions provided by Royal Society of Chemistry, and the payment terms and conditions.

All payments must be made in full to CCC. For payment instructions, please see information listed at the bottom of this form.

License Number	3743450577919
License date	Nov 07, 2015
Licensed content publisher	Royal Society of Chemistry
Licensed content publication	Journal of Materials Chemistry
Licensed content title	The structure and reactivity of nanoscale diamond
Licensed content author	Anke Krueger
Licensed content date	Feb 25, 2008
Volume number	18
Issue number	13
Type of Use	Thesis/Dissertation
Requestor type	academic/educational
Portion	figures/tables/images
Number of figures/tables/images	4
Format	print and electronic
Distribution quantity	3
Will you be translating?	no
Order reference number	None
Title of the thesis/dissertation	SURFACE MODIFICATION OF NANODIAMOND AND ITS INCORPORATION IN NANODIAMOND/PEEK NANOCOMPOSITES
Expected completion date	Dec 2015

Figure C.2. Copyright release for Figure 1.2-1.5

ELSEVIER LICENSE
TERMS AND CONDITIONS

Nov 07, 2015

This is a License Agreement between Zahidul Wahab ("You") and Elsevier ("Elsevier") provided by Copyright Clearance Center ("CCC"). The license consists of your order details, the terms and conditions provided by Elsevier, and the payment terms and conditions.

All payments must be made in full to CCC. For payment instructions, please see information listed at the bottom of this form.

Supplier	Elsevier Limited The Boulevard,Langford Lane Kidlington,Oxford,OX5 1GB,UK
Registered Company Number	1982084
Customer name	Zahidul Wahab
Customer address	3247 Winchester lane ORANGEBURG, SC 29118
License number	3743460344933
License date	Nov 07, 2015
Licensed content publisher	Elsevier
Licensed content publication	Journal of Colloid and Interface Science
Licensed content title	Surface functionalization of nanodiamond with phenylphosphonate
Licensed content author	Zahidul Wahab,Elizabeth A. Foley,Perry J. Pellechia,Bruce L. Anneaux,Harry J. Ploehn
Licensed content date	15 July 2015
Licensed content volume number	450
Licensed content issue number	n/a
Number of pages	9
Start Page	301
End Page	309
Type of Use	reuse in a thesis/dissertation
Intended publisher of new work	other
Portion	full article
Format	both print and electronic
Are you the author of this Elsevier article?	Yes
Will you be translating?	No
Title of your thesis/dissertation	SURFACE MODIFICATION OF NANODIAMOND AND ITS INCORPORATION IN NANODIAMOND/PEEK NANOCOMPOSITES

Figure C.3. Copyright release for Chapter 2